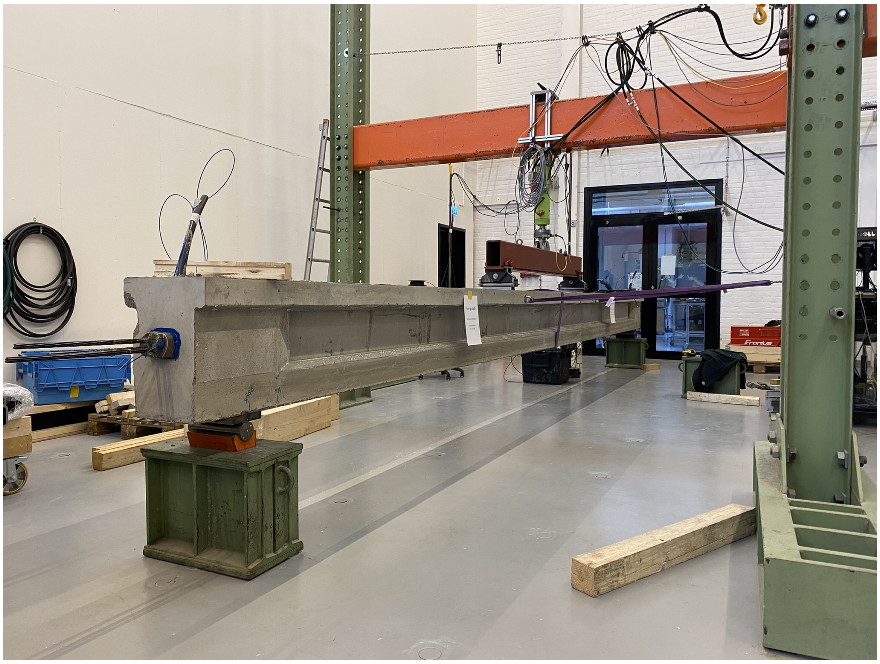

Evaluation of Post-tensioned Concrete Structures by Fiber Sensors

A study to develop sensor driven methods for evaluation of PRC elements, determine remaining prestressing force and assess key performance indicators

Master's thesis in Master Program Structural Engineering and Building Technology

LEO ADOLFSSON
OSKAR VESTIN

DEPARTMENT OF ARCHITECTURE AND CIVIL ENGINEERING

CHALMERS UNIVERSITY OF TECHNOLOGY
Gothenburg, Sweden 2022
www.chalmers.se

Master's thesis ACEX30

Evaluation of Post-tensioned Concrete Structures by Fiber Sensors

A study to develop sensor driven methods for evaluation of PRC elements, determine remaining prestressing force and assessment of key performance indicators

LEO ADOLFSSON
OSKAR VESTIN

Department of Architecture and Civil Engineering
Division of Structural Engineering
Chalmers University of Technology
Gothenburg, Sweden 2022

Evaluation of Post-tensioned Concrete Structures by Fiber Sensors
A study to develop sensor driven methods for evaluation of PRC elements, determine remaining prestressing force and assess key performance indicators

LEO ADOLFSSON
OSKAR VESTIN

Supervisor: Associate Professor Ignasi Fernandez, Department of Architecture and Civil Engineering
Postdoc Carlos Gil Berrocal, Department of Architecture and Civil Engineering
Examiner: Associate Professor Ignasi Fernandez, Department of Architecture and Civil Engineering

Department of Architecture and Civil Engineering
Division of Structural Engineering
Chalmers University of Technology
SE-412 96 Gothenburg
Telephone +46 31 772 1000

Cover: Testing of the post-tensioned specimen.

Department of Architecture and Civil Engineering
Gothenburg, Sweden 2022

Evaluation of Post-tensioned Concrete Structures by Fiber Sensors
A study to develop sensor driven methods for evaluation of PRC elements, determine remaining prestressing force and assess key performance indicators.
Leo Adolfsson
Oskar Vestin
Department of Architecture and Civil Engineering
Chalmers University of Technology

Abstract

Prestressed concrete structures have numerous advantages over conventionally reinforced concrete, though the usage of post-tensioned structures has declined over the last decades. Structural health monitoring (SHM) have potential to change this trend and by implementing this technique in civil structures the knowledge about the structural response over time will increase. By constructing two beams and implement distributed optical fiber sensors (DOFS), key performance indicators of the post-tensioned concrete specimens were monitored and evaluated. One specimen was post-tensioned, while the other one served as a reference specimen, built the same apart from being prestressed.

Initial losses, as well as long term effects affecting prestressing force, deflections and cracks were tracked and compared to theoretical calculation methods. Later, the specimens were pre-cracked and tested in a four-point bending test. It was found that the theoretical calculation methods mostly agreed well with results from the distributed optic fiber sensors. The loss of prestressing force due to creep and relaxation differed 0.8 %, while the loss due to friction differed 0.6 %. Regarding deflections, the relative error ranged up to 3.3 % for the reference specimen, while the post-tensioned reinforced concrete specimen ranged up to 2.9 %.

The crack onset was traced using both Digital image correlation (DIC) and DOFS. Due to the low strain values, it was only the DOFS that were able to capture the crack onset. Comparisons were made to previous research to verify the assumption that certain strain peaks could be correlated to crack onset.

The results and conclusions are a foundation for larger scale use of structural health monitoring systems implemented in civil engineering structures, that could contribute to safer, sustainable, and more resilient infrastructure.

Keywords: Post-tensioned concrete, Distributed optical fibre sensing, Prestressing force, Rayleigh backscattering, Crack monitoring, Performance indicators

Acknowledgements

This master's thesis was performed as an quantitative study at the division of Structural Engineering at Chalmers University of Technology in Gothenburg, Sweden. Its purpose was to monitor and to evaluate post-tensioned reinforced concrete beam using Fiber optic sensors. The main part of the experimental work was conducted in the concrete laboratory at Chalmers and the whole project was executed as a cooperation between Chalmers, WSP Sweden and NCC AB.

Firstly, we want to express our gratitude and thank our examiner Assoc Prof. Ignasi Fernandez and supervisor Postdoc. Carlos Gil Berrocal at the division of Structural Engineering. Especially for their engagement and support through the project and providing us with the right tools to carry through the project.

We would also like to give a special thanks to Sebastian Almfeldt and Anders Karlsson at the concrete laboratory for their engagement and many hours of help during the experimental part of this research. It would not have been possible to conduct the experiment in a successful manner without your knowledge and experience.

Finally, we would like to thank our opponent group, Siri Salander and Ofelia Fredriksson for their feedback and interest in our work during this period.

Leo Adolfsson, Gothenburg, June 2022
Oskar Vestin, Gothenburg, June 2022

Contents

Nomenclature

Greek letters

α	Angle/ fraction
α_R/β_R	Stress block parameters
α_c	Coefficient taking account of long term effects
χ_∞	Final relaxation factor
χ_t	Relaxation factor at time t
χ_{1000}	Relaxation loss for prestressing steel after 1000h at 20°C
$\Delta\sigma_p$	Stress change in prestressing steel
$\Delta\varepsilon_{tendon}$	Strain change in prestressing steel
ΔP	Relative loss of prestressing force
Δs	Wedge penetration
η	Reduction factor to account for long term effects
γ_c	Partial safety factor for concrete
γ_p	Partial safety factor for prestressing steel
γ_s	Partial safety factor for reinfocement steel
μ	Frictional coefficient/ Initial stress level for prestressing steel
σ	Stress/Standard deviation
σ_c	Tensile stress in concrete
σ_p	Stress in prestressing steel
σ'_s	Stress in top reinforcement
σ_s	Stress in bottom reinforcement
$\sigma_{cc\infty}$	Compressive stress in concrete after long time
σ_{cci}	Initial compressive stress in concrete
$\sigma_{ct\infty}$	Tensile stress in concrete after long time
σ_{cti}	Initial tensile stress in concrete
θ	Rotation of the specimen
ε_{bottom}	Strain at the level of the bottom fiber
$\varepsilon_{c,creep}$	Creep deformation of concrete
$\varepsilon_{c,el}$	Elastic part of concrete deformation
ε_{ca}	Autogenous shrinkage strain
ε_{cc}	Concrete strain at the compressed edge of the cross-section
ε_{cd}	Drying shrinkage strain
ε_{cpi}	Initial concrete strain at the level of the prestressing steel
ε_{cs}	Total shrinkage strain
ε_{p0i}	Initial strain difference between prestressing steel and concrete
ε_{pi}	Initial strain in prestressing steel
ε_{PRC}	PRC specimen strain

ε_{RC}	RC specimen strain
$\varepsilon_{s'}$	Top reinforcement steel strain
ε_{s}	Bottom reinforcement steel strain
ε_{top}	Strain at the level of the top fiber
$\varphi(t_0, t)$	Creep coefficient

Roman lowercase letters

$\bar{x}_c$	Center of gravity, gross concrete section
$\bar{x}_i$	Center of gravity
b_w	Width of web
b_{tf}	Width of top flange
e	Eccentricity
e_{net}	Eccentricity net section
f_{cd}	Design value of concrete compressive strength
f_{ck}	Characteristic compressive cylinder strength of concrete at 28 days
f_{cm}	Mean concrete cylinder compressive strength
f_{ctd}	Design value of concrete tensile strength
$f_{ctk,0.05}$	Lower characteristic tensile strength of concrete, 5% fractile
$f_{ctk,0.95}$	Upper characteristic tensile strength of concrete, 95% fractile
f_{ctm}	Mean concrete tensile strength
f_{ct}	Tensile concrete strength
f_{puk}	Ultimate characteristic tensile strength reinforcement steel
f_u	Ultimate capacity
f_{yd}	Design yield strength of reinforcement
f_{yk}	Characteristic yield strength of reinforcement
f_y	Yielding capacity
h	Height
h_{tf}	Height of top flange
k	Unintended angular displacement per unit length
l_{tendon}	Length of prestressing steel/tendon
m_i	Mass
s	Minimum shear reinforcement spacing
t	Time
x	Distance
x_{net}	Center of gravity for net section
y	Deflection of the specimen
z	Distance between bottom and top fiber

Roman uppercase letters

A_c	Sectional area of gross concrete section
$A_{I,ef}$	Effective sectional area state I
A_I	Sectional area of transformed concrete section state I
A_i	Sectional area
A_{net}	Sectional area of transformed concrete section
A_p	Sectional area of prestressing steel
A_{sw}	Cross-sectional area of shear reinforcement unit
A_{tf}	Sectional area of top flange
E_p	Modulus of elasticity, prestressing steel

E_s	Modulus of elasticity, reinforcement steel
E_{cm}	Modulus of elasticity for concrete
EI	Flexural stiffness of the section
$F_{cs,p}$	"Shrinkage force" at the level of prestressing steel
$F_{cs,s'}$	"Shrinkage force" at the level of the top reinforcement
$F_{cs,s}$	"Shrinkage force" at the level of the bottom reinforcement
I_c	Second moment of area for gross concrete section
$I_{I,ef}$	Effective second moment of area state I
I_{net}	Second moment of area for net concrete section
M	Bending moment
M_{g0}	Bending moment due to self-weight of the prestressed member
M_{qt}	Additional long term moment excluding moment due to self-weight
M_q	Additional maximum moment excluding moment due to self-weight
P_{0i}	Initial effective prestressing foce
P_i	Tendon force in the prestressing steel
S	First moment of area of the cross-section
V_{Ed}	Design shear force
V_{ipd}	Transverse component of inclined prestressing force

1

Introduction

1.1 Background

In the beginning of the 20th century usage of concrete structures was commonly connected with issues as creep and shrinkage. These effects were not well understood at this time [1] and to solve these issues and delay cracking of the concrete, development of prestressed concrete structures started to take place. The development took some time and it was not until the 1930s the usage of prestressing structures was successful. Prestressing of a member can be explained such that the member is subjected to an external compressive force. This can be made in two ways, either by pre- or post-tensioning [2].

Post-tensioned reinforced concrete (PRC) was first introduced in Swedish infrastructure in 1943, when it was used in the *Klockestrand Bridge*. Since then, the technology has been a key part of civil structures due to its ability to reduce deflections, minimize material use and provide more aesthetic, economical and sustainable solutions [1],[3]. Even though there are several benefits using post-tensioning, in later years the usage of this type of system in concrete bridges has decreased, see Figure 1.1.

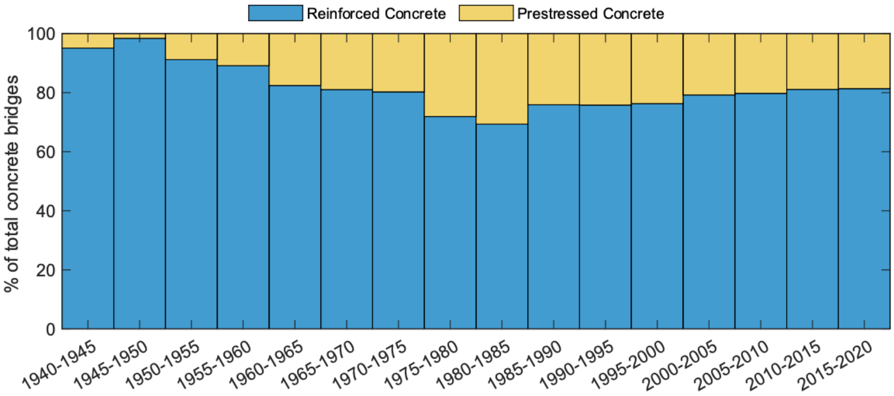

Figure 1.1: Reinforcement technology used in the concrete bridges built in Sweden during the last 80 years [4].

There are several theories behind this trend, as for example, complexity during construction and longer construction time. One other explanation for this decrease is that many of the old bridges built using this technique have started to show signs of deterioration. To be able to determine the functionality and safety of these structures, information about the residual prestressing force in the tendons after time is needed and yet there are several uncertainties connected to this area.

Fiber optics technique have been used for many decades in different fields to measure strain and temperature. The old technique based on Fiber Bragg Grating have its limitations and in the last decade, researchers have developed and increased knowledge around Distributed Optic Fiber sensors (DOFS). DOFS can measure the strain with a high resolution and researchers in the field of Civil Engineering have been able to correlate the measured strain with performance indicators of concrete structure. For example have cracks, not visible for the naked eye, been detected at an early stage by analysing the strain output. According to [5], this way of capture the behaviour of reinforced concrete beams can be considered as accurate as other older commonly used measurement devises and the increase of spatial resolution will boost the knowledge in this area. Development and increased usage of Fiber Optics in real structures will increase the safety and give engineers the tools to design more material efficient structures with a reduced environmental impact.

1.2 Aim and objectives

The aim of the thesis is to develop robust sensor-driven models, to be able to analyse the behaviour of the residual prestressing force, and to track important key indicators during the lifespan of a PRC element.

The objective of the thesis is to experimentally test the use of Distributed Optic Fiber Sensors, DOFS, to monitor long-term effects on PRC elements. Additionally, the objective is to adapt and extend methods that corresponds to reinforced concrete (RC) structures, such as deflection, to be suitable for application on PRC structures.

1.3 Limitations

The results of this study were limited to the measurement from one PRC beam and one reinforced concrete beam. Due to the large scale of the specimens and the limited amount of time for construction it was not possible to have more than these two samples.

In the sectional analysis of the specimens, the end sections (400 mm from the edges) were not considered since no or only some fibers were deployed at this area.

Due to the complexity to separate the different effects, the effect from relaxation of the post-tensioned tendons was not distinguished in the evaluation of the measured data even though it contributes to a loss of prestressing force over time.

1.4 Methodology

This project will be carried out in two main phases. The first phase consists of design and construction of two specimens with a length of 8 m suitable for the project. The first specimen is a PRC member, which is the main interest of the thesis. The second member is identical to the first one, where the only difference is that it is not post-tensioned. Thereby the second member will act as a reference and the shrinkage and temperature induced strain can be isolated and the post-tension effects can be analysed independently and more accurate. The construction of the two beams includes manufacturing of wooden frameworks and reinforcement cages, as well as installation of post-tensioning system and fiber optic sensors.

The second phase will mainly focus on retrieving and analysis of data from the DOFS as well as material testing and bending tests of the specimens. The effect from post-tensioning as well as other effects in the concrete, will be monitored by the distributed optic fiber sensors. The results will be analysed and compared accordingly to the aim of the project.

2

Theory

2.1 Prestressing effect

Prestressing is in principle the collective name for two commonly known techniques, pre-tensioning, and post-tensioning. The aim of prestressing is to mainly influence the cracking load, where the effect of prestressing is favourable. By carefully selecting a specific prestressing force, cracks can be avoided in the serviceability limit state (SLS). Thereby the cross section will remain fully effective in State I, until the design load is obtained. Unlike in a reinforced member, where the change of rigidity can occur before the SLS load, this effect is removed in a prestressed member [1].

However, in general the prestressing effect does not affect the flexural resistance, which is a common misunderstanding. As soon as cracking of concrete occurs, the steel influences the flexural resistance in the same way as in a reinforced member. There might be a small increase in capacity, but this is due to the prestressing steel area and its lever arm, regardless if the prestressing effect is active, i.e. tensioned or not [1].

In contrary to the flexural resistance, the shear resistance has a favourable effect of the prestressing in the same manner as a normal force. This is mainly because shear cracks are delayed, and in some cases even fully prevented [1].

2.2 Prestressing force

Regarding prestressed structures, it is important to understand the difference between tendon force and effective prestressing force. Furthermore, it is important to know the difference between the two approaches used to evaluate and design prestressed structures. These are the tendon force approach and the strain compatibility approach.

2.2.1 Effective prestressing force

The effective prestressing force is the internal restraint that is created by means of tensioning of the steel in relation to the concrete. This means that the effective prestressing force, unlike the tendon force, is not dependent on the load on the structure, but rather by the time dependent effects. Relaxation, creep, and shrinkage all have an effect on the effective prestressing force. The initial effective prestressing force P_{0i} is calculated according to Equation 2.1 and is a function of the difference between initial steel strain and initial concrete strain [1].

$$P_{0i} = E_p \varepsilon_{p0i} A_p \qquad \text{where:} \qquad \varepsilon_{p0i} = \varepsilon_{pi} - \varepsilon_{cpi} \tag{2.1}$$

P_{0i} - Initial effective prestressing force
E_p - Modulus of elasticity for prestressing steel
A_p - Sectional area of prestressing steel
ε_{pi} - Initial stain in the prestressing steel
ε_{cpi} - Initial concrete strain at the level of the prestressing steel
ε_{p0i} - Initial strain difference between prestressing steel and concrete

The tendon force, often denoted as P, is the actual force in the tendon during any load case.

2.2.2 Tendon force approach

The tendon force approach is an approach where the tendon force is considered as an external load. The tendon steel area is not considered as a part of the transformed concrete section, see Equation 2.2. The disadvantages of the tendon force approach are that the tendon force varies when the structure is loaded. An axial force on the member causes an elongation/contraction, which then affects the tendon force [1].

$$A_{net} = A_c - A_p + (\alpha_s - 1)A_s \qquad \text{where:} \qquad \alpha_s = \frac{E_s}{E_{cm}} \tag{2.2}$$

A_c - Area of gross concrete section
A_s - Sectional area of reinforcement steel
A_{net} - Area of transformed concrete section
E_s - Modulus of elasticity for reinforcement steel
E_{cm} - Modulus of elasticity for concrete

2.2.3 Strain compatibility approach

In the strain compatibility approach, the area of the tendon is considered in the resisting cross section. Both the prestressing steel and reinforced steel are included in the transformed concrete section, see Equation 2.3. This approach is only applicable when there is full interaction between the tendon and the concrete surrounding it. This on the other hand, means that the prestressing force is not affected by further loading [1].

$$A_I = A_c + (\alpha_p - 1)A_p + (\alpha_s - 1)A_s \qquad \text{where:} \qquad \alpha_p = \frac{E_p}{E_{cm}} \tag{2.3}$$

A_I - Area of transformed concrete section in state I

2.3 Prestressing degree

A prestressed member can be subjected to either full or partial prestressing. The mentioned phenomenon's will be further explained in the upcoming sections.

Full prestressing essentially means that no cracks are allowed at all in SLS. This can be divided in two categories, incomplete and complete prestressing. Incomplete prestressing is the case when some tensile stress is accepted in the tensile edge of the member, as long as it is not exceeding the tensile strength. Complete prestressing on the other hand is when no tensile stress at all is allowed in the member [1].

- Incomplete prestressing: $\sigma_c \leqslant f_{ct}$
- Complete prestressing: $\sigma_c \leqslant 0$

σ_c - Tensile stress in concrete
f_{ct} - Tensile strength of concrete

With partial prestressing, limited and controlled cracking is accepted in SLS. Though limited cracking is accepted, there is still differences to a reinforced concrete member. In a reinforced concrete member, cracks can in some cases occur for small loads, and thereby change the sectional rigidity abruptly. These cracks are then present through the whole life span, increasing the risk of corrosion in the member. A partial prestressed member is subjected to both a bending moment due to the eccentricity of the tendon, and a compressive prestressing force. This will prevent cracks for small loads, and the member will recover from cracks when unloaded from a high load, mainly due to the compressive force.

2.4 Post-tensioning

In post-tensioned concrete structures, as the name suggests, the concrete is cast before the tensioning of the prestressing steel takes place. In civil engineering constructions, such as bridges, the structure is often provided with one or several ducts, in which the prestressing steel lies. After tensioning, these ducts are injected with grout. This is to enable steel to concrete interaction, as well as to protect against corrosion [1].

In construction of houses another type of post-tensioned system is commonly used, which consists of single unbonded strands. These strands require no grouting, as the strand is placed in a plastic cover where it can move freely. On the other hand, this means the strand has no bond interaction with the concrete [1].

2.4.1 Tendon profile

Regarding the post-tensioned tendon profile, it can be chosen more freely than for a pre-tensioned member, because a pre-tensioned member often requires a straight profile as it is tensioned with no active external boundaries. When tensioning the post-tensioned member, the prestressing effect is created by means of an external boundary in form of, in most cases, a parabolic shape of the duct. This shape can then be chosen and adjusted to the actual design criteria, normally to counteract the bending moment caused by the self-weight [1].

2.4.2 Tensioning procedure

In the tensioning procedure, a hydraulic jack is often used to tension the tendons. It is placed towards the concrete and tensioned to the intended force. Anchor wedges are used, which fixes the active reinforcement in both ends. Modern jacks have capacity to tension several tendons at once, while some jacks only have capacity to tension one tendon at the time. In this case, it is of importance to calculate the intended force respectively for each tendon, since the contraction of the structure will be affected after the first tensioning [1].

After tensioning, the duct is injected with grout. By injecting the grout at the two highest points, this procedure can be controlled to validate that the duct is completely filled [1].

2.4.3 Initial losses

Wedge penetration, frictional losses and elastic shortening are three effects that reduce the tendon force. All these effects are caused instantaneously after tensioning and are often referred to as the initial losses.

When tensioning a tendon with a jack, losses from wedge penetration occurs. The wedge penetration is a result of the movement, as the anchorage wedge move inward when it bites into the tendon, as well as the spacing in the jack that enables for movement of the wedge along the tendon. The total movement ranges between approximately 3 to 25 mm, depending on the jack and tensioning method. The slip and penetration lead to a small force loss of the tendon, which is commonly compensated by overstressing. The stress loss from wedge penetration is calculated according to Equation 2.4, by dividing the wedge penetration, Δs by the length of the tendon, to achieve an average strain. Then this strain is multiplied with the modulus of elasticity to calculate the stress loss [2].

$$\Delta\sigma_p = \frac{\Delta s}{l_{tendon}} E_p = \Delta\varepsilon_{tendon} E_p \tag{2.4}$$

$\Delta\sigma_p$ - Stress change in prestressing steel
Δs - Wedge penetration
l_{tendon} - Length of the prestressing steel/tendon
$\Delta\varepsilon_{tendon}$ - Strain change in prestressing steel

Frictional losses are a phenomenon in post-tensioned members that occurs when the active reinforcement is being tensioned. During this process the tendon slides against the inside of the duct as the force is increased. The losses are divided in two parts, the first is *wobble friction*, which is a result of roughness and misalignment of the duct. It is described by a factor k. The second part, *curvature friction* is a result of the intentional parabolic shape of the duct, when the tendon slides against the lower or upper part. The angular part is described by the factor a while the friction part is described by the factor μ, see Equation 2.5 [2].

$$P_i(x) = P_i(0)e^{-\mu(\alpha+kx)} \tag{2.5}$$

$P_i(x)$ - Tendon force at position x
μ - Frictional coefficient
α - Change of slope
k - Unintended angular displacement per unit length
x - Length of duct from active end to evaluated section

As [1] mentions, during post-tensioning the concrete member will be compressed and shortened. As the tendon is tensioned, elastic shortening simultaneously occur in the concrete due to the induced compressive force. Thereby the tendon, depending on if tensioned individually or in group, behaves different with different methods. Inducing a higher compressive force in the concrete results in a contraction. This results in a loss of force in the previously tensioned tendons during the procedure. To account for this effect, overstressing and individual tensioning force is often used to compensate for this. For a group of tendons tensioned simultaneously, all tendons contribute to the elastic shortening and this effect can be controlled.

2.5 Material behaviour

In this chapter the theory behind each material of a post-tensioned reinforced concrete (PRC) structure will be explained and the global behaviour of a PRC element.

2.5.1 Concrete

As known, concrete is one of the most common building materials used in civil engineering and has been used for a very long time. A high compressive strength and a lower tensile strength is what characterises plain concrete [6]. The behaviour of plain concrete specimen with varying strength can be seen in Figure 2.1. From the figure, concrete with low strength has a more ductile behaviour compared with high strength concrete that shows a more brittle behaviour.

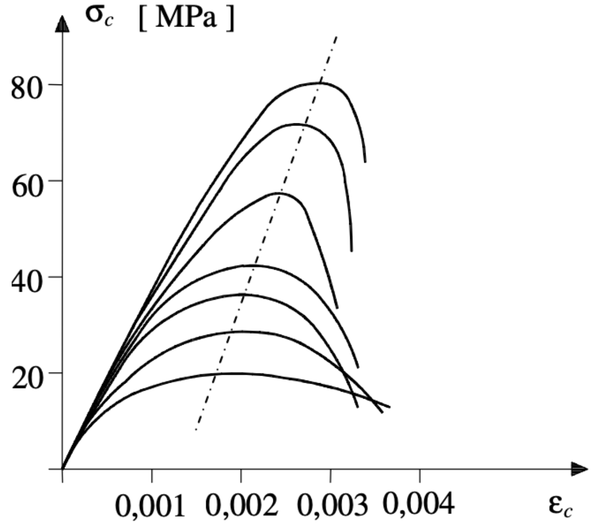

Figure 2.1: Stress-strain relation for compressed concrete with different compressive strength. From [6].

In Sweden, a normal method to test concrete compression strength is by using 150 mm cubes, which are tested uniaxially. According to EN-standard, another method is to uniaxially compress a cylinder, with a height of 300 mm and diameter of 150 mm. The correlation between these two test are shown in Equation 2.6. The cylinder strength is the commonly used strength in calculations of concrete and is denoted as f_{cm} [6].

$$f_{cm} \approx \frac{f_{cm,cube}}{1.2} \tag{2.6}$$

According to Eurocode 2 [7], there is a number of relations between concrete strength, characteristic values and design values for tensile and compression.

$$\begin{aligned} &\text{Compression:} && f_{cm} = f_{ck} + 8\text{MPa} \\ & && f_{cd} = \alpha_{cc}\frac{f_{ck}}{\gamma_c} \\ &\text{Tension:} && f_{ctk,0.05} = 0.7 f_{ctm} \\ & && f_{ctk,0.95} = 1.3 f_{ctm} \\ & && f_{ctd} = \alpha_{ct}\frac{f_{ctk,0.05}}{\gamma_c} \end{aligned}$$

f_{cm} - Mean concrete cylinder compressive strength
f_{ctm} - Mean concrete tensile strength
f_{ck} - Characteristic compressive cylinder strength of concrete at 28 days
f_{cd} - Design value of concrete compressive strength
$f_{ctk,0.05}$ - Lower characteristic tensile strength of concrete (5% fractile)
$f_{ctk,0.95}$ - Upper characteristic tensile strength of concrete (95% fractile)
f_{ctd} - Design value of concrete tensile strength

$\alpha_{c..}$ - Coefficient taking account of long term effects and other unfavourable effects
γ_c - Partial safety factor for concrete

In Eurocode 2 [7], the following requirements are established, see Equation 2.7-2.10. For partial prestressing, the limits for tensile strength are adjusted to fulfil the requirements for each specific project.

Initial concrete tensile stress:

$$\begin{array}{ll} \text{Incomplete prestressing:} & \sigma_{cti} \leqslant f_{ctk,0.05} \\ \text{Complete prestressing:} & \sigma_{cti} \leqslant 0 \end{array} \tag{2.7}$$

Initial concrete compressive stress:

$$|\sigma_{cci}| \leqslant 0.45 f_{ck} \tag{2.8}$$

Concrete tensile stress after long time:

$$\begin{array}{ll} \text{Incomplete prestressing:} & \sigma_{ct\infty} \leqslant f_{ctk,0.05} \\ \text{Complete prestressing:} & \sigma_{ct\infty} \leqslant 0 \end{array} \tag{2.9}$$

Concrete compressive strength after long time:

$$|\sigma_{cc\infty}| \leqslant 0.45 f_{ck} \tag{2.10}$$

Effects that will influence concrete over time is shrinkage and creep. The equations for the upcoming sections is based on Eurocode 2 [7]. Shrinkage is a load-independent effect in concrete that is caused by chemical reactions and water evaporation. The total shrinkage of concrete consists of two components, drying shrinkage and autogenous shrinkage, Equation 2.11.

$$\varepsilon_{cs}(t) = \varepsilon_{cd}(t) + \varepsilon_{ca}(t) \tag{2.11}$$

ε_{cs} - Total shrinkage strain
ε_{cd} - Drying shrinkage strain
ε_{ca} - Autogenous shrinkage strain

Drying shrinkage is mainly influenced by the surrounding conditions, due to the exchange of moisture between the concrete and surrounding air. If there are dry conditions with high temperature the exchange will go faster. When the free water in the concrete evaporates the concrete volume will decrease. If the area of concrete surfaces exposed to the surrounding air is big, the evaporation will be quicker and so the volume decrease of the concrete [6].

Autogenous shrinkage is caused by the reaction between water and cement in concrete. During the hardening process of concrete, the water will react with the cement and create an exothermic process also known as hydration. In newly cast concrete there is a lot of water that is participating in this process. With time, the concrete will dry out, be consumed, and chemically bounded into the C-S-H (Calcium-

Silicate-Hydrate) gel and the amount of water that can react will decrease. The process will thereby slow down and that is why autogenous shrinkage will decrease with time [6]. The main parameters that influences the size of the total shrinkage are according to [6] is:

- Concrete mixture, water/cement ratio and surface treatment
- Surrounding conditions: temperature and relative humidity
- The shape of section and size of surfaces exposed to the surrounding environment
- Age of the concrete

Creep is in contradistinction to shrinkage, a load-dependent effect that is highly time dependent. The total long-term deformation consists of two parts, one initial elastic part and one part that is influenced by the duration of loading and the age of concrete at loading. In case of constant load, the total creep at a certain time can be calculated according to Equation 2.12 and follows the behaviour obtained in Figure 2.2a. As mentioned creep is both depend on the concrete age at loading and the load duration and that is why the creep function $\varphi(t, t_0)$ is a function of two separate time variables.

In case of varying load, with both loading and unloading there will still be deformations left after unloading from the creep as seen in Figure 2.2b. To calculate the creep coefficient at a certain time it is important to take the load history of the structure until that time into consideration. To calculate the creep, Eurocode 2 [7] provides variables that is based on the surrounding environment, concrete class, age at loading and the nominal size of the structure [6].

$$\varepsilon_{c,creep}(t) = \varepsilon_{c,el} + \varphi(t, t_0)\frac{\sigma_c}{E_{cm}} \qquad \text{where:} \qquad \varepsilon_{c,el} = \frac{\sigma_c}{E_{cm}} \tag{2.12}$$

$\varepsilon_{c,creep}$ - Creep deformation of concrete
$\varepsilon_{c,el}$ - Elastic part of concrete deformations
$\varphi(t, t_0)$ - Creep coefficient

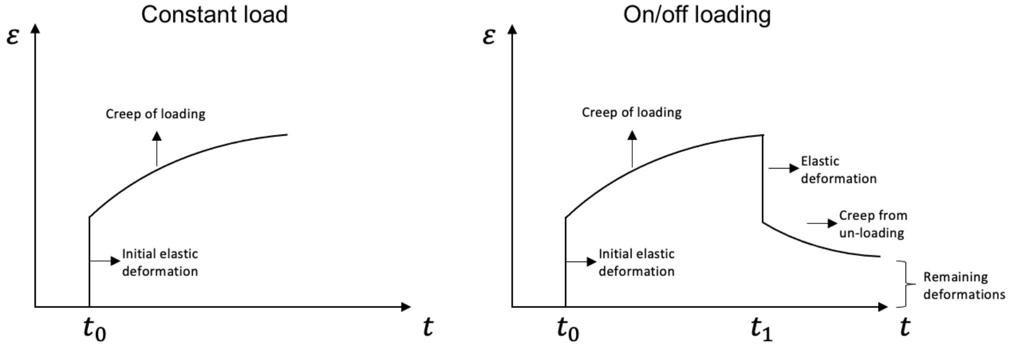

Figure 2.2: Principle response for concrete. a) Constant load, b) On/off loading, with load applied at time t_0 and unloading at time t_1. Adapted from [6].

2.5.2 Reinforcement steel

Due to the low tensile strength of concrete, reinforcement is often used together with concrete to increase the strength and reduce cracks in structures that are subjected to tensile stresses. There are several types of reinforcement steel on the market with varying treatment, quality, surface shapes and dimensions. The stress-strain relation for both cold formed and hot rolled steel can be seen in Figure 2.3, where it is also seen that hot rolled steel has a more ductile behaviour compared to the brittle behaviour of cold formed steel. The E-modulus is defined by the angle of the elastic part of the curve [6].

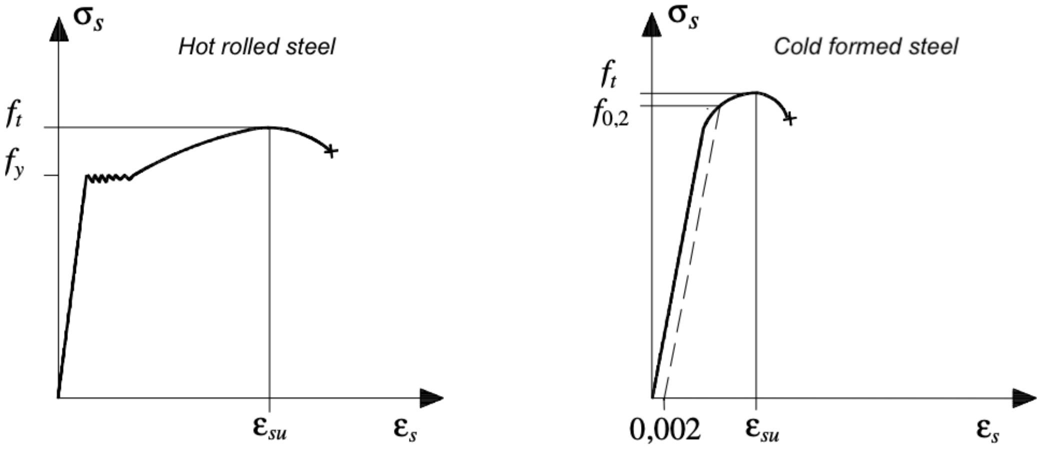

Figure 2.3: Stress-strain relation for steel. From [6].

The design yield strength for hot rolled reinforcement steel can be can be calculated according to Equation 2.13. For cold formed steel the 0.2 % proof strength is used instead of the characteristic strength. Commonly the strength of reinforcement steel is tested by a tensile test according to EN-standards. It is worth mention that behaviour and strength of steel is well known due to the homogeneity of the material and well-developed manufacturing methods.

$$f_{yd} = \frac{f_{yk}}{\gamma_s} \tag{2.13}$$

f_{yd} - Design yield strength of reinforcement
f_{yk} - Characteristic yield strength of reinforcement
γ_s - Partial factor for reinforcing steel

2.5.3 Prestressing steel

Prestressing steel is commonly made of cold-worked high-performance steel. The main types are prestressing-wires, -strands and -bars. A combination where several wires or strands are used together is called a tendon [1]. Tendons are stronger and are used in constructions where a higher compressing force is required. The tendons are placed inside of a duct and there are several setups for both anchorages and tensioning systems.

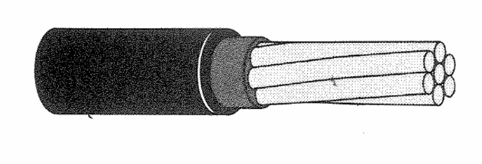

Figure 2.4: Example of 7-wire strand. From [6].

Due to the high stresses that are induced in the prestressing steel at tensioning, relaxation is an important load dependent phenomena that needs to be considered for this type of steel. There are several parameters that are effecting the degree of relaxation as, steel type, manufacturing technique, temperature and load duration [1]. Even though the relaxation degree often is defined by the manufacturer, Eurocode 2, [7], provides equations to approximate the relaxation factor. There are three classes that defines the relaxation class which makes it possible to estimate the relaxation factor after a certain time period according to Equation 2.14-2.16. Relaxation will have largest influence in the beginning after tensioning and will then stagnate with time.

$$\text{Class 1:} \quad \chi_t = 5.39 \cdot \chi_{1000} \cdot e^{6.7 \cdot \mu} \cdot (\frac{t}{1000})^{0.75(1-\mu)} \cdot 10^{-3} \tag{2.14}$$

$$\text{Class 2:} \quad \chi_t = 0.66 \cdot \chi_{1000} \cdot e^{9.1 \cdot \mu} \cdot (\frac{t}{1000})^{0.75(1-\mu)} \cdot 10^{-3} \tag{2.15}$$

$$\text{Class 3:} \quad \chi_t = 1.98 \cdot \chi_{1000} \cdot e^{8 \cdot \mu} \cdot (\frac{t}{1000})^{0.75(1-\mu)} \cdot 10^{-3} \tag{2.16}$$

χ_t - Relaxation factor at time t [-]
t - Time after tensioning [h]
χ_{1000} - Relaxation loss after 1000h at 20°C [-]
μ - Initial stress level for the prestressing steel (σ_{pi}/f_{pk}) [-]

2.5.4 RC/PRC structures

As mentioned in Chapter 2.5.2, reinforcement is commonly embedded into concrete to increase, mainly the tensile strength of the structure but it will also increase the compressive strength of the structure. To utilize the full capacity of a reinforced concrete (RC) element, the concrete must crack before the reinforcement will be activated and contribute to the global strength. As commonly known, cracking is in many cases connected to issues and can decrease the lifespan of an element.

To delay cracking, commonly in SLS, prestressing can be used. The compressive force that is induced into the structure will counteract the tensile stress induced by the service load and will thereby prevent cracking, Figure 2.5.

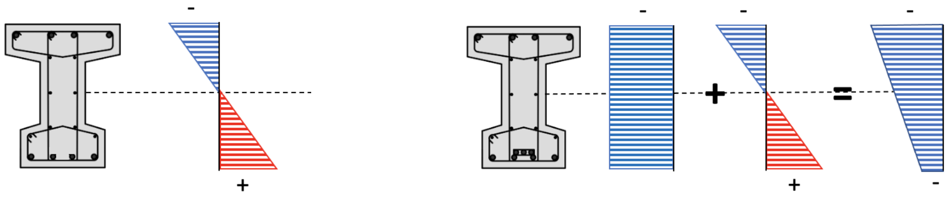

(a) Stress distribution RC **(b)** Stress distribution PRC

Figure 2.5: Stress distribution RC/PRC.

The SLS load will be carried by the uncracked concrete but the ultimate capacity of the structure will not increase due to the prestressing force [2]. Engström, [1], comparing a RC beam and a PRC beam with the same dimensions, cross-sectional area and same amount of tensile reinforcement subjected to the same load magnitude. In Figure 2.6 the result is shown and it is clear that the RC beam will crack at an earlier stage due to the induced axial force from the prestressing. It is also clear that the deflection for the same load magnitude is considerably smaller for the PRC beam compared to the RC beam.

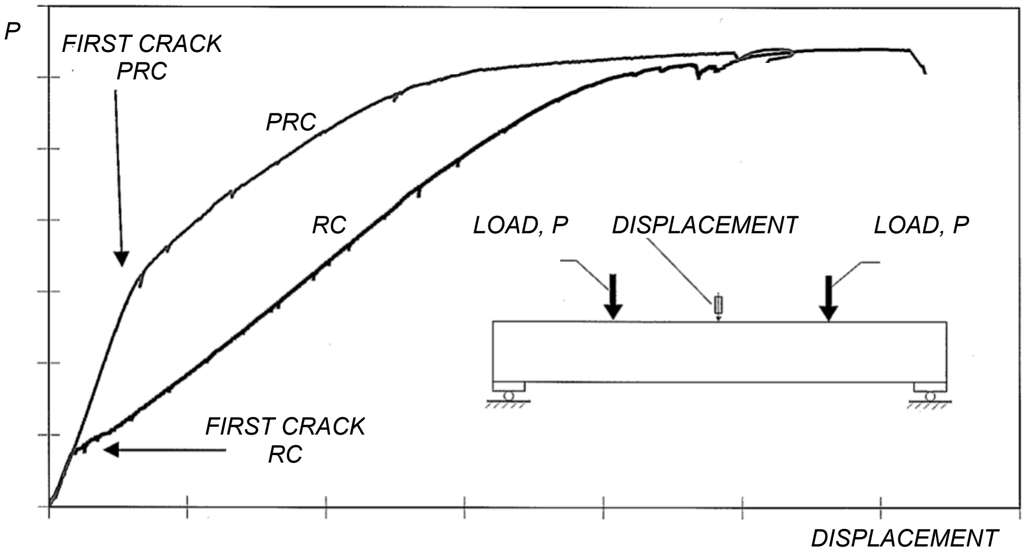

Figure 2.6: Load displacement comparison RC/PRC beams. Adapted from [1].

Looking at an environmental point of view, prestressing implies that design conditions can be met using less material. Thus, reducing material leads to a more sustainable construction method [2]. Additionally, sustainability implies resilience. Prestressed concrete infrastructures are great candidates for recycling into new uses.

2.6 Structural health monitoring systems

According to [5],[8], implementing structural health monitoring (SHM) systems on both existent and upcoming civil structures could be beneficial in several aspects, when SHM is used to evaluate the performance and health of structures. Data retrieved from monitoring structures could give important information about the structures health and performance and give indicators of weaknesses or damages. This is beneficial in a sustainable point of view since it would both simplify inspections, create prerequisites for preventive maintenance, more efficient structures and decrease the risks for collapsing structures. In both old and modern civil engineering structures, SHM is not commonly used due to lack of affordable solutions that has a stable and accurate performance [8].

2.6.1 Optical fiber sensors

In the last decades, researchers have found out that Optic fiber sensors (OFS) of different types can be used to measure the behaviour of structures in real-time. OFS has shown several benefits such as a high durability, low weight, good stability and good resistance against both corrosion, chemicals and electromagnetic fields [5]. There are several types of OFS and measuring techniques and they all have different benefits and drawbacks. The main drawbacks with one of the most common technique, Fiber Bragg grating (FBG) is the limitation of numbers of measuring points along the fiber length. This could result in uncertainties of the actual health of a structure since data of critical sections could fall out of the measuring scope [9]. In later years researchers has developed Distributed optic fiber sensors (DOFS), which take advantage of the full fiber length and gives a spatial resolution and accuracy incomparable to the older developed systems with point measuring. The type used in this study is DOFS and will be further explained in the upcoming sections.

The technique behind fiber optics is based on light transmittance and optical scattering. By measuring difference in amplitude, frequency, phase and polarization of the backscattered light it is possible to obtain strain(ε) and/or temperature(T) variation along the whole fiber, using only one connecting point at the end of the fiber [10]. Brillouin scattering, Raman scattering and Rayleigh scattering are the three different working principles used for DOFS [8]. According to [5], the working principles, differs in their usage area and their sensitivity of measure temperature and strain. Raman is mostly used in other applications than civil engineering and is sensitive to temperature measurement. The other two mentioned principles are sensitive to both temperature and strain measurements but differs in range and resolution. Brillouin scattering has a measuring range up to 300 km and a spatial resolution of about 10 cm. This compared to Rayleigh which has a substantial lower measuring range of maximum 100m but instead a substantially higher spatial resolution with a distance between each measuring point of less than a millimetre [5].

Optical Frequency Domain Reflectometry (OFDR) is the base of Rayleigh scattering. A reference state of the scattering pattern is stored before any "load" is applied to the fiber. When the fiber is subjected to strain or temperature changes the spectral shift that occurs can be compared to the reference state and the corresponding strain or temperature can be determined [9], see Figure 2.7. In conditions where the temperature is stable and known, as in a lab for example, the temperature effect on the strain in the fiber is considered as small and can be neglected in the global analysis of the structure [5].

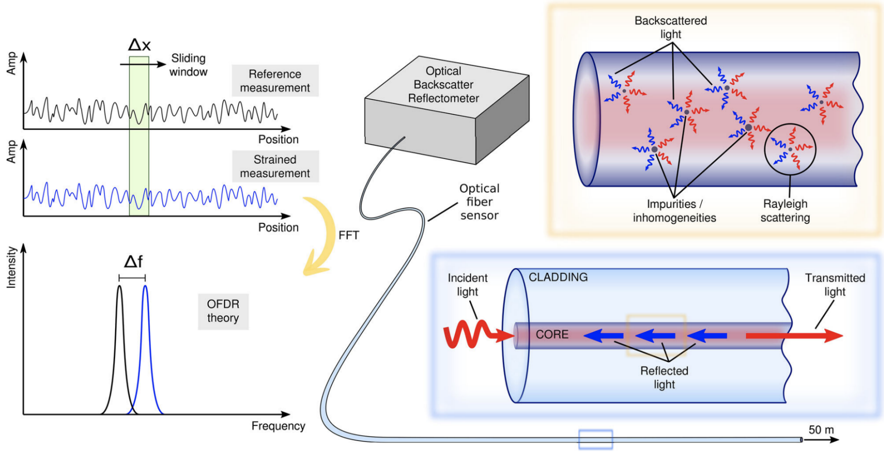

Figure 2.7: The principals of Rayleigh Backscattering based on OFDR. From [9].

2.6.2 Usage of DOFS monitoring concrete structures

There are several ways of installation of DOFS in concrete structures. The placement of the DOFS is of big importance to ensure the accuracy of the measured data but there is no standardized way of implementation. Berrocal *et al.* [5] mention in their work that there are a lot of parameters that can influence the performance of the DOFS, and therefore it is important to take these parameters into account before deciding both the placement and the mounting method. Some parameters can for example be geometry of the structure, type of fiber, type of structure, sought outcome and type of equipment. In the work it is also mentioned that the most common methods of mounting DOFS is:

- Attached to existent concrete surface.
- Embedded into concrete while casting.
- Attached to reinforcement surface or into a grove in the reinforcement bar before casting.

All these methods have shown successful results used analysing RC structures, but it is important to keep in mind that the cladding of the fiber and the attachment method used, can also influence the strain transfer between the mother material and the measuring fiber.

3

Design of specimens

The design of the specimens was the first step of the project. A preliminary design was first completed, assuming gross values and parameters. The results were then analysed in an accurate design for verification. This part of the project was performed to later have a reasonable specimen design that is suitable for the nature of the project and can withstand post-tensioning. The complete calculation is made in Appendix A.

3.1 Material properties

The project was limited in a few aspects. The beams were limited by the manageability to move them efficiently after casting, which affected the length and weight of the beams. Even though longer beams practically would have given a more realistic experiment they were decided to have a length of 8 m. The maximum weight the overhead cranes in the structural engineering lab at Chalmers could carry was 5 tons, which then were decided as the upper weight boundary per specimen. The concrete properties used in the casting is presented in Table 3.1.

Table 3.1: Concrete properties.

Concrete class	C50/60
Cement	CEM II/A-LL 42,5R
D_{max}	16 mm
f_{cm}	65.6 MPa
Standard deviation, σ	2.437 MPa

The reinforcement that was available for the construction of the specimens were of type and dimensions according to Table 3.2. The provided reinforcement were straight bars with a length of 6 m.

Table 3.2: Reinforcement properties.

Diameter, ϕ	6, 8 ,16 mm
Type	K500C-T

The post-tensioning system was manufactured and delivered by CCL Spännarmering. The used system was an XF Live-end anchorage, consisting of XF20 anchorage system and a roll-formed flat metal duct.

Figure 3.1: Anchorage of post-tensioning system. From [11].

In Table 3.3 and 3.4 the properties of the post-tensioning system are listed.

Table 3.3: Post-tensioning system - Strand properties.

Steel designation	Y1860S7
Nominal diameter	15.7 mm
Tensile strength, f_{puk}	1860 MPa
Steel area, A_{pi}	150 mm^2
Breaking load, $f_{puk} \cdot A_{pi}$	279 kN
0.1 % proof load	246 kN
Max strand load, $0.8 \cdot f_{puk} \cdot A_{pi}$	221 kN

Table 3.4: Post-tensioning system - Duct properties.

Inner duct height	18 mm
Inner duct width	69 mm
Duct wall thickness	4 mm
Duct area	1174 mm^2

3.2 Preliminary design

Firstly, a preliminary design was made according to [1] based on Eurocode 2. The cross-section geometry was decided to be made as an I-section, with flanges at top and bottom, and a web. The dimensions were assumed in the first iteration, but later adjusted to fulfil the criteria of the project.

3.2.1 Sectional constants

The sectional constants were initially calculated using the gross concrete area of the cross-section. Because of the symmetry in the I-section, the centre of mass was calculated as a function of the height of the cross-section. The second moment of inertia was calculated with respect to the y-axis, as the test loads only were applied vertically on the beam.

$$\bar{x}_c = \frac{1}{\sum m_i} \sum m_i \bar{x}_i \tag{3.1}$$

$$I_c = \sum I_i + A_i(\bar{x} - \bar{x}_i)^2 \tag{3.2}$$

$\bar{x}_c$ - Centre of gravity for gross concrete section
$\bar{x}_i$ - Centre of gravity
m_i - Mass
I_c - Second moment of area for gross concrete section
A_i - Sectional area

3.2.2 Stress limitations

As the beam is designed as a fully prestressed member, no cracks are allowed in the tensioning stage, nor in SLS. This meant that different equations were established for different phases. After the post-tensioning, it was of interest to limit stress in the top edge, as this were where tension occur. As the tendon profile followed the moment distribution, the cross-section of interest is in the middle of the beam, where maximum moment is present for a simply supported beam with two symmetrical placed point loads.

Top edge in tension:

$$\sigma_{cti} \approx \frac{-P_i}{A_c} + \frac{-P_i e + M_{g0}}{I_c}(-\bar{x}_c) \leqslant \sigma_{cti,max} \tag{3.3}$$

Bottom edge in compression:

$$\sigma_{cti} \approx \frac{-P_i}{A_c} + \frac{-P_i e + M_{g0}}{I_c}(h - \bar{x}_c) \geqslant -|\sigma_{cci,max}| \tag{3.4}$$

M_{g0} - Bending moment due to self-weight of the prestressed member
e - Eccentricity
h - Height

After the load is applied, the top edge shifts from be in tension to compression, and vice versa in the bottom edge. Then the following equations were established. In the preliminary stage a factor η was used to consider long-term effects, as creep and shrinkage [1].

Top edge in compression:

$$\sigma_{cc\infty} \approx \frac{-\eta P_i}{A_c} + \frac{-\eta P_i e + M_{g0} + M_{qt}}{I_c}(-\bar{x}_c) \geqslant -|\sigma_{cc\infty,max}| \tag{3.5}$$

Bottom edge in tension:

$$\sigma_{ct\infty} \approx \frac{-\eta P_i}{A_c} + \frac{-\eta P_i e + M_{g0} + M_q}{I_c}(h - \bar{x}_c) \leqslant -\sigma_{ct\infty,max} \tag{3.6}$$

M_{qt} - Additional long-term moment excluding moment due to self-weight
M_q - Additional maximum moment excluding moment due to self-weight
η - Reduction factor to account for long-term effects

3.2.3 Limits of the prestressing force

By using Equations 3.3 - 3.6, the prestressing force P_i was solved for each equation. After iterating values for eccentricity, point loads, and adjusting the cross-section geometry, this gave an upper and lower boundary for the prestressing force.

$$P_i \leqslant \frac{M_{g0} + \frac{I_c}{\bar{x}_c}\sigma_{cti,max}}{e - \frac{I_c}{\bar{x}_c A_c}} \tag{3.7}$$

$$P_i \leqslant \frac{M_{g0} + \frac{I_c}{h-\bar{x}_c}|\sigma_{cci,max}|}{e + \frac{I_c}{(h-\bar{x}_c)A_c}} \tag{3.8}$$

$$P_i \geqslant \frac{1}{\eta} \cdot \frac{M_{g0} + M_{qt} - \frac{I_c}{\bar{x}_c}|\sigma_{cc\infty,max}|}{e - \frac{I_c}{\bar{x}_c A_c}} \tag{3.9}$$

$$P_i \geqslant \frac{1}{\eta} \cdot \frac{M_{g0} + M_q - \frac{I_c}{h-\bar{x}_c}|\sigma_{ct\infty,max}|}{e + \frac{I_c}{(h-\bar{x}_c)A_c}} \tag{3.10}$$

The lowest value of Equation 3.7 and 3.8 gave the upper limit of the tendon force, while the highest value of Equation 3.9 and 3.10 correspondingly gave the lower limit of the tendon force. All previously mentioned parameters were then adjusted until a reasonable gap was created for the prestressing force.

3.3 Accurate design

In the accurate design, long-term effects in form of relaxation, creep and shrinkage were verified through the design that was preliminary decided.

3.3.1 Stress limitation

After post-tensioning, concrete stresses were calculated according to Equation 3.11-3.12, where the initial prestressing force was used. After loading, more effects were considered, as effective prestressing force over time, shrinkage and creep, Equation 3.13-3.14.

After post-tensioning:

$$\sigma_{cti} = \frac{-P_{0i}}{A_{net}} \cdot \frac{-P_{0i}e_{net} + M_{g0}}{I_{net}}(-x_{net}) \tag{3.11}$$

$$\sigma_{cci} = \frac{-P_{0i}}{A_{net}} \cdot \frac{-P_{0i}e_{net} + M_{g0}}{I_{net}}(h - x_{net}) \tag{3.12}$$

A_{net} - Transformed net area
I_{net} - Second moment of area of net section
x_{net} - Centre of gravity for net section
e_{net} - Eccentricity net section

After loading:

$$\begin{aligned}\sigma_{cc\infty} =& \frac{-(1-\chi_\infty)(P_{0i} - F_{cs,p}) + F_{cs,s} - F^{'}_{cs,s}}{A_{I,ef}} + \\ &+ \frac{-(1-\chi_\infty)(P_{0i} - F_{cs,p})e_{p,ef} + F_{cs,s}e_{s,ef} - F^{'}_{cs,s}e^{'}_{s,ef} + M_{g0} + M_{qt}}{I_{I,ef}}(-x_{I,ef})\end{aligned} \tag{3.13}$$

$$\begin{aligned}\sigma_{cc\infty} =& \frac{-(1-\chi_\infty)(P_{0i} - F_{cs,p}) + F_{cs,s} - F^{'}_{cs,s}}{A_{I,ef}} + \\ &+ \frac{-(1-\chi_\infty)(P_{0i} - F_{cs,p})e_{p,ef} + F_{cs,s}e_{s,ef} - F^{'}_{cs,s}e^{'}_{s,ef} + M_{g0} + M_{q}}{I_{I,ef}}(h - x_{I,ef})\end{aligned} \tag{3.14}$$

$A_{I,ef}$ - Effective area, state I
$I_{I,ef}$ - Effective second moment of area, state I
$F_{cs,p}$ - "Shrinkage force" at the level of the prestressing steel
$F_{cs,s}$ - "Shrinkage force" at the level of the bottom reinforcement
$F^{'}_{cs,s}$ - "Shrinkage force" at the level of the top reinforcement
χ_∞ - Final relaxation factor

3.3.2 Moment capacity

In the first moment capacity control, the tendon strain reached yielding. This meant that the tendon strain was decisive for the moment capacity. Before crushing of concrete, $\varepsilon_{cu} = 3.5‰$, is reached, there is already yielding of the tendon. This was taken into account by assuming the tendon strain equal to the yielding strain, and thereby the concrete compressive strain will not reach ε_{cu}. Assuming the neutral layer in the web, the horizontal equilibrium was formulated in Equation 3.15. As ε_{cc} is a function of α_R and β_R, the deformation condition in Equation 3.16 was used until the correct value of the neutral layer was iterated.

$$\alpha_R f_{cd} A_{tf} + \alpha_R f_{cd} b_w (x - h_{tf}) + \sigma^{'}_s A^{'}_s - (\sigma_p A_p + \sigma_s A_s) = 0 \tag{3.15}$$

$$x = \frac{\varepsilon_{cc}}{\varepsilon_{cc} + \Delta\varepsilon_p} \cdot d_p \tag{3.16}$$

With the neutral layer known, the moment capacity was calculated using moment equilibrium in the level of the prestressing steel, according to Equation 3.17. The model for sectional analysis is presented in Figure 3.2.

$$\begin{aligned} M_{Rd} = \alpha_R f_{cd}(b_{tf} - b_w)h_{tf}(d_p - \beta_R h_{tf}) + \alpha_R f_{cd} b_w x(d_p - \beta_R x) + \\ + \varepsilon_s^{'} E_s A_s^{'}(d_p - d^{'}) + \varepsilon_s E_s A_s(d_p - d) \end{aligned} \tag{3.17}$$

ε_{cc} - Concrete strain at the compressed edge of the cross-section
ε_s - Bottom reinforcement steel strain
$\varepsilon_{s'}$ - Top reinforcement steel strain
A_{tf} - Sectional area of top flange
b_w - Width of the web
b_{tf} - Width of the top flange
h_{tf} - Height of the top flange
α_R, β_R - Stress block parameters
σ_s - Stress in bottom reinforcement
σ_s' - Stress in top reinforcement
σ_p - Stress in prestressing steel

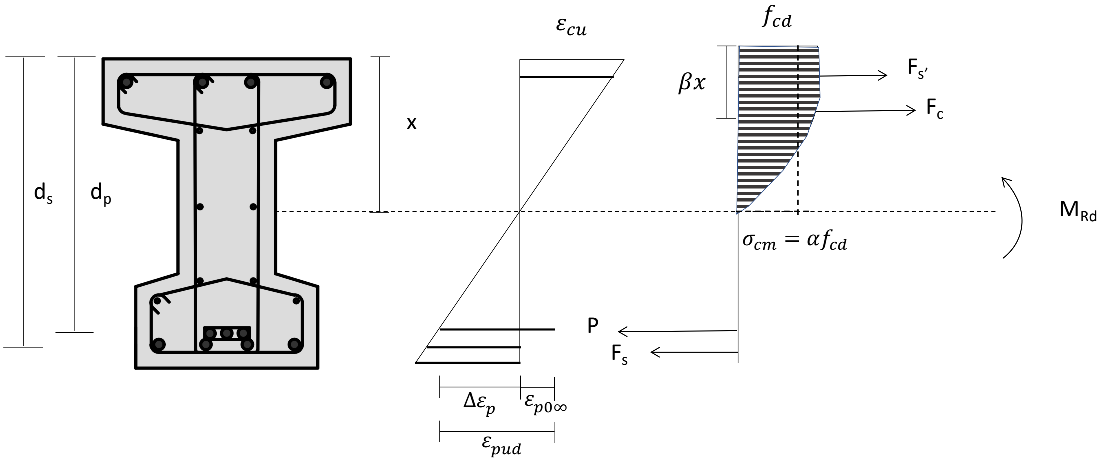

Figure 3.2: Model for sectional analysis.

3.3.3 Shear design

The first step of the shear design was to analyse the favourable effect of the inclined tendon. As the force in the tendon was inclined, a force component acted vertically to counteract the shear force when loaded. The net shear force was calculated using Equation 3.18.

$$V_{Ed,net} = V_{Ed} - V_{ipd} \qquad \text{where:} \qquad \begin{aligned} V_{ipd} &= \gamma_P \sigma_{p0\infty} A_p \tan\alpha_p \\ V_{ipd} &= P_d \tan\alpha_p \end{aligned} \tag{3.18}$$

V_{Ed} - Design shear force

V_{ipd} - Transverse component of inclined prestressing force
γ_p - Partial safety factor for prestressing steel

The next step was to check whether or not the beam could be considered cracked in bending. The critical section was found by assuming an 45° angle from the support and extracting the eccentricity in that location. Then, the stress was controlled in Equation 3.19.

$$\sigma_{ct} = \frac{-P_{0\infty}}{A_c} + \frac{-P_{0\infty}e_{crit} + M_{crit}}{I_c}(h - x_c) \leqslant \frac{f_{ctk,0.05}}{\gamma_c} \tag{3.19}$$

As compression was present, the next step was to determine the shear capacity $V_{Rd,cw}$, of uncracked concrete determined by web shear tension failure, see Equation 3.20.

$$V_{Rd,cw} = \frac{I_c b_w}{S}\sqrt{f_{ctd}^2 + \alpha_1 \sigma_{cp} f_{ctd}} \geqslant V_{Ed,net} \tag{3.20}$$

S - First moment of area of the cross-section

After realizing the capacity was sufficient, minimum reinforcement spacing, s, was designed for, according to Equation 3.21.

$$s = \min\left(\frac{2A_{sw}}{\rho_{w,min} b_w \sin\alpha}, 0.75d(1 + \cot\alpha)\right) \quad \text{where:} \quad \rho_{w,min} = 0.08\frac{\sqrt{f_{ck}}}{f_{yk}} \tag{3.21}$$

A_{sw} - Cross-sectional area of shear reinforcement unit

3.3.4 Design of anchorage zone

Due to unfavourable effects from prestressing force in the anchorage zone, the tendon force was multiplied with a partial factor according to Equation 3.22.

$$P_d = \gamma_p P \tag{3.22}$$

Using the strut and tie method, the tension tie in the anchorage zone was calculated, Equation 3.23. Assuming the tie width as b = half the height of the cross-section, and a = width of applied force, the force was evaluated. The reinforcement amount was then calculated.

$$\text{Tension tie:} \quad \frac{1}{2} \cdot \frac{b - a}{b}$$

$$T = \frac{1}{4} \cdot \frac{b - a}{b} \cdot P_d \tag{3.23}$$

$$\text{Reinforcement needed:} \quad \frac{T}{f_{yd}} \leqslant n 2\pi (\frac{\phi_{stirrup}}{2})^2 \tag{3.24}$$

The amount of stirrups, n, in the anchorage zone was then adjusted until Equation 3.24 was satisfied.

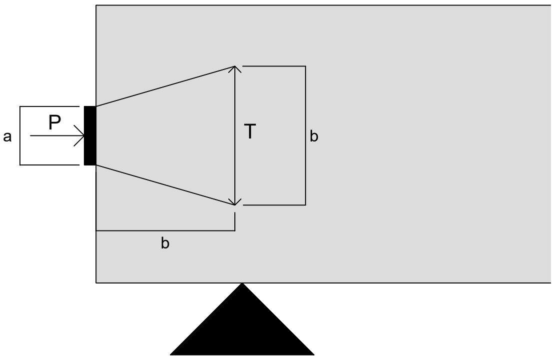

Figure 3.3: Strut and tie model of anchorage zone.

3.3.5 Final design

The final design of the beams are presented in Figure 3.4-3.5. The only thing that differentiates the two beams is that the duct and tendons are removed in the reference beam. At the two locations where the cross-section changes geometry, a smooth transition is created to avoid stress concentrations. These transitions are placed 400 mm in from the edges of the beam.

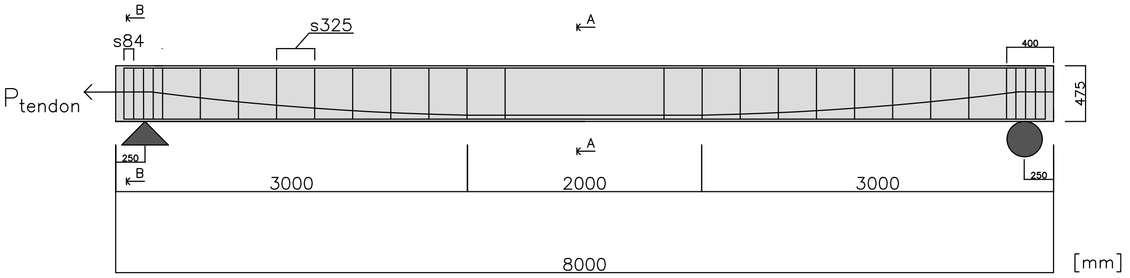

Figure 3.4: Sideview of the final design.

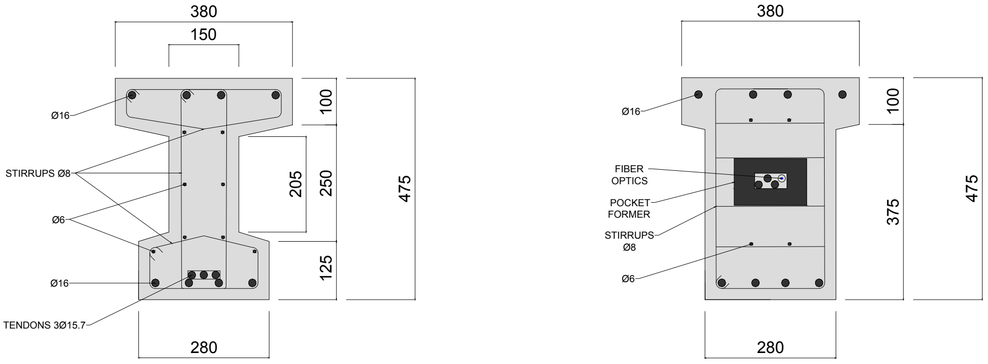

(a) Mid cross-section (A-A). (b) End cross-section (B-B).

Figure 3.5: Cross-section of the final design.

Figure 3.6 shows the moment and shear distribution in SLS and ultimate limit state (ULS) with the applied point loads.

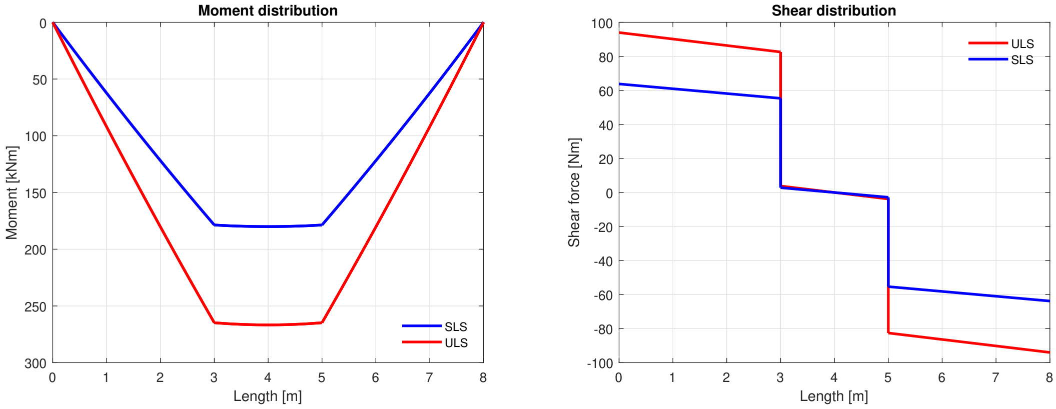

(a) Moment distribution.

(b) Shear force distribution.

Figure 3.6: Moment and shear force distribution. Self-weight included.

The point loads applied on the beams where iterated along with the other parameters regarding the design. In Table 3.5 the point loads, moment and shear force are compared to the design values.

Table 3.5: Loads and capacity.

State	Point load [kN]	Moment [kNm]	Moment capacity [kNm]	η [%]
SLS	52.5	180	320	57
ULS	78.75	267	320	83

4

Description of experiment

After the design of the beams were finalized, the rest of the project was carried out in different stages. These were construction of beams including installation of DOFS and casting, post-tensioning, and testing of the specimens. After the post-tensioning was finished the collection of strain data from the DOFS was initiated. The measurements were ongoing all the time from casting to the final four-point test of the beams. Simultaneously the data were post-processed.

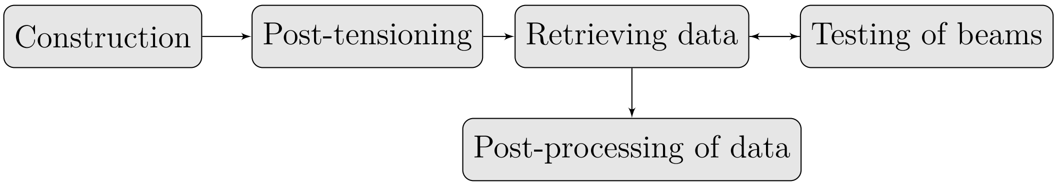

4.1 Construction

The construction of the beams was mainly performed in Betonghallen at Chalmers. The material processing was partly executed in The Architectural Workshop at Chalmers. The construction consisted of building the formwork, and installing the reinforcement cage, post-tensioning system and health monitoring system.

4.1.1 Formwork

After deciding the cross section of the beams, the building of the formwork initiated. Shuttering plywood was sawed out and acted as floor and walls for the concrete. As seen in Figure 4.1 and 4.2, wooden studs were used to support the construction, and EPS boards together with studs were used to create the I-section of the beams. Seen in Chapter 3.3.4, the cross section differs for mid and end span, visualized in 4.1a and 4.1b.

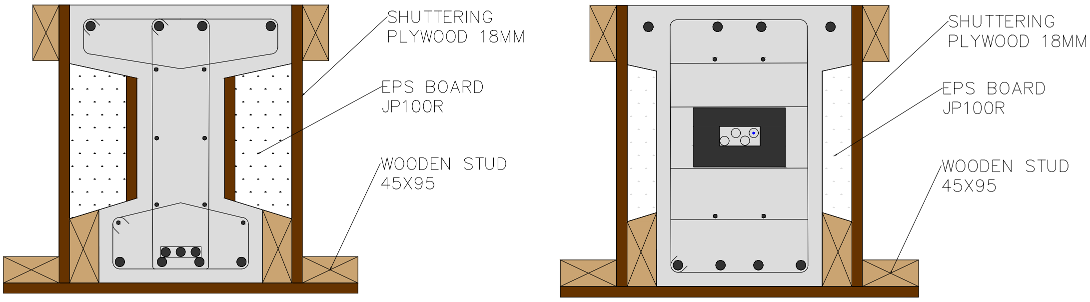

(a) Mid span.

(b) End span.

Figure 4.1: Illustration of formwork.

Firstly, the shuttering plywood floor were screwed from underneath and attached to the outer wooden studs. Then, the shuttering plywood walls were screwed onto the studs from the inside of the formwork. Stabilization was made between the connection of the shuttering plywood by vertical studs, and a supporting horizontal stud at the top of the formwork, seen in Figure 4.2.

The inner wooden studs, as well as the EPS board, was inclined to enable a smooth removal of the formwork after casting. The studs were screwed, and the EPS boards were initially glued, and later supported by another piece of scattering plywood, fastened by screwing through the EPS board.

At the ends span, the EPS board was, in a smooth transition, made the same depth as the inner wooden stud. Also, worth noting is that the installation of the EPS board had to be done after the installation of the lower reinforcement, as the width of the web made it hard to install it afterwards.

Figure 4.2: Construction of formwork.

4.1.2 Reinforcement cage

In smaller scale specimens, the installation of the reinforcement cage is usually made outside the formwork, and later installed by placing the finished cage form. Due to the size of the beams, as well as the I-shaped cross section, it was decided to build the reinforcement cage into the formwork directly. A reinforcement cutter was used to cut the reinforcement into the correct lengths, and a bar bending machine was used to shape the stirrups.

Because of the I-shaped cross section and inclination of the top and bottom flange, the stirrups were separated in the midsection. One type of stirrup for the top flange, one type for the web, and one type for the bottom flange. The stirrups in the flanges followed the inclined profile. Binding wire was used to connect the reinforcement to each other, and reinforcement distances were used to space the reinforcement from the formwork.

Figure 4.3: Reinforcement in formwork.

4.1.3 Post-tensioning system

The installation of the post-tensioning system was made simultaneously as the installation of the reinforcement. The shuttering plywood in each end of the beam was carved out to make space for the anchorage system, and to be able to pull through the prestressing steel. The aluminium duct, seen in Figure 4.4, was taped together with the anchorage system and placed in a parabolic shape throughout the beam.

When the duct was placed in the correct position and fixed to the reinforcement, the tendons were pulled through.

Figure 4.4: Anchorage of post-tensioning system.

4.1.4 Installation of DOFS

The DOFS used in this experiment were a robust type from Solifos named BRUsens V9, with an outer diameter of 3.2 mm and a strain rate of up to 10,000 µε. Outside of the fiber optic the wire consists of a steel tube and an external polyamide cladding to increase its durability and strength and to reduce the risk of rupturing. The DOFS was strategically placed along longitudinal reinforcement in both beams before casting of concrete, as seen in Figure 4.5. The optical fiber wire was placed back and forth in the beams since each wire was approximately 25 m. To decrease the usage of fiber, the reference beam were only equipped with fiber in the horizontal centre of the beam in in three layers (mid,top and bottom). The DOFS were bonded to the reinforcement using electrical tape. After the installation was made and the fibers were connected to the measuring device, the fibers were pinched at specific points at the ends of the beams to locate the position of start and end points of the fibers.

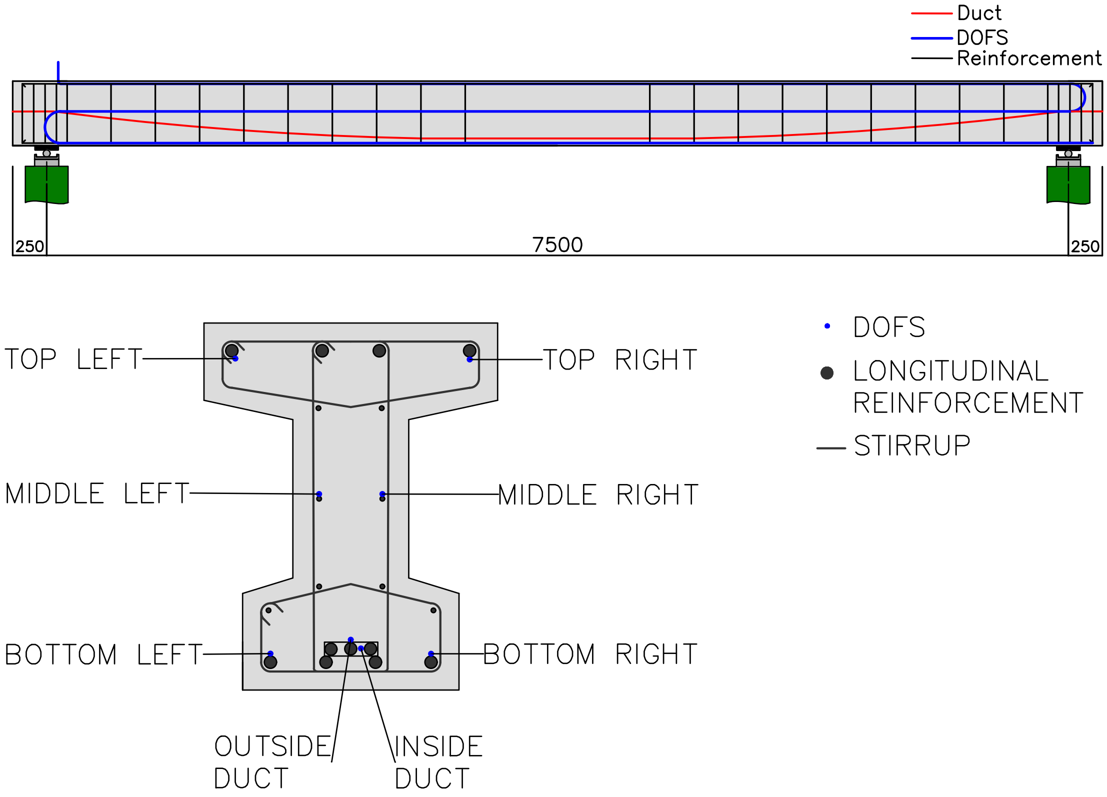

Figure 4.5: DOFS placement in the PRC beam.

4.1.5 Casting of concrete

After the formwork was constructed and the DOFS were installed, the casting of the beam started. Concrete according to Chapter 3.1 was used, and was provided by a concrete mixing transport truck. During the casting process, the concrete was vibrated to evenly spread the concrete in the formworks and to reduce the risk of air trapped in the concrete. Wooden supports were used at the top of the formwork to handle the forces created by the concrete.

After casting, the concrete was covered with a plastic layer to minimize the evaporation of water in the concrete during hardening. After four days, the formwork was completely removed from the beams, see Figure 4.6. They were simultaneously put on supports (simply supported) as long-term effects began immediately after removal.

The beams were both cast and stored in an indoor lab environment during the whole measuring time with a mean temperature of 22.3 °C and a mean relative humidity of 30.9%.

Figure 4.6: Specimens after casting and demoulding.

4.1.6 Post-tensioning

In the post-tensioning procedure, the prestressing steel was tensioned step by step according to manufacturer instructions [11]. As seen in Figure 4.7, an anchor head of steel was placed closest to the beam. The prestressing steel was brought through this piece, and wedges were used on each tendon, which bites into the steel block when tensioned. Next to the wedge, a larger steel tube was placed to be able to fit the hydraulic cylinder next to the other tendons. The process was controlled with a load cell placed between the hydraulic cylinder and the steel tube, to measure the force in the tendon. After the tensioning was finished, the duct was grouted using a mixture provided by the manufacturer CCL. This operation was performed 11 days after casting.

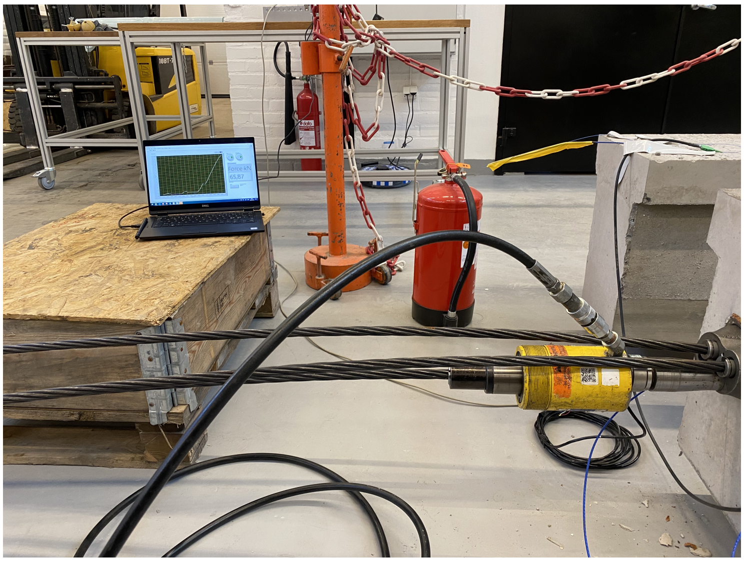

Figure 4.7: Set-up of post-tensioning.

4.2 Retrieving data

The Optical Distributed Sensor Interrogator (ODiSI) 6000 series from Luna Inc. was used as interrogator unit. It provides a strain resolution of 0.1 µε and a range of ±15000 µε.

The DOFS gave a strain output to a cloud-based database every 10 minutes. The strain output consisted of strain measurements every 2.6 mm along the fiber length. The interrogator has eight separated channels but only four channels were used, see Chapter 4.1.4. Each channel covered approximately three lengths of the beam, meaning that each measuring point needed to be correlated to the correct position in the beams.

4.2.1 Post-processing of data

Due to the DOFS placement, the raw data from the Fiber Sensor was processed to be able to interpret and compare data correctly. During the installation of the DOFS, as mentioned in Chapter 4.1.4, the optical wire was pinched at various locations to detect the location of the optical fiber in relation to the specimen. The raw data output consisted of approximately 25 m strain measurements, meaning that the data was both split in respectively direction, and aligned so the strain outputs corresponded to the same location in different fiber lengths.

The data was also refined, meaning that scatter and outliers where adjusted, and missing values where replaced, as seen in Figure 4.8. This smoothing operation was performed to minimize local disturbance and to optimize data storage.

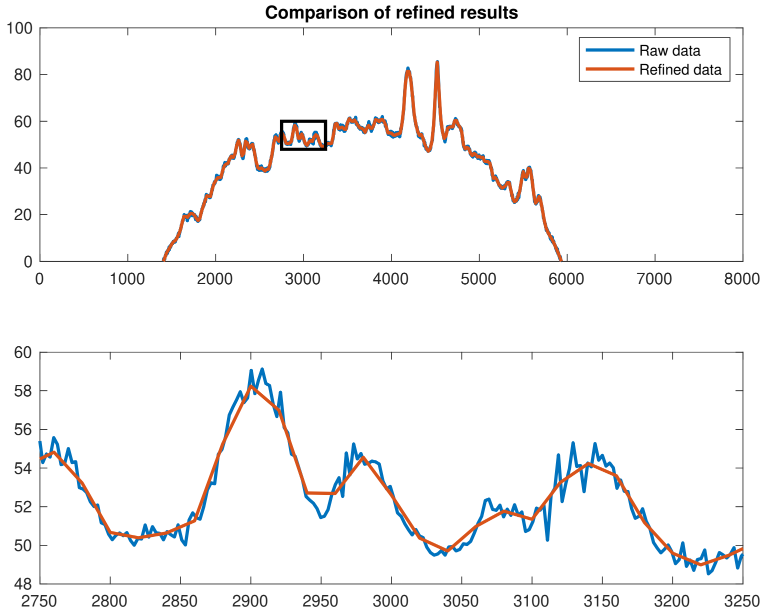

Figure 4.8: Comparison of refined results.

During the time of the data collection, some processing and calculations were made to be able to follow the behaviour of the beams in real time since the strain retrieved from the DOFS varies both in time and space. The curvature, rotation and deflection, which are key indicators to capture the behaviour of the beams were calculated according to Equation 4.1, 4.2 and 4.3.

$$\chi(x,t) = \frac{\varepsilon_{bottom}(x,t) - \varepsilon_{top}(x,t)}{z} \tag{4.1}$$

$\chi(x,t)$ - Curvature of the specimen
ε_{bottom} - Strain at the level of the bottom fiber
ε_{top} - Strain at the level of the top fiber
z - Distance between bottom and top fiber

$$\theta(x,t) = \int_0^x \chi(x,t)\,\mathrm{d}x \tag{4.2}$$

$\theta(x,t)$ - Rotation of the specimen

$$y(x,t) = \int_0^x \theta(x,t)\,\mathrm{d}x = \iint_0^x \chi(x,t)\,\mathrm{d}x \tag{4.3}$$

$y(x,t)$ - Deflection of the specimen

From the curvature of the beams, it was also possible to calculate the bending moment distribution over the length of the beams according to Euler–Bernoulli beam theory, Equation 4.4.

$$M(x,t) = -EI \cdot \chi(x,t) \tag{4.4}$$

$M(x,t)$ - Bending moment
EI - Flexural stiffness of the section

To approximate the strain at the level of the tendons, two approaches were used. One was that the strain of the fiber that was attached to the upper side of the duct, were assumed to have the same strain as the strain at the level of the tendons. In the other approach, the strain at the level of the tendons were interpolated from the strain difference between the top and bottom fiber, assuming a linear relation throughout the height of the cross section.

To calculate the relative loss of prestressing force in the tendons isolated from creep and shrinkage effects, the creep developed from the self-weight and the shrinkage had to be removed. Assuming that the above-mentioned effects were of the same magnitude in the same positions in the RC and the PRC beam those effect could be removed and the relative loss of prestressing force could be calculated according to Equation. 4.5. The relative loss is mainly developed from creep developed from prestressing force.

$$\Delta P = (\varepsilon_{PRC} - \varepsilon_{RC}) \cdot E_P \cdot A_P \tag{4.5}$$

ΔP - Relative loss of prestressing force
ε_{PRC} - PRC specimen strain
ε_{RC} - RC specimen strain

4.3 Testing

In the next phase of the project, several test methods were used to evaluate the performance and key indicators of the beams. Both individual material samples and the beams were tested. During testing of the beams, data from the DOFS were collected. During the final four-point bending test of the beams, Digital Image correlation (DIC) were used to compare the strain from the DOFS with the actual cracks capture by DIC pictures of the specimens.

4.3.1 Long-term test

In the long-term test, the simply supported specimens were monitored over time to detect strain changes mainly due to long-term effects. The test was initiated at the same day as the post tensioning was performed by tare the DOFS and lasted for 44 days. During this time the DOFS gave a strain output every 10 minutes. Both the reference beam and the PRC beam were monitored with the same settings and the same measuring unit.

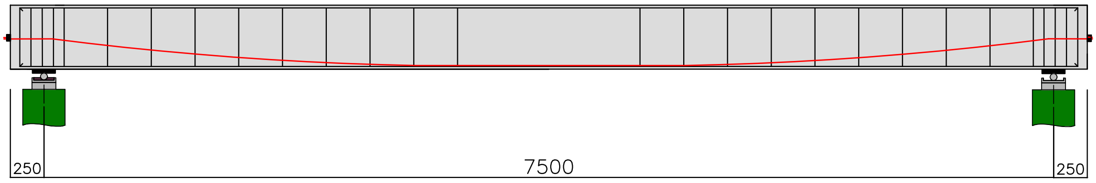

Figure 4.9: Setup for long-term test.

4.3.2 Pre-cracking of specimen

As a first step of the capacity testing of the specimens, the PRC beam was put through a cyclic loading test. The cycles had random magnitudes up to 60 kN per point and varied for varying time periods. Since a distribution beam transferred the load from the actuator to the tested beam, Figure 4.10, the load from the actuator was divided by two assuming even distribution between the two loading points. The cyclic loading test lasted for seven days and was performed directly after the long-term test. Since the main part of this test was outside the scope of this thesis the focus will be on the cycles where the beam was pre-cracked. The pre-cracked loading ramps can be found in Figure 4.11, and the purpose of this test was only to initiate cracking in the bottom of the PRC specimen and track the behaviour at lower load levels.

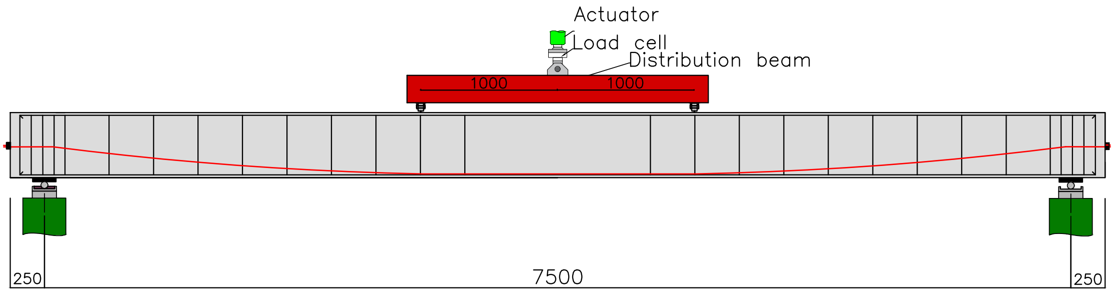

Figure 4.10: Setup for pre-cracking.

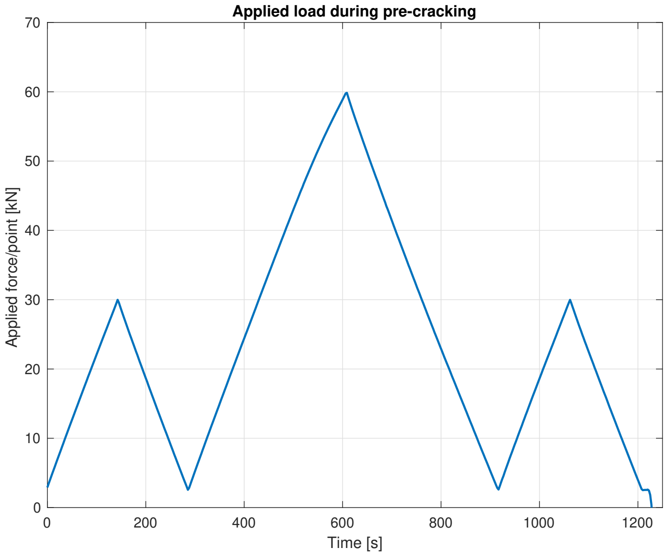

Figure 4.11: Load cycles during pre-cracking of the PRC specimen.

4.3.3 Four-point bending test

The final test of the beams was a destructive maximum test where the beams were tested until failure. The loading setup was according to Figure 4.12, where the point loads were placed 3m in from each side of the beam and separated 2m from each other. Due to the relative high capacity of the beams, the required load to failure was not sufficient using only one actuator and a distribution beam so two actuators had to be used. Since the controlling of the actuators were individual for each one, the load applied needed to be controlled by the displacement of the cylinder instead of controlled by force. By setting an individual displacement pace for each actuator it was possible to balance and apply the same load from each one of the point loads.

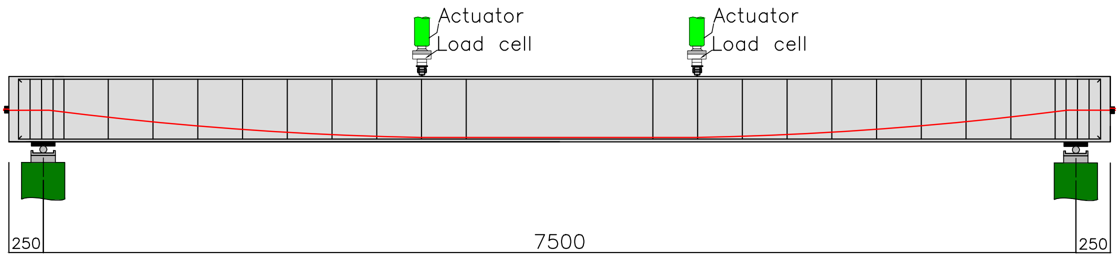

Figure 4.12: Setup for failure test.

During the tests of both beams, the response was recorded using Digital Image Correlation (DIC). The two cameras used, recorded the middle of the beams with a spectrum capturing a width of approximately 1.35m. The cameras using a black and white stochastic pattern as a reference and then comparing changes in the pattern to capture the strain fields and to create a 3D-model. The pattern were painted on the beams, see Figure 4.13, and reference stickers were placed in the middle of the beam to be able to identify the position of the pattern in relation to the beams. This simplifies and increases the accuracy during post processing of the images and comparison with the measured strain from the DOFS.

Figure 4.13: Setup for DIC and stochastic pattern on the specimen.

4.3.4 Material testing

To make sure that the concrete used fulfils the given manufacturer properties, a concrete cube test was performed at two different occasions. The first test was performed approximately 28 days after casting and the second one at 63 days after casting. The five test cubes were casted at the same occasion as the beams and were after hardening stored in a water tank. The dimension of the cubes were 150x150x150 mm and the testing followed the protocol according to European Standard [12]. At the first occasion two of the cubes were tested and at the second occasion the remaining three. Figure 4.14 shows the testing machine and the procedure.

(a) Test setup.

(b) Specimen after testing.

Figure 4.14: Concrete cube strength test.

The results from the cube test can be found in Table 4.1-4.2. The cylinder compressive strength for the concrete could be calculated from the cube test according to Equation 2.6. The standard deviation for the 28-day test was 1.19 MPa and 1.76 for the 64-day test. The red-marked text in Table 4.2 indicates the cubes that did not fulfil the required crack pattern according to the standard protocol [12]. Since this is a subjective assessment, the results from those cubes are still presented in the test results.

Table 4.1: Cube test at 28-days.

Cube nr	ρ [g/m^3]	Applied force [kN]	σ [MPa]	f$_{cm}$ [MPa]
1	2.53	1508.91	67.06	55.88
2	2.5	1470.89	65.37	54.48
Mean strength			66.22	55.18

Table 4.2: Cube test at 64-days.

Cube nr	ρ [g/m^3]	Applied force [kN]	σ [MPa]	f_{cm} [MPa]
3	2.53	1543.23	68.59	57.16
4	2.51	1596.84	70.97	59.14
5	2.52	1519.49	67.53	56.28
Mean strength			69.03	57.53

The reinforcement used in the specimens were also tested to control the strength of the steel. The test was conducted with five test samples of each rebar size used in the beams, ϕ6 mm, ϕ8 mm, ϕ16 mm. The bars were tested in a tensile test, see Figure 4.15, and pulled until failure. The test specimens had a length of 400 mm and the distance between the clamps in the testing machine were 293 mm for the smaller dimensions of reinforcement and 254 mm for ϕ16 mm bars. To increase the accuracy of the measured elongation of the steel bars and capture the steel behaviour even at lower loads, an extensometer was used to measure the strain in the beginning of the test. The extensometer was limited in elongation and to avoid failure, the test was paused during the procedure and the extensometer was removed. This pause can be seen in the stress-strain result curves where a small gap can be found where the data from the extensometer have been matched up together with the stress-strain data from the testing machine.

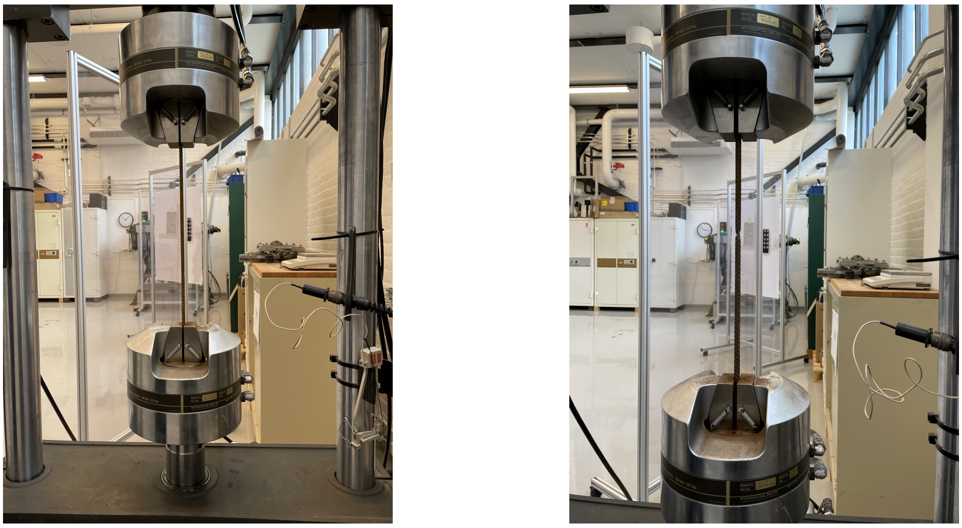

(a) Test setup. **(b)** Bar after test.

Figure 4.15: Reinforcement tensile test.

The results from the test of the five sample of each dimension are presented in stress-strain graphs, Figure 4.16- 4.18 and the mean values are compiled in Table 4.3. As seen in the figures, all the samples followed the same behaviour and lived up to the expected properties given by the manufacturer.

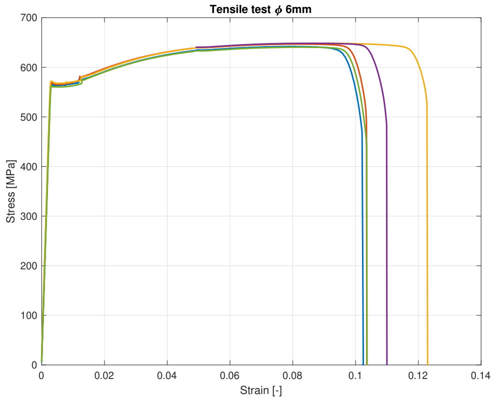

Figure 4.16: Tensile test results ϕ 6mm reinforcement.

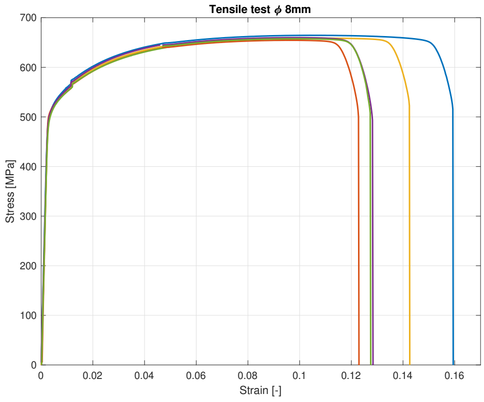

Figure 4.17: Tensile test results ϕ 8mm reinforcement.

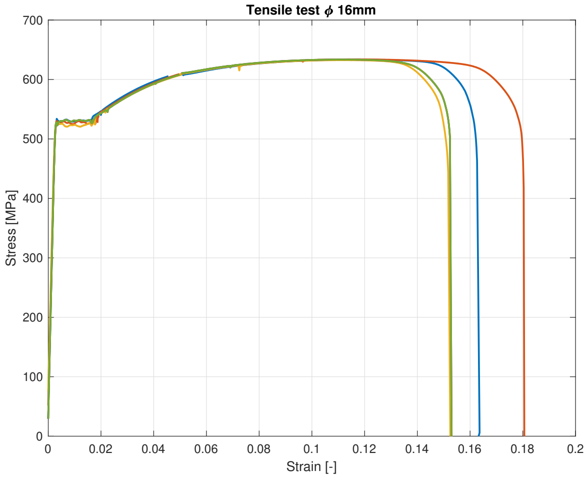

Figure 4.18: Tensile test results ϕ 16mm reinforcement.

Table 4.3: Average reinforcement properties from testing.

Dimension [mm]	E_s [GPa]	f_y [MPa]	f_u [MPa]
ϕ6	189	566	642
ϕ8	167	500	660
ϕ16	176	528	633

5

Results and Discussion

In the results and discussion chapter the main subject of interest is to present and evaluate the prestressing force. Though, complementary results will be presented and discussed in the form of strain, curvature, rotation, deflection and moment distributions. The main results will be divided in four subcategories, describing the initial phase, the long-term results, the pre-cracking and the final four-point bending test. In the end, results will be compared to theoretical calculations.

Unfortunately, the distributed optic fiber sensors did not registered strain at the final four-point bending test for the PRC specimen. Though, as pre-cracking was performed for the PRC beam up to 60 kN/point load, the results from this phase will be considered the same and used for comparison at the four-point bending test.

5.1 Initial phase

In the initial phase, results are presented around the time where the post-tensioning was performed. In Figure 5.1, the refined strain output directly after post-tensioning is presented for the post-tensioned specimen. As seen, the achieved strain is a behaviour that was expected. The prestressing force causes an axial force in the whole specimen, meaning that where the curvature is zero, i.e., where $\varepsilon_{top} \approx \varepsilon_{bottom}$, there is still a negative strain.

For the top fibers, positive strain was registered in the middle section, due to post-tensioning. There is some difference between the right and left fiber, which might be an effect of some rotation when tensioning the steel, but overall the alignment is accurate. For the middle fiber, the tendency indicates a slightly parabolic shape, which is a result of the placement of the fiber. If the fiber was placed in the natural layer the shape would be constant. As the fibers were placed in the vertical center of the cross section, the parabolic shape is expected. The DOFS in the middle of the beam were also attached to 6 mm reinforcement bars, which might have affected their position during casting, due to the concrete heaviness compared to the relatively small stiffness of the reinforcement. This result reduces the reliability for the DOFS in the middle of the PRC specimen.

At this phase, the bottom fiber is where the beam experiences the most compression, as expected due to the post-tensioning. The right and left fiber follows each other well. Also, the behaviour of strain from the fiber placed on top of the duct was expected. The difference in strain to the bottom fiber was small in the middle section where the duct is closest to the bottom edge and increased the further out it goes due to the parabolic profile of the duct. Overall, it can be said that the result from DOFS to measure strain in the specimens followed the expected behaviour.

Worth noting is that the strain was tared just before post-tensioning. This explains why the strain inside the duct is close to zero, as the grouting of the duct occurred after the post-tensioning, and the steel were able to move freely during the tensioning. Unfortunately, the DOFS inside the duct was clamped at one location, seen in Figure 5.1, when tensioning the tendons, but this did not change the result significantly. This also meant that the presented results were not the true strain, as effects from bending due to self-weight was neglected when taring the strain. As the strain was measured in the RC specimen as well, the neglected part was known at the time for taring and could thereby be verified as considerably small.

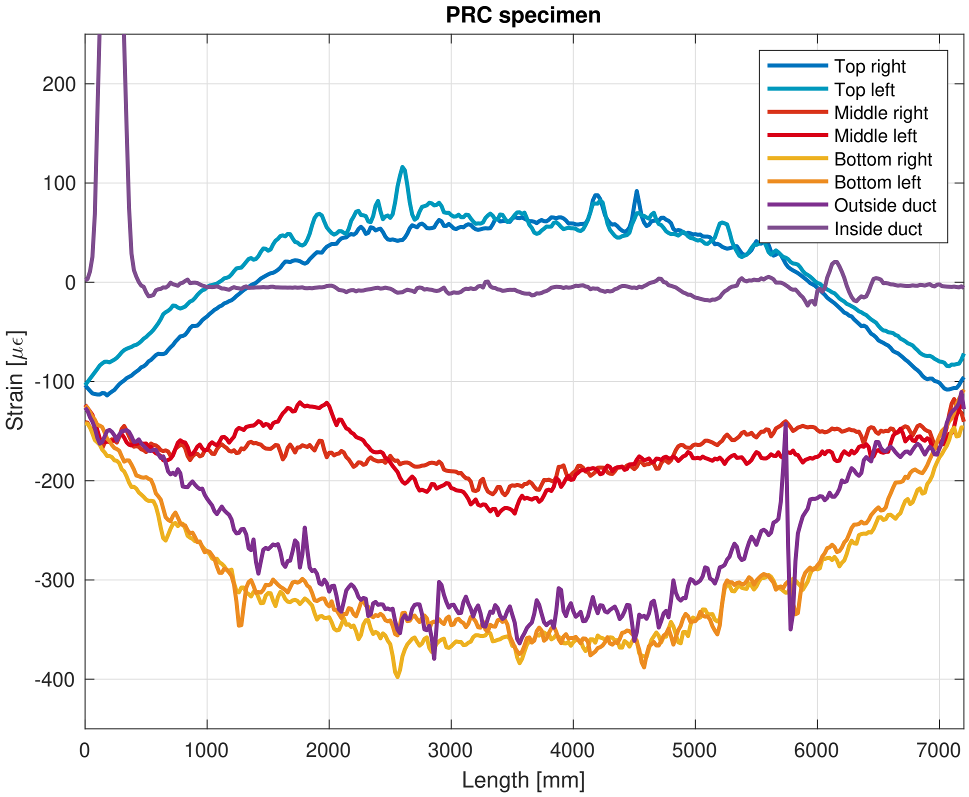

Figure 5.1: All refined strain data for PRC specimen.

Using the strain output for the top and bottom fibers, the curvature was calculated, as seen in Figure 5.2. As the curvature has the same shape of curve as the bending moment, the curve was found reasonable, due to having the same shape as the profile of the duct. Using boundary conditions at the supports and refining the curvature graph, the rotation could be calculated by integrating the curvature. Then, integrating the rotation correspondingly gave the deflection of the PRC specimen after post-tensioning.

The graph shows an inverted behaviour compared to a traditional reinforced specimen loaded in bending, as the post-tensioning gives an opposite effect. Notice that the deflection of the specimen is positive, meaning that the beam is bent upwards by the post-tensioning. This is reasonable, as the effect from post-tensioning will give an inverted deflection.

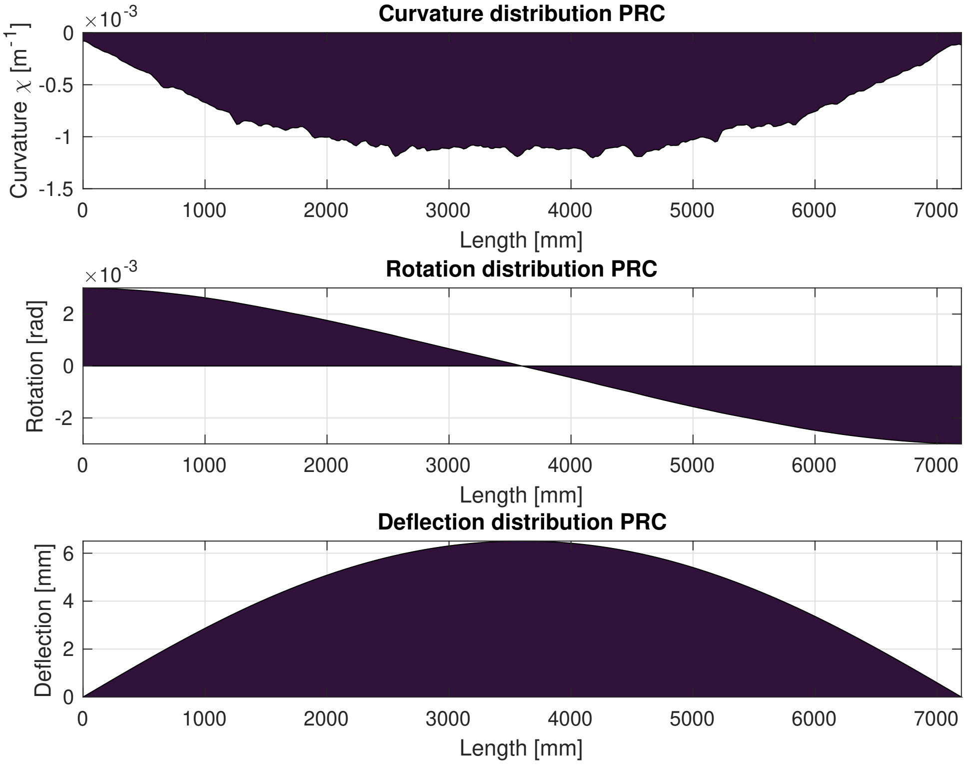

Figure 5.2: Curvature, rotation and deflection for PRC specimen in initial phase.

Looking at a small time interval during the tensioning procedure of the PRC specimen, an interesting phenomena can be traced. As seen in Figure 5.3, where strain on the duct and strain in bottom fiber is described over time in the middle section, the concrete behaviour from wedge penetration can be both seen and magnified.

Obviously, the effect from wedge penetration will differ between the active and passive prestressing edges. By tracing the behaviour in the middle section, a mean value of the wedge penetration is captured. This strain set back is not the same as in the prestressing steel, because at this stage the prestressing steel is not grouted, and thereby there is no bond between steel and concrete. The prestressing steel moves freely in relation to the specimen between the anchorages at both sides.

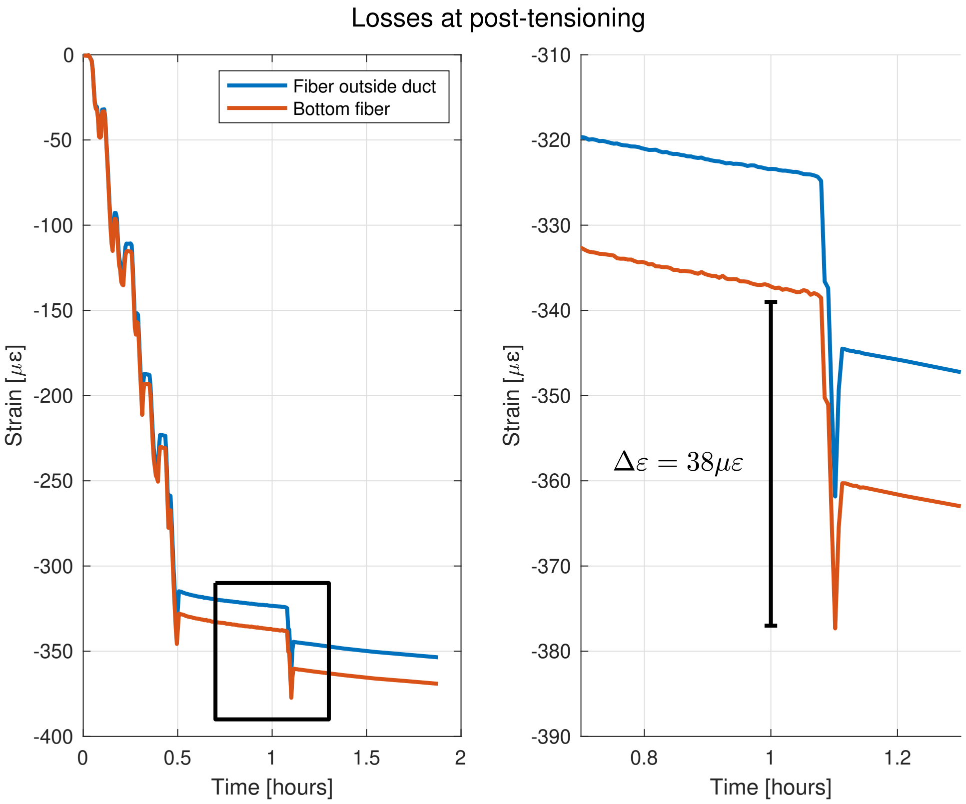

Figure 5.3: Initial losses during tensioning procedure.

The bending moment distribution was calculated by multiplying the curvature χ by the sectional rigidity EI. By comparing the moment distribution to the eccentricity of the prestressing steel, seen in Figure 5.4, it was found that the two graphs had more or less the same shape, implying that the prestressing force, calculated by dividing the moment by the eccentricity, were more or less constant over the length of the specimen.

Due to uncertainties of the tendon eccentricity in the inclined parts, only the mean prestressing force of the middle section, between the point loads, was calculated. In reality, the tendon profile had a third-degree polynomial shape, as the slope of the duct was zero both at the middle section, and in both ends due to the configuration of the anchorage.

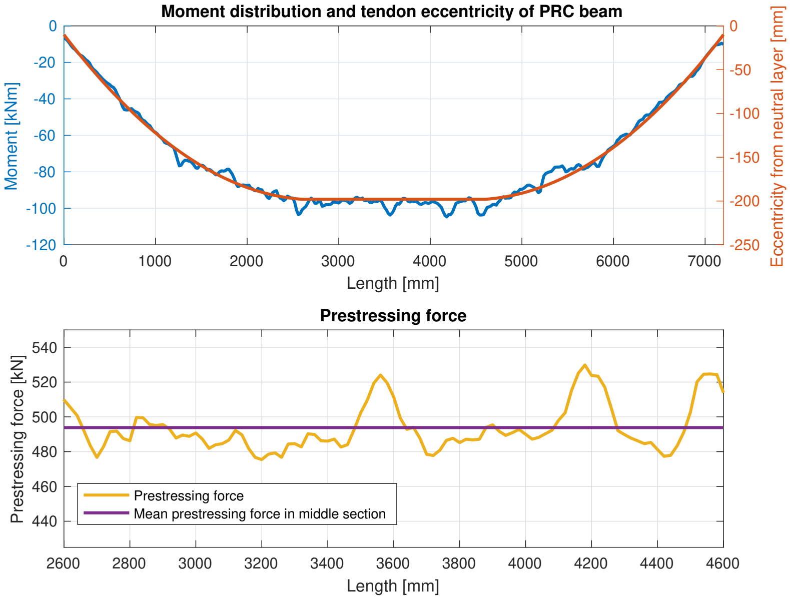

Figure 5.4: Moment, eccentricity of tendon and calculated prestressing force in initial phase.

By calculating the mean value of the prestressing force in the middle section for every time step during the post-tensioning, the prestressing force variation could be visualized. As seen in Figure 5.5, the different phases of the tensioning could be interpreted, as the tendons were tensioned after each other. Just as in Figure 5.3, the wedge penetration can now be seen and magnified in the form of a force loss that directly corresponds to the force loss in the prestressing steel for the middle section.

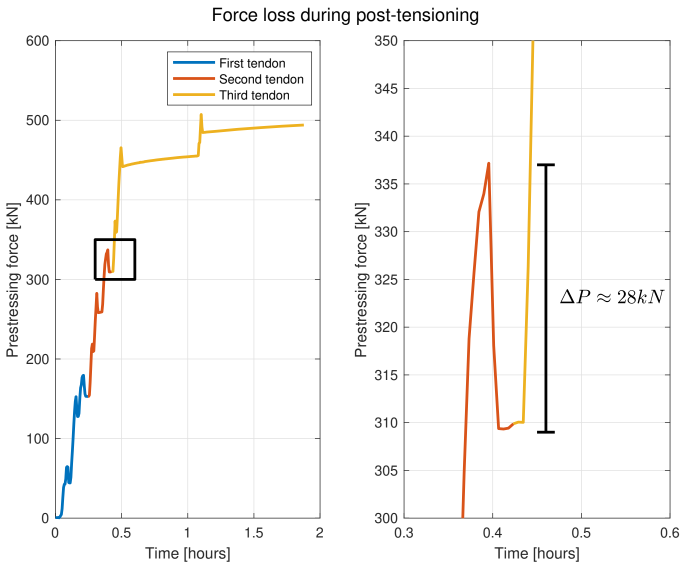

Figure 5.5: Mean prestressing force and loss during post-tensioning.

Considering the force loss obtained after tensioning procedure, the total prestressing force could be found. Figure 5.6 show how the hydraulic jacks load cell force output, which was considered accurate, varies when tensioning the tendons. By comparing this force with the calculated mean prestressing force in the middle section, some similarities were found. The magnitude is larger at the active prestressing edge than in the middle, and when releasing the jack, the load cell force resets to zero, while the force measured from strain sets back from wedge penetration. In this case the total prestressing force can be calculated.

$$P = (P_0 - \Delta P)n = (195\text{ kN} - 28\text{ kN}) \cdot 3 = 501\text{ kN} \tag{5.1}$$

Figure 5.6 really shows the reliability of the calculated prestressing force from the strain. The prestressing force variation in the middle section is captured accurately when comparing to the force from the load cell.

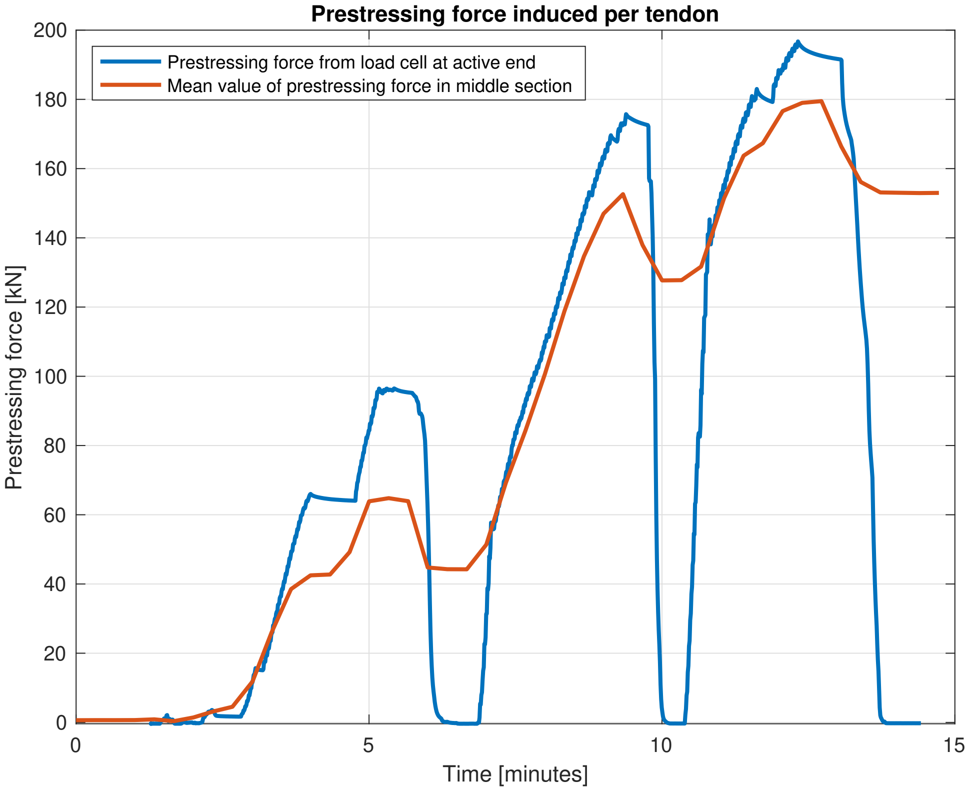

Figure 5.6: Force induced during post-tensioning.

The relation between the prestressing force at middle section compared to the active end induces that a reduction of prestressing force is present in the specimen, just as in theory. In Figure 5.7, the total force variation along the beam is visualized, both before and after the release of the jack. This is a result of friction losses where the duct curves. In the passive end, where the duct curves, the prestressing force is assumed to have the same decrease of force as in the active end, due to the symmetry of the duct profile.

It can also be seen that the wedge penetration affects the prestressing force, causing a decrease of force from the active end to the passive end of the specimen. By plotting the prestressing force in the middle section before and after the final release, using data from Figure 5.6, the difference in prestressing force can be visualized in the middle section. What is interesting from this graph is that the intersection of the two curves occur just before the end of the examined span. This indicates that the distance where wedge penetration affects the prestressing force, x_s, is almost as long as the examined span. The prestressing force after the intersection is unaffected by the wedge penetration, meaning that it follows the same force as before release.

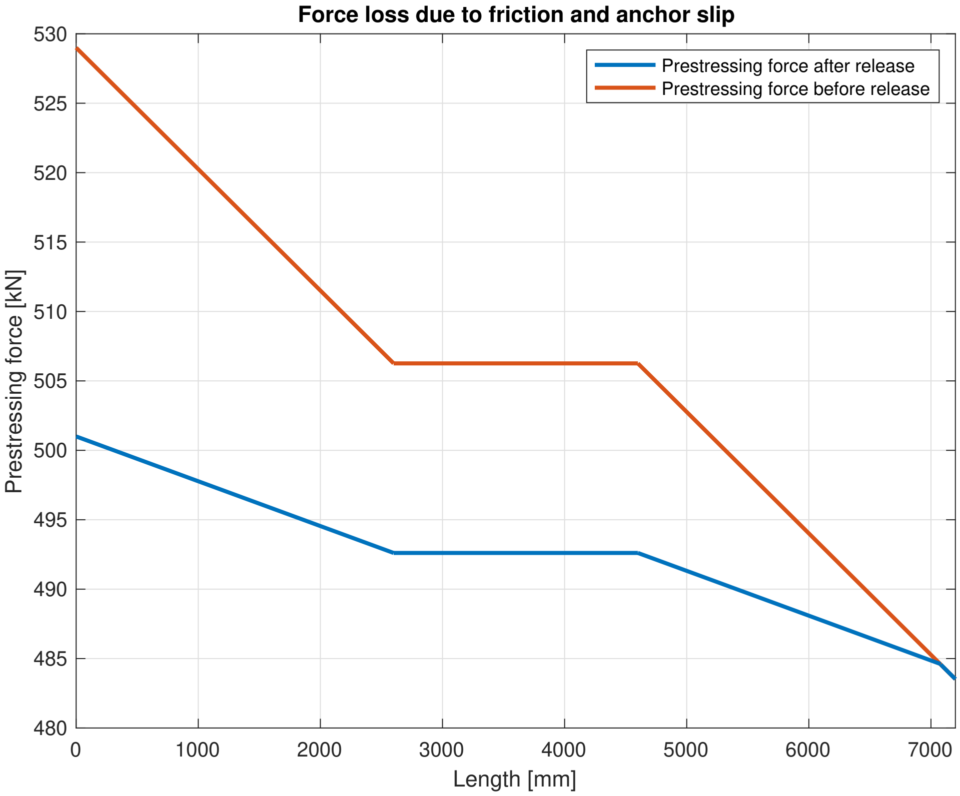

Figure 5.7: Force loss due to friction and wedge penetration.

5.2 Long-term results

By keeping the specimens in a controlled indoor environment over time, it was possible to measure long-term effects of the two specimens. In Figure 5.8, the measured strain variation over time can be seen. The dark blue colour symbolizes the time between start and stop of the post-tensioning. Obviously, this was only the case for the PRC specimen. For both specimens, it can be interpreted that the absolute value of the negative strain is constantly increasing, which is an effect of shortening of the specimen mainly due to shrinkage. Notice that the strain distribution in the top fiber of the PRC specimen changes from positive to negative strain.

For the PRC specimen, there is a rapid increase of compression during the first days, to later have a slight decrease of contraction. For the reference specimen, the contraction is more or less constant through the time span. Looking at the change of shape, the PRC specimen has an unchanged shape, while the reference specimen curves in the top and bottom edge. The top edge will experience the largest compressive strains, as the beam is simply supported. In contrary, the bottom edge will experience the smallest compressive forces. This indicates that the long-term effects cause an increasing deflection over time.

An interesting phenomena occurs at the compressive edge of both specimens, i.e. in the bottom fiber of the PRC and top fiber of the reference. At the length of 5500 mm there is a decrease of compressive strain, which is probably a result of the splice length of the reinforcement. An increase of steel gives a higher stiffness which counteracts the compressive strain at these locations.

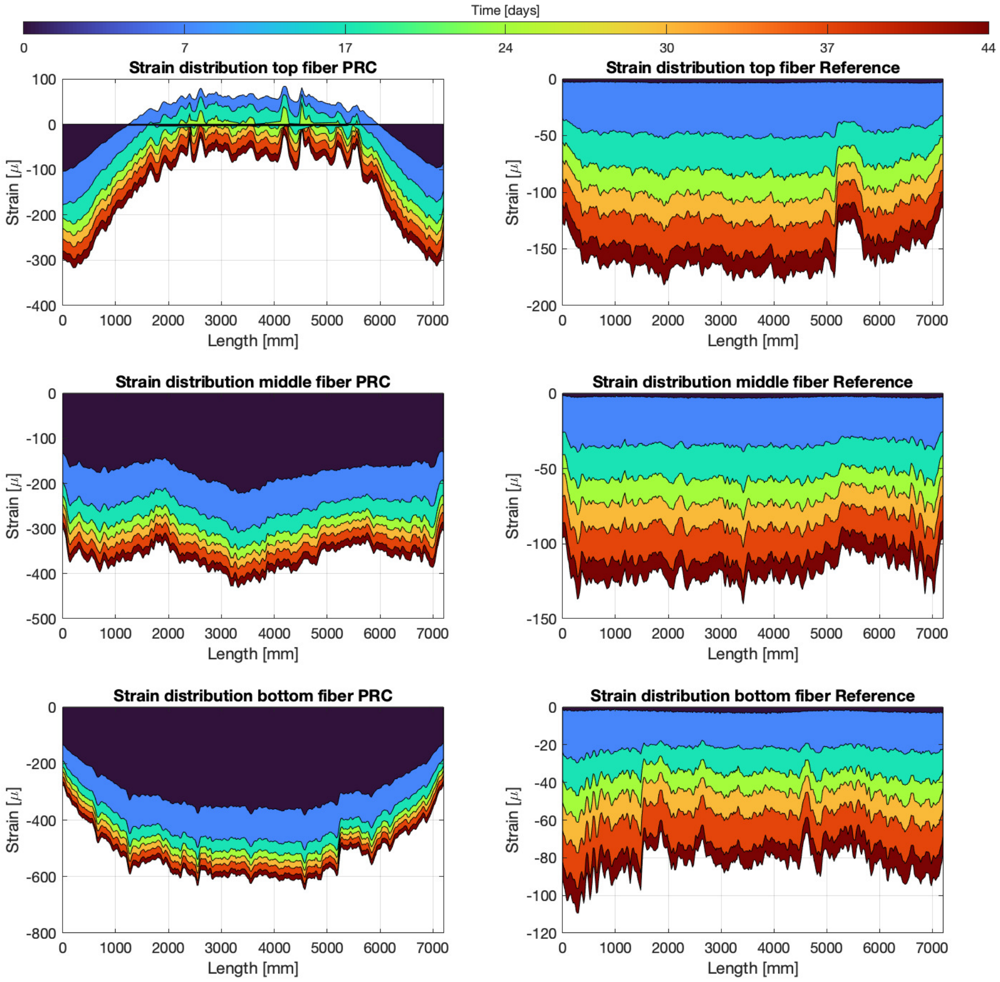

Figure 5.8: Strain variation for PRC and reference specimen. Darker region indicates the effect from post-tensioning.

As described previously, the deflection increases for the reference specimen, according to Figure 5.9. Looking at the PRC specimen, the curvature, rotation, and deflection continues to increase due to long-term effects.

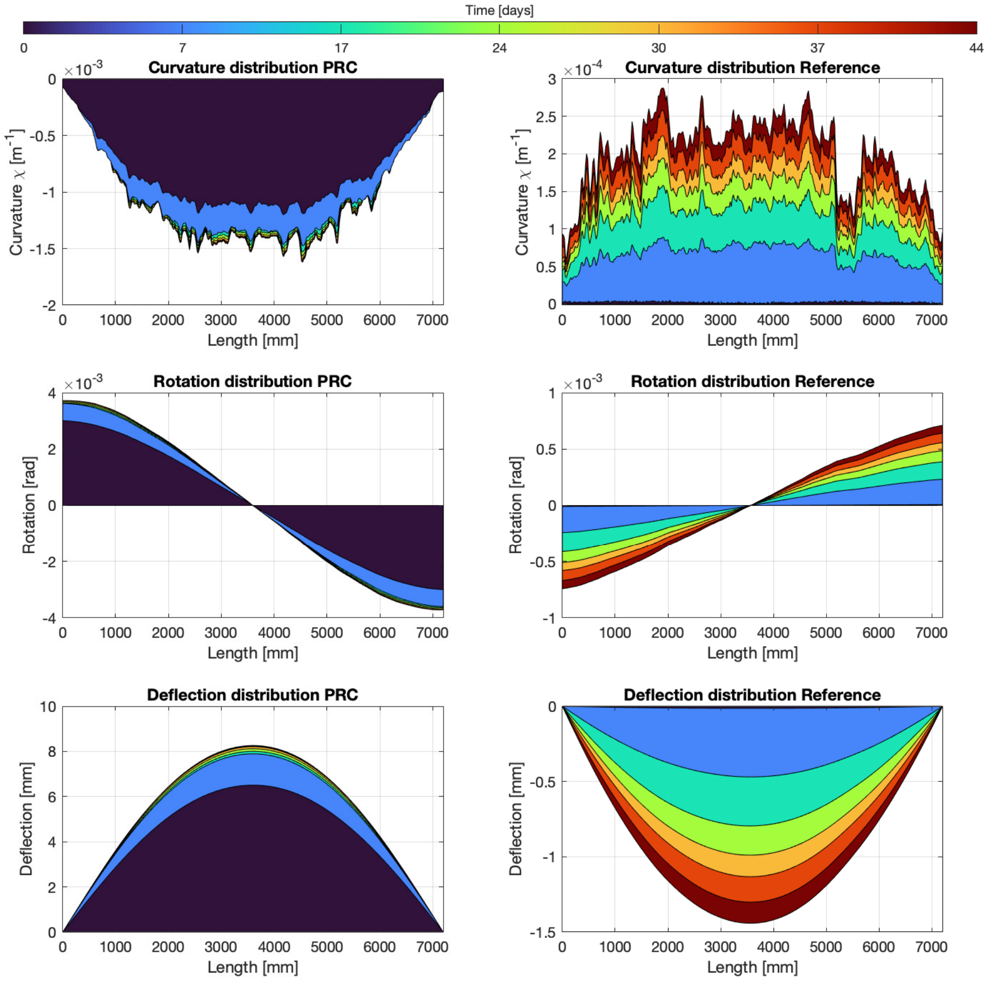

Figure 5.9: Curvature, rotation and deflection after long-term effects. Darker region indicates the effect from post-tensioning.

By tracing the strain development over time at the level of the prestressing steel in both specimens, in this case in the middle section, the effect of creep induced by the prestressing force can be approximated. By subtracting the measured strain from the RC specimen with the PRC the effects of shrinkage and creep from self-weight is removed and the strain from creep induced by the prestressing force can be calculated.

By multiplying the relative strain with the stiffness and the area of the prestressing steel, the force loss can be visualized, Figure 5.10. The prestressing induced creep contributes to about 60 % of the total force loss, which is near 13 kN over this time span of 45 days. Worth mention that in the total force loss, the effect from relaxation of the prestressing steel is included since this part is considered as a small and hard to isolate from the total loss. This effect will nevertheless be evaluated with theoretical calculation methods in Chapter. 5.5.

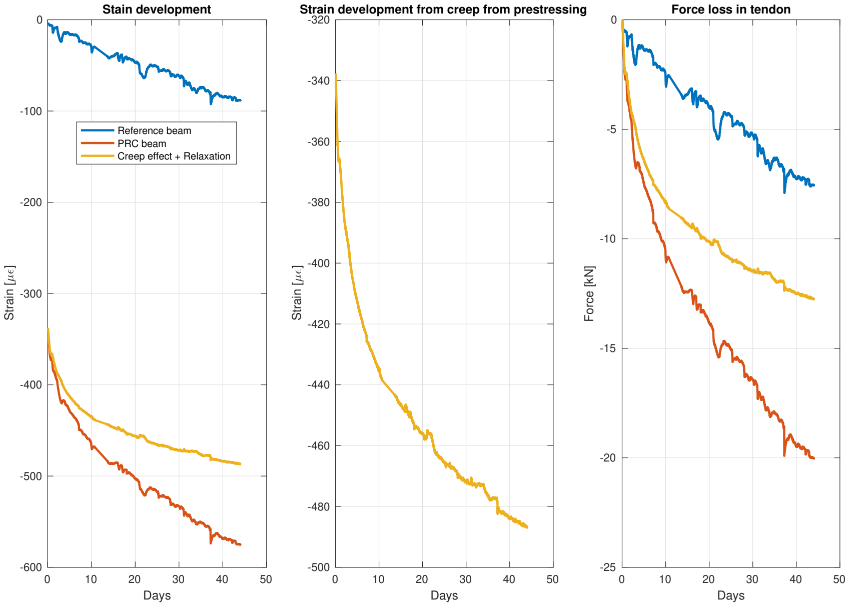

Figure 5.10: Strain and force development over time in middle section.

Earlier research performed to evaluate the loss of prestressing force on real structures over long time has found out that the major part of the time dependent losses, effecting the prestressing force, occurs within the first 6 month of the structure [13]. This research validates the behaviour seen in Figure 5.10 where it can be seen that the slope of the curve declines over time, although the shorter time period. Assuming an even force loss along the length of the beam, the total force loss during the long-term test could be calculated and is found in Figure 5.11.

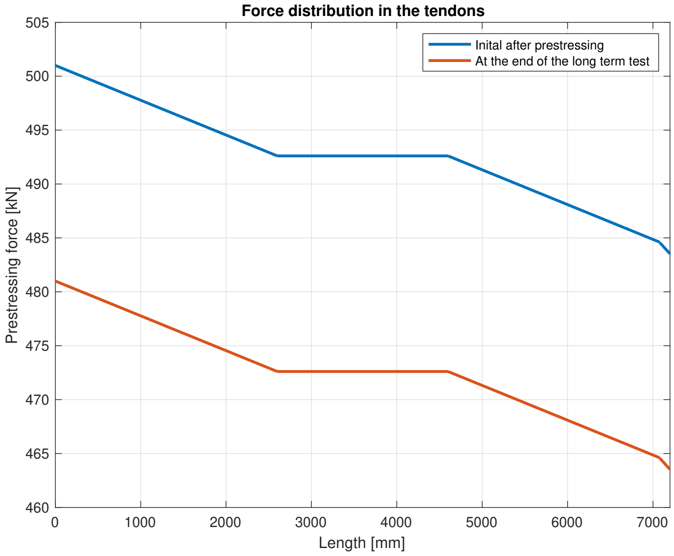

Figure 5.11: Tendon force distribution.

5.3 Pre-cracking and DIC comparison

During the pre-cracking stage of the PRC beam the load and deflection were captured using both data from the load cells on the actuators and the DOFS. The deflection was calculated from the strain data according to Equation 4.3, Chapter 4.2.1. In Figure 5.12 it is possible to follow the maximum deflection of the beam which follows the load ramping described in Chapter 4.3.2. The force in the figure is the applied force per point load measured from the load cell assuming an even distribution force through the load beam to the points. Worth notice is that the mid span deflection starts at a value of approximately 8mm. The explanation behind the positive deflection of the beam in the beginning of this loading stage is the reference point was set before the post-tensioning was performed, described in Chapter 5.2. It is possible to see from the graphs that cracks probably occurs in the beam during this stage since the slope of the curve changes in the loading cycle up to 60 kN. The nonlinear behaviour in this loading stage is explained by the change of stiffness in the beam as a result of the cracks. In the end of the test, the initial positive deflection decreases a bit due to the small cracks that has occurred in the bottom of the beam, but the final change of deflection is small in this test due to the low load magnitude.

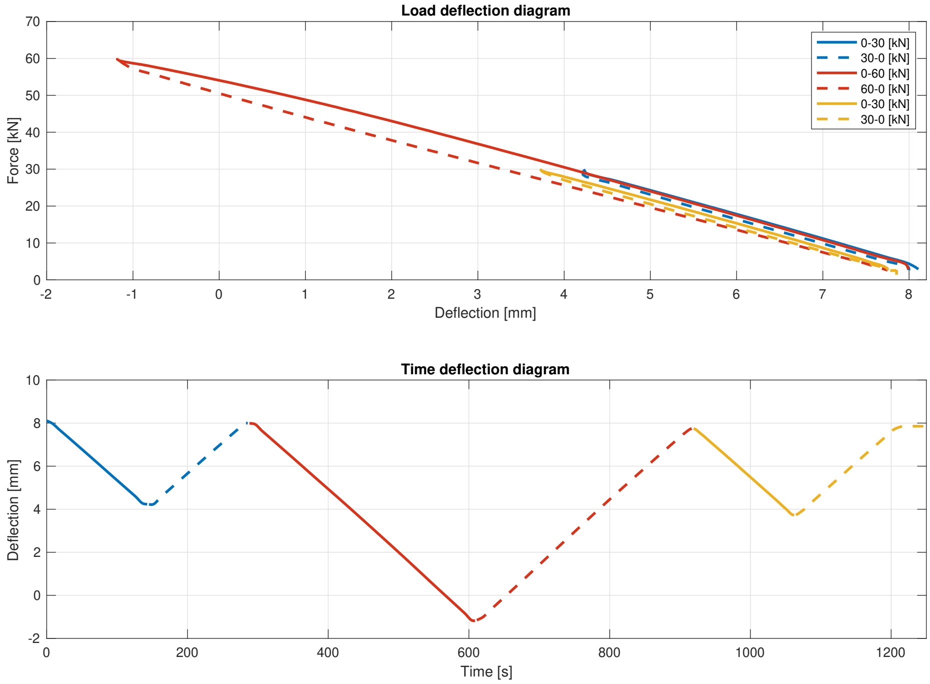

Figure 5.12: Load deflection diagram pre-cracking.

Since the strain was recorded during the test it was possible to correlate the obtained strain to a certain load level. This is visualized in Figure 5.13 where it is possible to both obtain the increase of strain with increasing load and also some strain peaks along the length of the beam. Since cracks will be initiated from the bottom of the beam, the DOFS of interest for cracks are the fibers connected to the bottom reinforcement. The variation between both sides of the beam were small and since the DIC was placed on the left side, the strain data for this comparison was retrieved from the bottom left fiber.

The two most distinct peaks at position 2750 mm and 4750 mm aligns with both the position for the point loads and with the change of slope for the duct. It is assumed that the load position has the heaviest influences on the local strain. This might be explained by the fact that the load leads to an angle change of the beam resulting in a strain increase. The difference in strain between the two maximum points could be explained by an uneven distribution of the applied force between the two loading points. Irregularities and differences in the stiffness along the length of the beam, for example at positions of reinforcement splicing, could result in uneven force distribution and thereby a strain increase.

In general, the peaks in the strain data are assumed to be possible cracks due to the local strain increase over a small region and further verification for this theory will be made through this chapter.

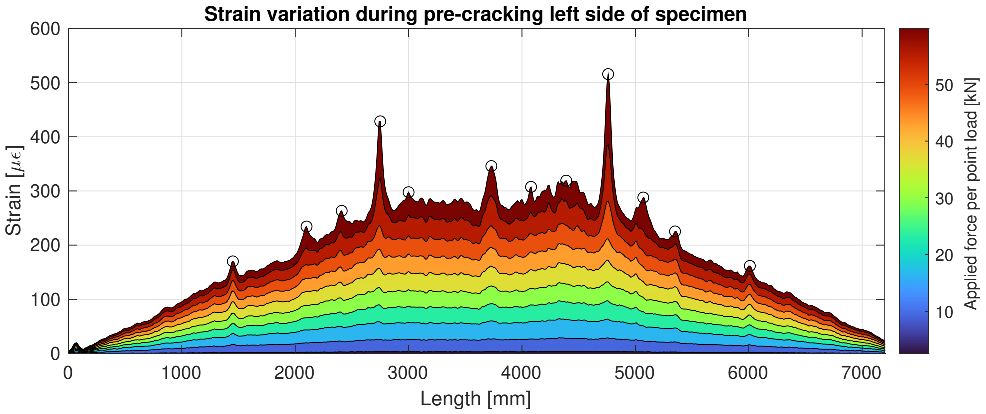

Figure 5.13: Strain variation during loading.

One verification step was to calculate the strain limit for crack development according to Equation 5.2 where the manufacturer material properties was used as input. As seen in the equation, the limit is 138 $\mu\varepsilon$ and some of the strain peaks could thereby be correlated to cracks in the concrete since the measured strain is above the crack limit. Worth mentioning is that f_{ctm} is the mean value of the concrete tensile strength and thereby one should be careful to draw the conclusion that measured strain above the limit automatically corresponds to a crack. Also as previously mentioned it should be noted that the measured strain in the figures do not precisely corresponds to the actual strain.

$$\varepsilon_{crack,lim} = \frac{f_{ctm}}{E_c} = \frac{4.5 \text{ MPa}}{32.2 \text{ GPa}} = 137.5\mu\varepsilon \tag{5.2}$$

As mentioned earlier in this chapter, the DOFS strain data from the final destructive four-point bending test went missing so instead the DOFS data from the pre-cracking test was compared with the DIC data from the final four-point test. Figure 5.14 shows the strain profile from the bottom left DOFS for different load levels and it is compared to a computed picture from the DIC at a load level of 60 kN. As seen in the figure, the highest strain peaks are outside the range of the DIC picture.

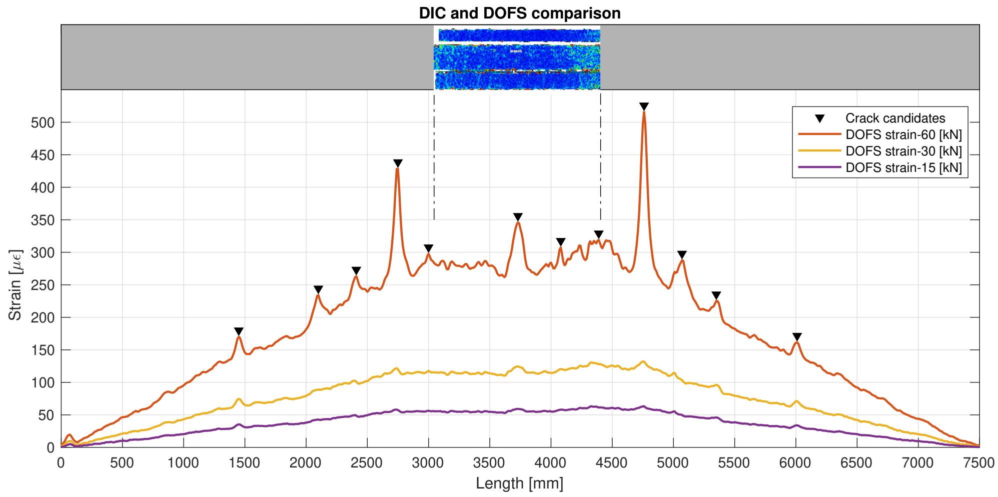

Figure 5.14: DIC picture and DOFS strain at 60 kN load.

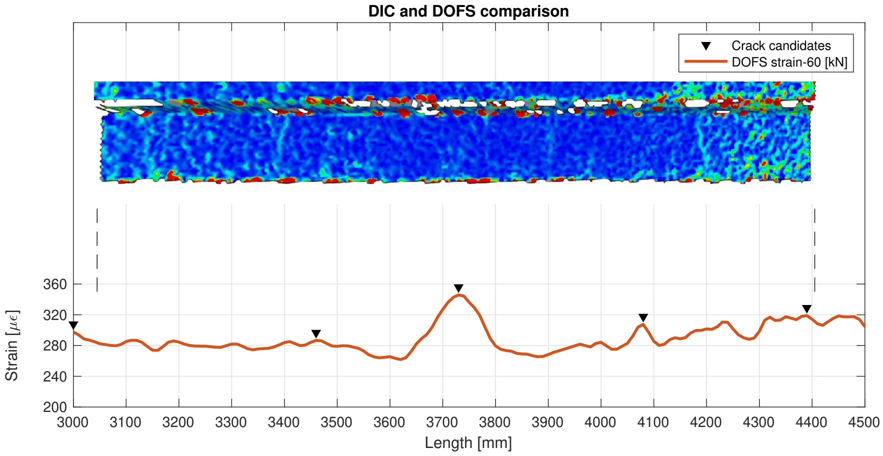

(a) Close-up of DIC picture and DOFS strain at 60 kN load.

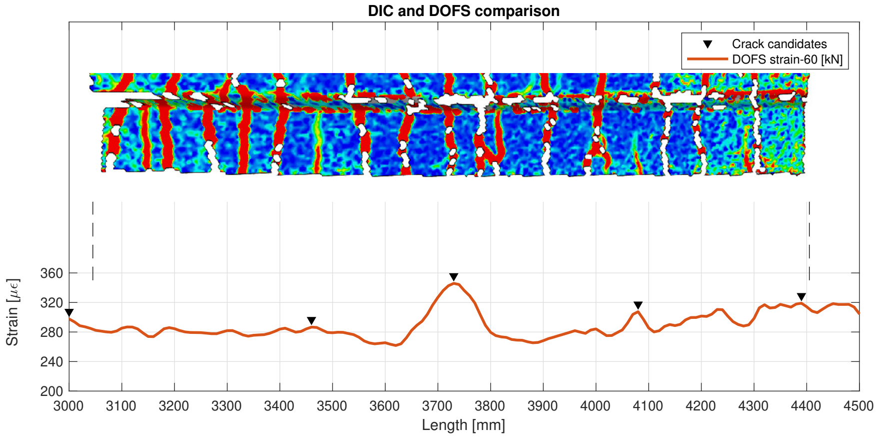

(b) Close-up of DIC picture at 190 kN load and DOFS strain at 60 kN load.

Figure 5.15: Crack determination from DIC picture and DOFS strain.

Figure 5.15a shows a close-up picture of Figure 5.14. In the DIC picture no clear cracks could be detected but according to the strain profile, some clear peaks that could be crack candidates can be seen. According to [5], where extensive studies in the field of DOFS has been made, it can be seen that for an ordinary RC beam the strain peaks obtained at lower strain levels can give a good approximation of the position of where the cracks will develop. Worth noting is that small cracks can merge into bigger cracks and some cracks might close when other cracks develop so therefore there are still uncertainties during determination of the exact positions for lower strain. In Figure 5.15b, strain data from 60 kN load is compared with a DIC picture from 190 kN load. At 190 kN load the beam have extensive cracking and therefore it is hard to determine the accuracy of the crack position from the DOFS at a lower load magnitude. Though, further experiments should be performed to validate the crack development from initiation of cracks until failure of the specimen.

5.4 Four-point bending test

In the four-point bending test, output from the actuator, load cell and DIC will be used to present results.

Firstly, comparing the point load force from the load cell to the displacement from the DIC, a load deflection diagram can be plotted, see Figure 5.16. One thing that massively separates the PRC specimen to the reference specimen is the ultimate load. In theory, according to Chapter 2.5.4, the ultimate capacity for two similar beams, one prestressed and one not, should be the same. The explanation to this is the extra capacity that is present in the PRC specimen. If the reference beam would have been constructed with three 15.7 mm tendons, just as the PRC specimen, the capacity in theory would been the same. It is no wonder that the reference specimen has a lower ultimate capacity, due to the extra steel and lever arm constructed in the PRC specimen.

This though, does not affect the first bending crack initiated in the two specimens. As seen, the first bending crack for the reference specimen occur earlier than for the PRC specimen, mainly due to the axial force induced from prestressing. The crack initiation also causes the deflection to increase. The deflection is almost 40 mm larger at 70 kN for the reference beam, partly because of the early cracks, partly because the inverted effect on the deflection that the prestressing cause.

In Figure 5.17 the result from the final test can be seen, where crushing of concrete was decisive for the PRC beam and bending cracks/ deformation was decisive for the RC beam.

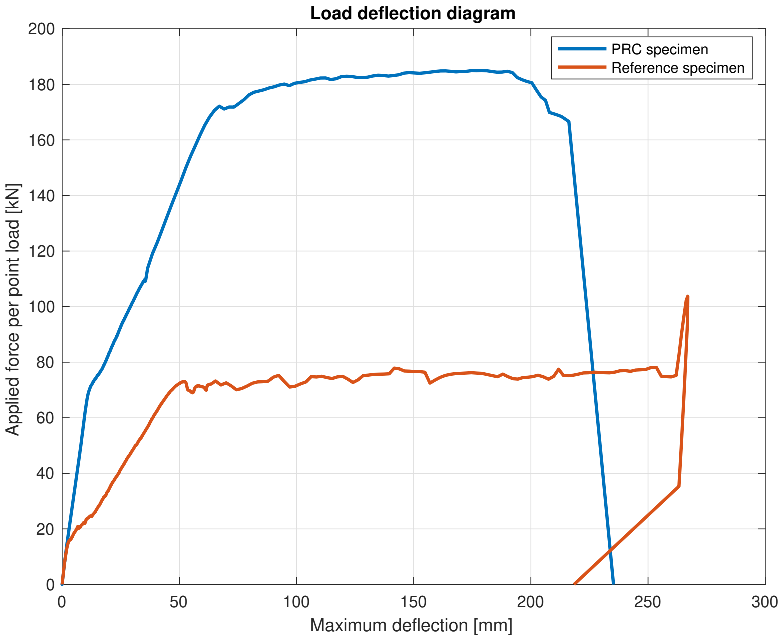

Figure 5.16: Load displacement diagram.

(a) Failure of PRC specimen.

(b) Failure of RC specimen.

Figure 5.17: Destructive four-point bending test.

It is also of interest that the ultimate bending moment created by the point loads is larger than anticipated in Appendix A. This might be a result of the calculation method used for the bending moment capacity. Yielding of the prestressing steel was used as the limit for bending capacity, according to [1], where in reality the passive reinforcement will continue to contribute to strength. Also, the prestressing steel was assumed to have a horizontal top branch during yielding. In Eurocode, the stress-strain relationship can also be described with an inclined top branch that captures the effects of hardening, which further increase the ultimate bending moment.

By analysing data from the DIC images, crack widths from four selected cracks can be displayed as a function of the applied load, see Figure 5.18. The position of these four cracks was located between the two point loads. It can be interpreted that the pre-cracking caused cracks to a point load of approximately 70 kN. After this load, a change of behaviour can be seen, causing a change of slope in the graph. This continues beyond the 0.2 mm crack width limit, up to yielding of the specimen. At this stage the cracks grow larger due to yielding of the reinforcement until failure.

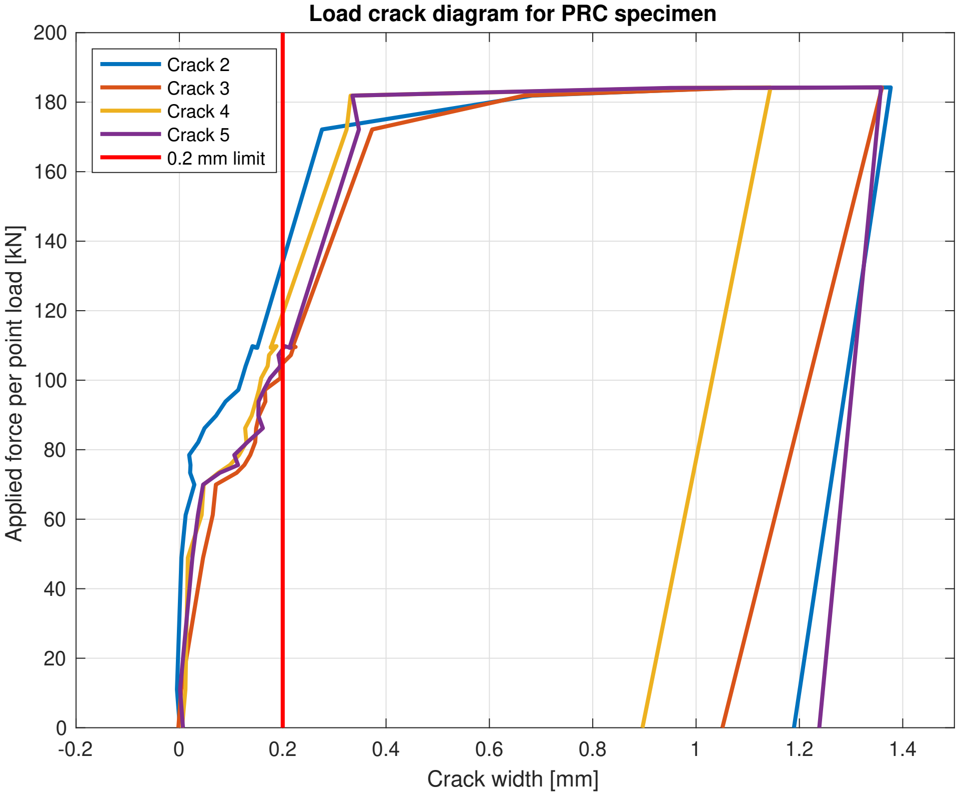

Figure 5.18: Load crack diagram.

A comparison was made between maximum deflections from the DIC and calculated deflections using DOFS, see Table 5.1. Prestressing contributes to a reduction of deflection, very least when comparing to the reference specimen. The deflection of the reference specimen at zero state is the same as the PRC specimen at 60 kN/point load. As deflection is a vital part of the design in SLS, it is remarkable what influence the prestressing have on deflection.

Table 5.1: Comparison of deflection.

Specimen	Reference			PRC		
	DOFS [mm]	DIC [mm]	Rel. error	DOFS [mm]	DIC [mm]	Rel. error
0 kN/point load	-1.4	-1.4	0 %	8.1	8.1	0 %
30 kN/point load	-18.2	-18.3	0.5 %	4.5	4.6	2.9 %
60 kN/point load	-38.7	-40.0	3.3 %	-1.2	-1.4	2.1 %

5.5 Comparison with theoretical calculation methods

Some of the obtained results were compared with theoretical calculation methods used in Eurocode. By making this comparison, calculations methods can be verified to the results from this experiment.

Comparing the strain and force, originally from Figure 5.5, with the calculated creep strain and steel relaxation from Eurocode, a similar behaviour is captured, see Figure 5.19. Since creep is load dependent, Equation 5.3 could be used to calculate the strain originating from load induced creep effect. Assuming a relaxation loss of 2.5 % after 1000 hours for the prestressing steel the relaxation factor could be calculated according to Equation 2.15.

$$\varepsilon_{c,creep}(t) = \varphi(t,t_0)\frac{\sigma_c}{E_c} = \varphi(t,t_0)\frac{P}{E_c A_c} \tag{5.3}$$

As seen, the result from the DOFS has the same shape as the result from Eurocode calculations. As expected, the creep effect is significantly larger than the relaxation. By adding the effects from creep and relaxation, a total creep and relaxation effect based on Eurocode is displayed. Comparing to the effects from the DOFS, the two graphs are almost identical, based on the results from this specimen. The relative error is 0.8 %. This is remarkable, and an indication that DOFS gives reliable results and that Eurocode estimates creep and relaxation accurately.

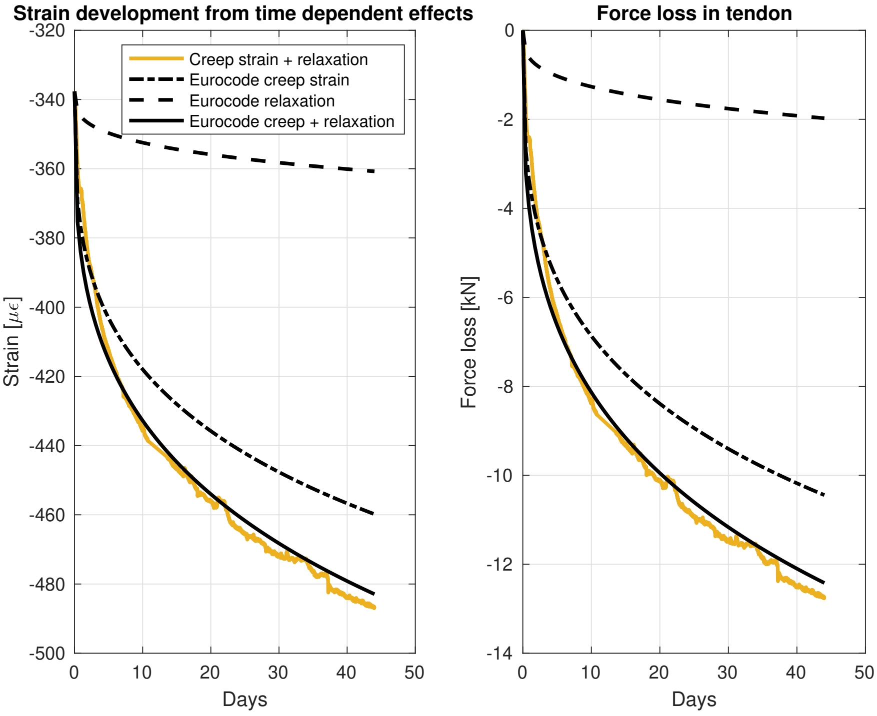

Figure 5.19: Comparison between prestressing force induced creep and relaxation to model in Eurocode according to Equation 2.14-2.16 and 5.3.

When comparing the prestressing force distribution after the final release during post-tensioning to the prestressing force calculated in Eurocode, it can be seen that the force is similar. Again, the loss was overestimated in the theoretical calculation method by approximately 0.6 % in the end span. The wedge penetration was calculated to affect the whole length of the specimen in Eurocode, in contrary to the prestressing force from DOFS where the wedge penetration almost effects the whole specimen length. Though, this difference is marginal as the calculated effective distance where wedge penetration occur was calculated to 7.44 m in Eurocode, which is slightly longer than the span of interest. Note that the prestressing force is assumed constant from the end values to the outer edges of the beam.

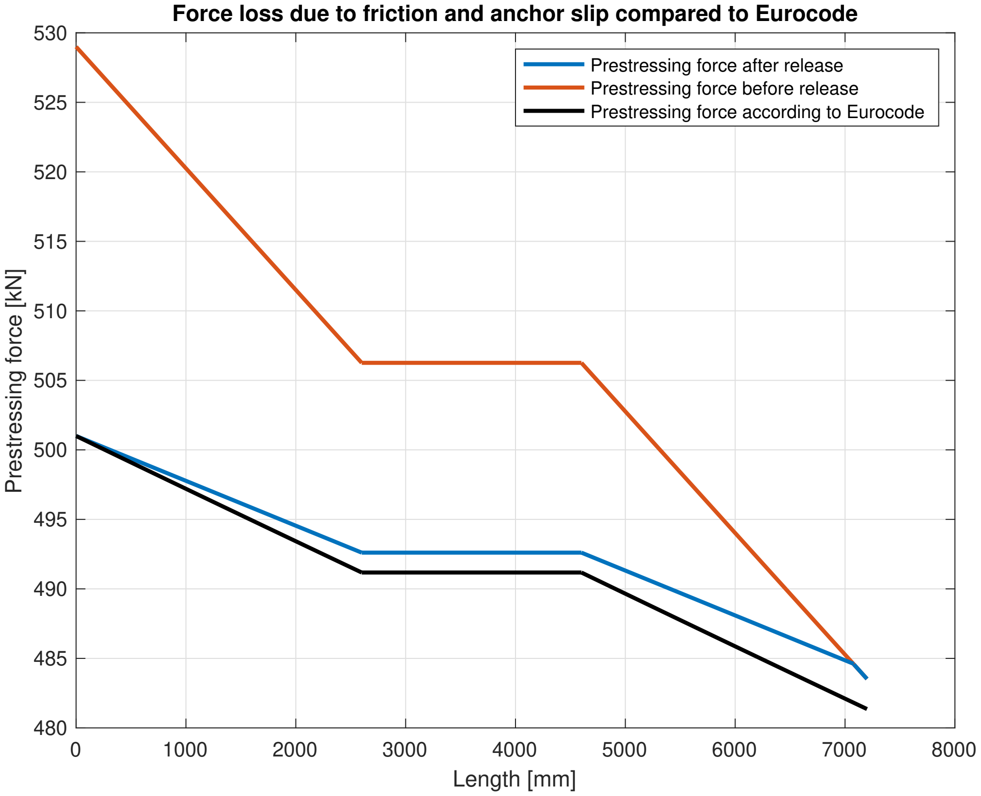

Figure 5.20: Force loss due to friction and wedge penetration compared to Eurocode.

Comparing the measured crack widths to Eurocode, it can be seen in Appendix A that the calculated crack width in SLS, for 52.5 kN, is 0.014 mm. By comparing this value to the four different crack widths from DIC, it can be seen in Figure 5.21 that the real crack widths are larger in three out of four cases. For one crack, the width is about 3.5 times wider than in Eurocode, which is a significant difference.

Though the difference in crack width still is not close to the crack limit in SLS, 0.2 mm, it is still an underestimation in Eurocode of the actual crack width. Worth noting is that the crack widths have been refined due to large scatter during measuring. After all, the crack widths are so small that even the smallest disturbance affect the measured width and might affect the actual crack width when measuring with DIC.

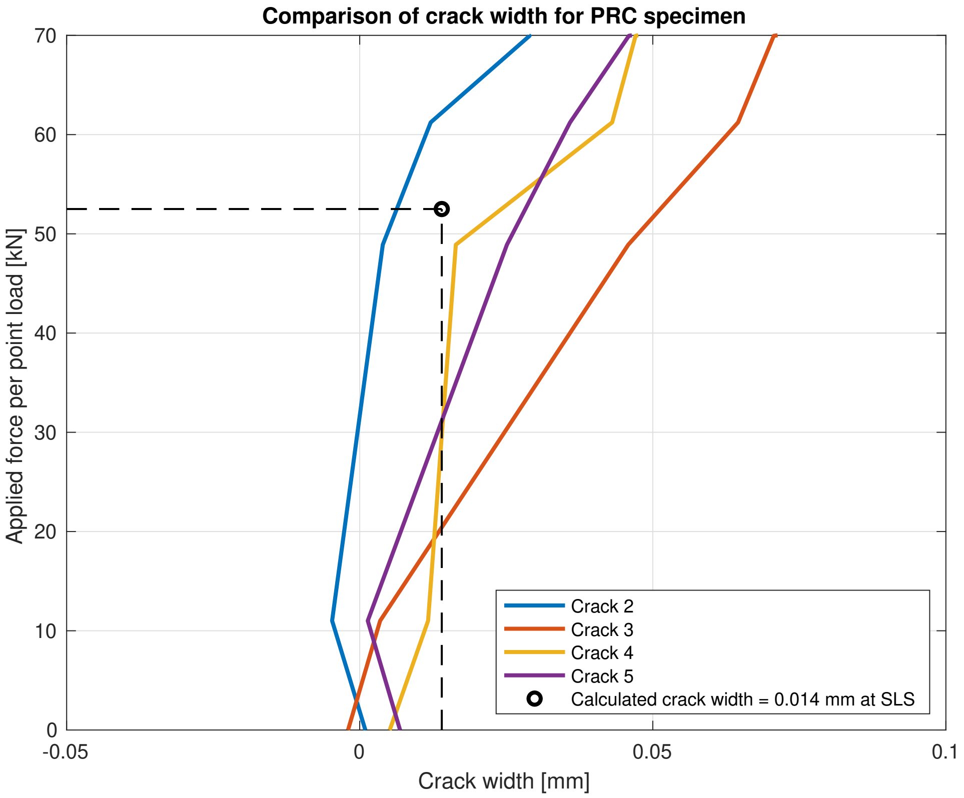

Figure 5.21: Comparison of crack width for PRC specimen.

6

Conclusion

In conclusion, this thesis presented the usage of DOFS, distributed optic fiber sensors, for further possibilities of measuring behaviour and key performance indicators for a post-tensioned reinforced concrete specimen. By using an additional reference beam, the effects of prestressing could be determined accurately by removing effects related to solely concrete, as shrinkage and creep induced by self-weight.

Regarding the strain from the DOFS, the quality of output was successful despite operating in a previously untested area. Previous research has solely tested the usage of DOFS for reinforced concrete specimens. This thesis finds the usage of DOFS feasible with post-tensioned reinforced concrete members. As post-tensioned concrete shows many similarities with pre-tensioned concrete, it is probable that usage of DOFS will be practicable with this type of prestressing as well.

By comparing results from DOFS to theoretical calculation methods, some conclusions were made. Starting with the loss of prestressing force, shrinkage and creep from self-weight was removed and only mechanical creep and relaxation was considered. It was seen that the shape of the graph reminded of an ordinary creep curve, and the result was verified by comparing to theoretical creep and relaxation calculations. The theoretical results were almost identical to the results from DOFS, which verifies the reliability.

Moving on to force loss along the specimen due to wedge penetration and friction, the results were similar. By comparing loss of prestressing force in the active end and middle section, a relation between loss of prestressing force over the specimen was plotted. It was seen that the wedge penetration almost affected the whole length of the specimen, whereas the theoretical calculation claimed the same length was slightly longer than the length of interest.

Looking at crack widths, it was seen that the theoretical result underestimated the crack widths from the DIC. Though, due to small widths and the matter of fact that the specimen was in motion due to loading, scatter occurred which disputes the reliability of these results.

Furthermore, it was also found that usage of DOFS could detect crack candidates at an early stage during testing. As described in Chapter 5.3, already at relatively small loads a change of strain was detected, that is indicating future cracks. This assumption was built upon earlier studies and to verify this, further research with higher strain should be performed.

As sustainability is a subject on the agenda, it is unfortunate that the use of post-tensioned concrete has declined over the last decades. This thesis states that key performance indicators in a post-tensioned member are described well by modern theoretical approaches. By applying monitoring system such as DOFS the prestressing force can now be accurately controlled in real time and the uncertainties previously connected to this area are no longer apparent. The impression is that distributed optical fiber sensors can increase knowledge of civil infrastructure and promote continuous and enhanced usage of post-tensioned concrete. Increased research and usage of DOFS in civil infrastructure can be a key for a more sustainable and efficient construction industry for future generations.

6.1 Further research

Further experiments need to be conducted to validate the usage of DOFS in PRC structures and thereby the results of this thesis. Firstly, measurements should be evaluated over longer time to capture and imitate the life span of a post-tensioned concrete structure. Secondly, distributed optic fiber sensors should be installed and evaluated in other types of structures, as pre-tensioned concrete, slabs, and walls. Furthermore, research of the measured data from the cyclic loading test should be made to analyse a more realistic loading scenario.

Lastly, corrosion is one major concern regarding the functionality of prestressing tendons. The same approach used in this study should be tested against corrosion. Due to the high resolution and accuracy using DOFS, the results indicates that this technique has potential to detect and monitor corrosion development of tendons as well.

Bibliography

[1] B. Engström, *Design and analysis of prestressed concrete structures.* Chalmers University of Technology, Department of Civil and Environmental Engineering, Structural Engineering, Concrete Structures, Report 2011:7, Gothenburg, 2011.

[2] H. R. Dolan, Charles W. Hamilton, *Prestressed Concrete : Building, Design, and Construction.* Cham, Switzerland: Springer International Publishing, 2019. [Online]. Available: https://link.springer.com/book/10.1007/978-3-319-97882-6, Accessed on: 2022-03-01.

[3] B. S. Choo, "25 - reinforced and prestressed concrete," in *Advanced Concrete Technology* (J. Newman and B. S. Choo, eds.), pp. 3–17, Oxford: Butterworth-Heinemann, 2003.

[4] Trafikverket, "Batman - Bro och Tunnel Management," n.d.

[5] C. G. Berrocal, I. Fernandez, M. F. Bado, J. R. Casas, and R. Rempling, "Assessment and visualization of performance indicators of reinforced concrete beams by distributed optical fibre sensing," *Structural Health Monitoring*, vol. 20, pp. 3309–3326, Jan. 2021. https://doi.org/10.1177%2F1475921720984431.

[6] M. Al-Emrani, B. Engström, M. Johansson, and P. Johansson, *Bärande konstruktioner : Del 1.* Chalmers University of Technology, Department of Civil and Environmental Engineering, Structural Engineering, Concrete Structures, Report 2013:1, Gothenburg, 2013.

[7] European Committee for Standardisation, *European Standard, EN 1992-1-1. Eurocode 2: Design of concrete structures.- Part 1-1: General rules and rules for buildings.* Brussel, Dec 2004.

[8] B. Glišić, D. Hubbell, D. H. Sigurdardottir, and Y. Yao, "Damage detection and characterization using long-gauge and distributed fiber optic sensors," *Optical Engineering*, vol. 52, no. 8, 2013. doi:10.1117/1.OE.52.8.087101.

[9] C. G. Berrocal, I. Fernandez, and R. Rempling, "Crack monitoring in reinforced concrete beams by distributed optical fiber sensors," *Structure and Infrastructure Engineering*, vol. 17, no. 1, pp. 124–139, 2021. https://doi.org/10.1080/15732479.2020.1731558.

[10] P. Lu, N. Lalam, M. Badar, B. Liu, B. T. Chorpening, M. P. Buric, and P. R. Ohodnicki, “Distributed optical fiber sensing: Review and perspective,” *Applied Physics Reviews*, vol. 6, no. 4, 2019. https://doi.org/10.1063/1.5113955.

[11] CCL Spännarmering, “Post-tensioning systems,” 2017.

[12] European Committee for Standardisation, *European Standard, EN 12390-3. Testing hardened concrete – Part 3: Compressive strength of test specimens.* Brussel, June 2019.

[13] H. Abdel-Jaber and B. Glisic, “Monitoring of long-term prestress losses in prestressed concrete structures using fiber optic sensors,” *Structural Health Monitoring*, vol. 18, no. 1, pp. 254–269, 2019. https://doi.org/10.1177/1475921717751870.

A

Design calculations

Master Thesis - Design of Specimen

INPUT

Geometry:

$l_1 := 3\text{m}$

$l_2 := 2\text{m}$

$l_3 := l_1 = 3\,\text{m}$

$l := l_1 + l_2 + l_3 = 8\,\text{m} \qquad l_{eff} := 7.5\text{m}$

$b_{tf} := 380\text{mm}$ top flange

$h_{tf} := 100\text{mm}$

$b_w := 150\text{mm}$ web

$h_w := 250\text{mm}$

$b_{bf} := 280\text{mm}$ bottom flange

$h_{bf} := 125\text{mm}$

$b_{bt} := \dfrac{b_{bf} - b_w}{2} = 0.065\,\text{m}$ bottom "triangles"

$h_{bt} := 2.5\text{cm}$

$b_{tt} := \dfrac{b_{tf} - b_w}{2} = 0.115\,\text{m}$ top "triangles"

$h_{tt} := 2.5\text{cm}$

$h := h_{tf} + h_w + h_{bf} = 0.475\,\text{m} \qquad h_{max} := 0.5\text{m}$

Concrete (28 days):

$\gamma_c := 1$

$f_{cm} := 65.6\text{MPa}$

$f_{ck} := f_{cm} - 8\text{MPa} = 57.6\cdot\text{MPa}$

$f_{cd} := \dfrac{f_{ck}}{\gamma_c} = 57.6\cdot\text{MPa}$

$f_{ctm} := 0.3\cdot\left(\dfrac{f_{ck}}{\text{MPa}}\right)^{\frac{2}{3}}\text{MPa} = 4.474\cdot\text{MPa}$

$f_{ctk0.05} := 0.7\cdot f_{ctm} = 3.132\cdot\text{MPa}$

$f_{ctk.0.95} := 1.3\cdot f_{ctm} = 5.817\cdot\text{MPa}$

$f_{ctd} := \dfrac{f_{ctk0.05}}{\gamma_c}$

$E_{cm} := 22\cdot\left(\dfrac{f_{cm}}{10\text{MPa}}\right)^{0.3}\text{GPa} = 38.681\cdot\text{GPa}$

$\sigma_{cc.inf.max} := 0.6\cdot f_{ck} = 34.56\cdot\text{MPa}$

$\sigma_{cti.max} := f_{ctk.0.95} = 5.817\cdot\text{MPa}$

$\sigma_{cci.max} := 0.45\cdot f_{ck} = 25.92\cdot\text{MPa}$

$\sigma_{ct.inf.max} := f_{ctk.0.95} = 5.817\cdot\text{MPa}$

Concrete (7 days):

$f_{cm7} := 0.86\cdot 65.6\text{MPa}$

$f_{ck7} := f_{cm7} - 8\text{MPa} = 48.416\cdot\text{MPa}$

$f_{cd7} := \dfrac{f_{ck7}}{\gamma_c} = 48.416\cdot\text{MPa}$

$f_{ctm7} := 0.3\cdot\left(\dfrac{f_{ck7}}{\text{MPa}}\right)^{\frac{2}{3}}\text{MPa} = 3.985\cdot\text{MPa}$

$f_{ctk0.05.7} := 0.7\cdot f_{ctm7} = 2.79\cdot\text{MPa}$

$f_{ctk.0.95.7} := 1.3\cdot f_{ctm7} = 5.181\cdot\text{MPa}$

$E_{cm7} := 22\cdot\left(\dfrac{f_{cm7}}{10\text{MPa}}\right)^{0.3}\text{GPa} = 36.969\cdot\text{GPa}$

$\sigma_{cti.max7} := f_{ctk0.05.7} = 2.79\cdot\text{MPa}$

$\sigma_{cci.max7} := 0.45\cdot f_{ck7} = 21.787\cdot\text{MPa}$

Reinforcement:

$\gamma_s := 1$

$f_{yk} := 500\text{MPa}$

$f_{yd} := \dfrac{f_{yk}}{\gamma_s}$

$E_s := 200\text{GPa}$

$\phi := 16\text{mm}$

$A_{si} := \left(\dfrac{\phi}{2}\right)^2 \cdot \pi$

$\phi_{stirrup} := 8\text{mm}$

$\alpha_s := \dfrac{E_s}{E_{cm}} = 5.171$

$n_s := 4 \qquad n_{s.prim} := 4$

$A_{s.tot} := \left(n_s + n_{s.prim}\right) \cdot A_{si} = 1.608 \times 10^{-3}\,\text{m}^2$

$A_{s1} := n_s \cdot A_{si} \qquad A_{s.prim} := n_{s.prim} \cdot A_{si}$

$d_{prim} := 36\text{mm} \qquad d_1 := h - 36\text{mm}$

Post-tensioned steel:

$\phi_{tendon} := 15.7\text{mm}$

$A_{pi} := 150\text{mm}^2$

$n_{tendon} := 3$

$A_p := A_{pi} \cdot n_{tendon}$

$E_p := 190\text{GPa}$

$f_{puk} := 1860\text{MPa}$

$f_{p0.1k} := \dfrac{246\text{kN}}{A_{pi}} = 1.64 \times 10^3 \cdot \text{MPa}$

$\alpha_p := \dfrac{E_p}{E_{cm}} = 4.912$

SECTIONAL CONSTANTS

Eccentricity of tendon and prestressing (iterative values)

$e_f := 198\text{mm}$ $P_{i.1} := 187\text{kN}\cdot n_{tendon} = 0.561\cdot\text{MN}$ Max load for one tendon 221 kN.

Areas and centroids

Top flange:	$A_{tf} := b_{tf}\cdot h_{tf} = 0.038\,\text{m}^2$	$y_{tf} := \frac{h_{tf}}{2} = 0.05\,\text{m}$
Top triangles:	$A_{tt} := \frac{b_{tt}\cdot h_{tt}}{2} = 1.438\times10^{-3}\,\text{m}^2$	$y_{tt} := h_{tf} + \frac{1}{3}\cdot h_{tt} = 0.108\,\text{m}$
Web:	$A_w := h_w\cdot b_w = 0.038\,\text{m}^2$	$y_w := h_{tf} + \frac{h_w}{2} = 0.225\,\text{m}$
Bottom triangles:	$A_{bt} := \frac{b_{bt}\cdot h_{bt}}{2} = 8.125\times10^{-4}\,\text{m}^2$	$y_{bt} := h_{tf} + h_w - \frac{1}{3}\cdot h_{bt} = 0.342\,\text{m}$
Bottom flange:	$A_{bf} := h_{bf}\cdot b_{bf} = 0.035\,\text{m}^2$	$y_{bf} := h_{tf} + h_w + \frac{h_{bf}}{2} = 0.413\,\text{m}$
Duct:	$A_{duct} := 1174\text{mm}^2$	$y_{duct.net} := 222\text{mm} + e_f$ $y_{duct.I} := 227\text{mm} + e_f$

$$A_c := A_{tf} + 2A_{tt} + A_w + 2A_{bt} + A_{bf} = 0.115\,\text{m}^2$$

$$A_{net} := A_{tf} + 2A_{tt} + A_w + 2A_{bt} + A_{bf} - A_{duct} + (\alpha_s - 1)\cdot A_{s.tot} = 0.121\,\text{m}^2$$

$$A_I := A_c + (\alpha_p - 1)\cdot A_p + (\alpha_s - 1)\cdot A_{s.tot} = 0.123\,\text{m}^2$$

$$x_c := \frac{A_{tf}\cdot y_{tf} + 2A_{tt}\cdot y_{tt} + A_w\cdot y_w + 2A_{bt}\cdot y_{bt} + A_{bf}\cdot y_{bf}}{A_c} = 0.223\,\text{m}$$

$$x_{net} := \frac{A_{tf}\cdot y_{tf} + 2A_{tt}\cdot y_{tt} + A_w\cdot y_w + 2A_{bt}\cdot y_{bt} + A_{bf}\cdot y_{bf} - A_{duct}\cdot y_{duct.net} \cdots + \left[(\alpha_s - 1)\cdot A_{s.prim}\cdot d_{prim} + (\alpha_s - 1)\cdot A_{s1}\cdot d_1\right]}{A_{net}} = 0.222\,\text{m}$$

$$x_I := \frac{A_{tf}\cdot y_{tf} + 2A_{tt}\cdot y_{tt} + A_w\cdot y_w + 2A_{bt}\cdot y_{bt} + A_{bf}\cdot y_{bf} + (\alpha_p - 1)\cdot A_p\cdot y_{duct.I} \cdots + (\alpha_s - 1)\cdot A_{s.prim}\cdot d_{prim} + (\alpha_s - 1)\cdot A_{s1}\cdot d_1}{A_I} = 0.227\,\text{m}$$

$$e_{f.max} := h - x_c - \left(20\text{mm} + 8\text{mm} + 16\text{mm} + 2\text{mm} + \frac{\phi_{tendon}}{2}\right) = 0.198\,\text{m}$$

$$e_{net} := h - x_{net} - \left(20\text{mm} + 8\text{mm} + 16\text{mm} + 2\text{mm} + \frac{\phi_{tendon}}{2}\right) = 0.199\,\text{m}$$

$$e_I := h - x_I - \left(20\text{mm} + 8\text{mm} + 16\text{mm} + 2\text{mm} + \frac{\phi_{tendon}}{2}\right) = 0.195\,\text{m}$$

Second moment of inertia

$$I_{tf} := \frac{b_{tf} \cdot h_{tf}^{3}}{12} + A_{tf} \cdot \left(x_c - y_{tf}\right)^2 \qquad I_{tf.net} := \frac{b_{tf} \cdot h_{tf}^{3}}{12} + A_{tf} \cdot \left(x_{net} - y_{tf}\right)^2$$

$$I_{tt} := \frac{b_{tt} \cdot h_{tt}^{3}}{36} + A_{tt} \cdot \left(x_c - y_{tt}\right)^2 \qquad I_{tt.net} := \frac{b_{tt} \cdot h_{tt}^{3}}{36} + A_{tt} \cdot \left(x_{net} - y_{tt}\right)^2$$

$$I_{w} := \frac{b_{w} \cdot h_{w}^{3}}{12} + A_{w} \cdot \left(x_c - y_{w}\right)^2 \qquad I_{w.net} := \frac{b_{w} \cdot h_{w}^{3}}{12} + A_{w} \cdot \left(x_{net} - y_{w}\right)^2$$

$$I_{bt} := \frac{b_{bt} \cdot h_{bt}^{3}}{36} + A_{bt} \cdot \left(x_c - y_{bt}\right)^2 \qquad I_{bt.net} := \frac{b_{bt} \cdot h_{bt}^{3}}{36} + A_{bt} \cdot \left(x_{net} - y_{bt}\right)^2$$

$$I_{bf} := \frac{b_{bf} \cdot h_{bf}^{3}}{12} + A_{bf} \cdot \left(x_c - y_{bf}\right)^2 \qquad I_{bf.net} := \frac{b_{bf} \cdot h_{bf}^{3}}{12} + A_{bf} \cdot \left(x_{net} - y_{bf}\right)^2$$

$$I_{tf.I} := \frac{b_{tf} \cdot h_{tf}^{3}}{12} + A_{tf} \cdot \left(x_I - y_{tf}\right)^2$$

$$I_{tt.I} := \frac{b_{tt} \cdot h_{tt}^{3}}{36} + A_{tt} \cdot \left(x_I - y_{tt}\right)^2$$

$$I_{w.I} := \frac{b_{w} \cdot h_{w}^{3}}{12} + A_{w} \cdot \left(x_I - y_{w}\right)^2$$

$$I_{bt.I} := \frac{b_{bt} \cdot h_{bt}^{3}}{36} + A_{bt} \cdot \left(x_I - y_{bt}\right)^2$$

$$I_{bf.I} := \frac{b_{bf} \cdot h_{bf}^{3}}{12} + A_{bf} \cdot \left(x_I - y_{bf}\right)^2$$

$$I_c := I_{tf} + 2I_{tt} + I_w + 2I_{bt} + I_{bf} = 2.728 \times 10^{-3}\,m^4$$

$$I_{net} := I_{tf.net} + 2I_{tt.net} + I_{w.net} + 2I_{bt.net} + I_{bf.net} - A_{duct} \cdot \left(x_{net} - y_{duct.net}\right)^2 = 2.682 \times 10^{-3}\,m^4$$

$$I_I := I_{tf.I} + 2I_{tt.I} + I_{w.I} + 2I_{bt.I} + I_{bf.I} - \left(\alpha_p - 1\right) \cdot A_p \cdot \left(y_{duct.I} - x_I\right)^2 = 2.66 \times 10^{-3}\,m^4$$

LOAD EFFECTS

Loads

Self weight: $\rho_{concrete} := 2500\frac{kg}{m^3}$ $g = 9.807\frac{m}{s^2}$

$g_k := \rho_{concrete}\cdot g\cdot A_c = 2.819\cdot\frac{kN}{m}$

Point loads: $P_k := 52.5kN$

Safety factors: $\gamma_{G.1} := 1$ $g := \gamma_{G.1}\cdot g_k = 2.819\frac{1}{m}\cdot kN$

$\gamma_{Q.1} := 1$ $P := \gamma_{Q.1}\cdot P_k = 52.5\cdot kN$

SLS - Unloaded case (before application of tendon force)

$R_A := \frac{g_k\cdot l}{2} = 11.278\cdot kN$ $R_B := R_A$

$M_{g0}(x) := \frac{-g_k\cdot x^2}{2} + R_A\cdot x$ $M_{g0.SLS} := M_{g0}\left(\frac{l}{2}\right) = 22.555\cdot kN\cdot m$

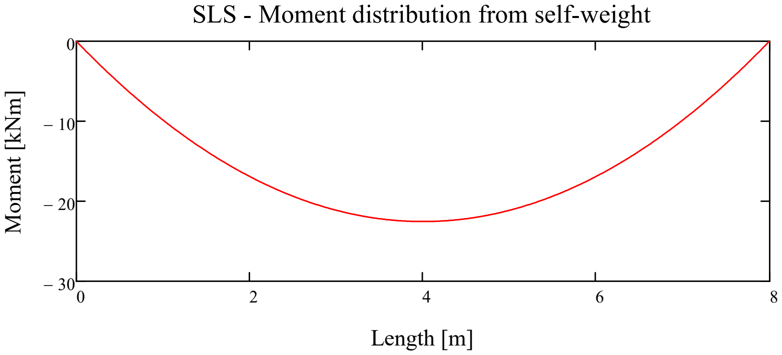

ULS - Unloaded case (before application of tendon force)

$R_A := \frac{g\cdot l}{2} = 11.278\cdot kN$ $R_B := R_A$

$M_{g0}(x) := \frac{-g\cdot x^2}{2} + R_A\cdot x$ $M_{g0.ULS} := M_{g0}\left(\frac{l}{2}\right) = 22.555\cdot kN\cdot m$

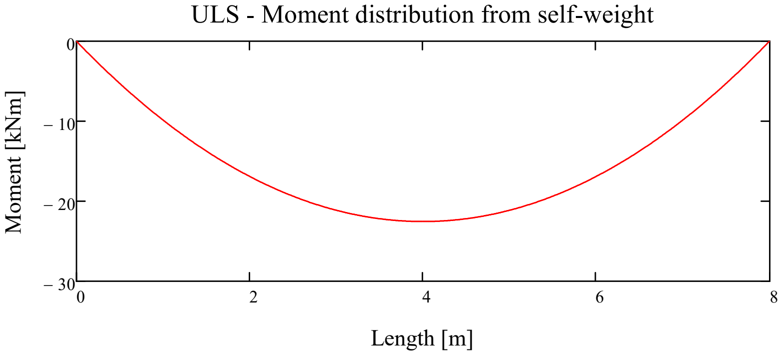

SLS - Loaded case (after application of point loads)

$R_A := \frac{g_k \cdot l + 2P_k}{2} = 63.778 \cdot kN \qquad R_B := R_A$

$x_1 := 0m, 0.01m .. l_1 \qquad x_2 := l_1, l_1 + 0.01m .. l_1 + l_2 \qquad x_3 := l_1 + l_2, l_1 + l_2 + 0.01m .. l$

$M_1(x) := \frac{-g_k \cdot x^2}{2} + R_A \cdot x \qquad V_1(x) := -g_k \cdot x + R_A$

$M_2(x) := \frac{-g_k \cdot x^2}{2} - P_k \cdot (x - l_1) + R_A \cdot x \qquad V_2(x) := -g_k \cdot x - P_k + R_A$

$M_3(x) := -\frac{g_k \cdot x^2}{2} - P_k \cdot (x - l_1) - P_k \cdot (x - l_1 - l_2) + R_A \cdot x \qquad V_3(x) := -g_k \cdot x - 2P_k + R_A$

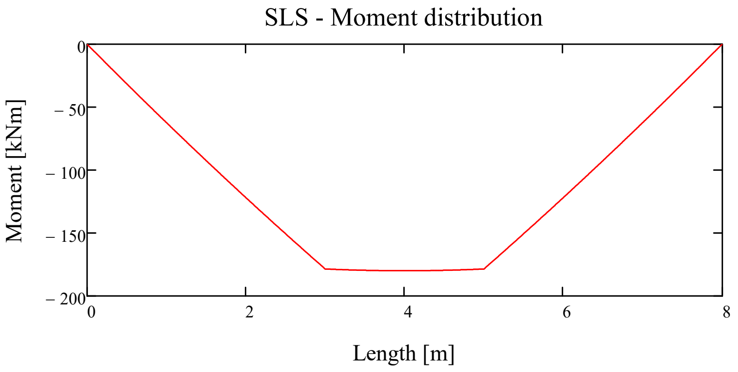

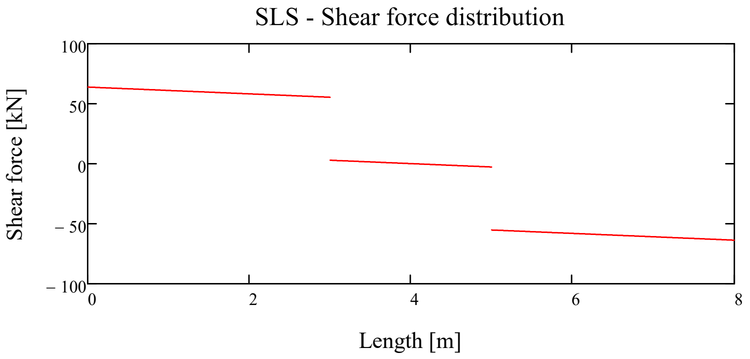

$M_{Ek} := M_2\left(\frac{l}{2}\right) = 180.055 \cdot kN \cdot m$

$V_{Ek} := V_1(0m) = 63.778 \cdot kN$

ULS - Loaded case (after application of point loads)

$R_A := \frac{g \cdot l + 2P}{2} = 63.778 \cdot kN$ $\qquad$ $R_B := R_A$

$x_1 := 0m, 0.01m .. l_1$ $\qquad$ $x_2 := l_1, l_1 + 0.01m .. l_1 + l_2$ $\qquad$ $x_3 := l_1 + l_2, l_1 + l_2 + 0.01m .. l$

$M_1(x) := \frac{-g \cdot x^2}{2} + R_A \cdot x$ $\qquad$ $V_1(x) := -g \cdot x + R_A$

$M_2(x) := \frac{-g \cdot x^2}{2} - P \cdot \left(x - l_1\right) + R_A \cdot x$ $\qquad$ $V_2(x) := -g \cdot x - P + R_A$

$M_3(x) := -\frac{g \cdot x^2}{2} - P \cdot \left(x - l_1\right) - P \cdot \left(x - l_1 - l_2\right) + R_A \cdot x$ $\qquad$ $V_3(x) := -g \cdot x - 2P + R_A$

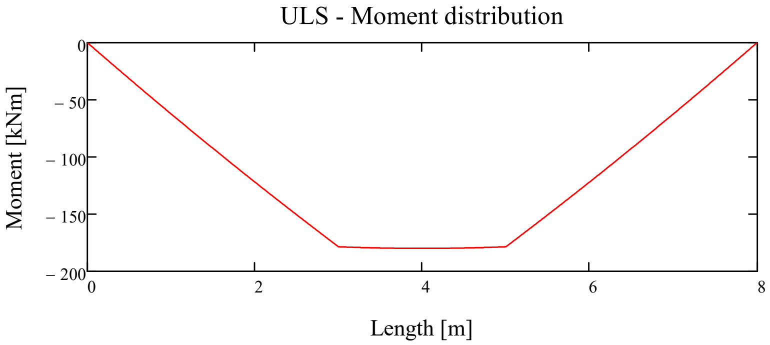

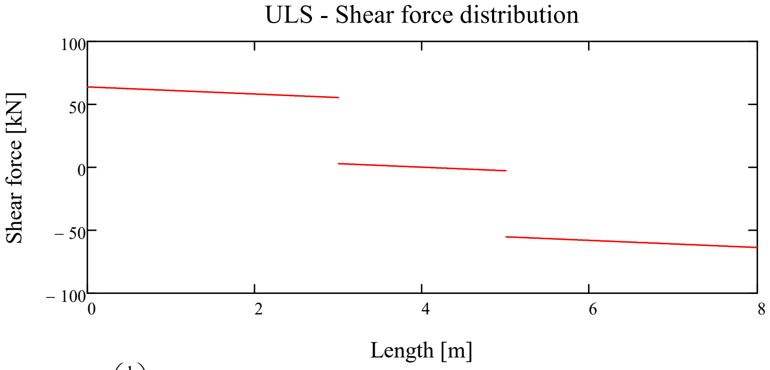

$M_{Ed} := M_2\left(\frac{l}{2}\right) = 180.055 \cdot kN \cdot m$ $\qquad$ $V_{Ed} := V_1(0m) = 63.778 \cdot kN$

PRELIMINARY DESIGN

Estimation of needed cross section (no cracks allowed)

$M_q := M_{Ek} - M_{g0.SLS} = 157.5 \cdot kN \cdot m$

$\psi_2 := 0 \qquad M_{qt} := M_q$

$\eta := 0.8$

Edge 1: $\left| \begin{array}{l} \text{"OK"} \quad \text{if } \dfrac{I_c}{x_c} \geq \dfrac{M_{qt} + (1-\eta) \cdot M_{g0.SLS}}{\left|\sigma_{cc.inf.max}\right| + \eta \cdot \sigma_{cti.max}} \\ \text{"Not OK"} \quad \text{otherwise} \end{array} \right. = \text{"OK"}$

Edge 2: $\left| \begin{array}{l} \text{"OK"} \quad \text{if } \dfrac{I_c}{h - x_c} \geq \dfrac{M_q + (1-\eta) \cdot M_{g0.SLS}}{\eta \left|\sigma_{cci.max}\right| + \sigma_{ct.inf.max}} \\ \text{"Not OK"} \quad \text{otherwise} \end{array} \right. = \text{"OK"}$

Value of prestressing force with known eccentricity

$r_{sup} := 1.1 \qquad r_{inf} := 0.9$

$$P_{i.top.max} := \frac{M_{g0.SLS} + \dfrac{I_c}{x_c} \cdot \sigma_{cti.max7}}{r_{sup}\left(e_f - \dfrac{I_c}{x_c \cdot A_c}\right)} = 0.562 \cdot MN$$

$$P_{i.bottom.max} := \frac{M_{g0.SLS} + \dfrac{I_c}{h - x_c} \cdot \left|\sigma_{cci.max7}\right|}{r_{sup}\left[e_f + \dfrac{I_c}{\left(h - x_c\right) \cdot A_c}\right]} = 0.804 \cdot MN$$

$P_{i.max} := \min\left(P_{i.top.max}, P_{i.bottom.max}\right) = 562.408 \cdot kN$

$$P_{i.top.min} := \frac{1}{\eta} \cdot \frac{M_{g0.SLS} + M_{qt} - \dfrac{I_c}{x_c} \cdot \left|\sigma_{cc.inf.max}\right|}{r_{inf}\left(e_f - \dfrac{I_c}{x_c \cdot A_c}\right)} = -3.68 \cdot MN$$

$$P_{i.bottom.min} := \frac{1}{\eta} \cdot \frac{M_{g0.SLS} + M_q - \dfrac{I_c}{h - x_c} \cdot \left|\sigma_{ct.inf.max}\right|}{r_{inf}\left[e_f + \dfrac{I_c}{\left(h - x_c\right) \cdot A_c}\right]} = 0.557 \cdot MN$$

$P_{i.min} := \max\left(P_{i.top.min}, P_{i.bottom.min}\right) = 556.771 \cdot kN$

Is prestressing force in allowable range? $\left| \begin{array}{l} \text{"OK"} \quad \text{if } P_{i.min} \leq P_{i.1} \leq P_{i.max} \\ \text{"Not OK"} \quad \text{otherwise} \end{array} \right. = \text{"OK"}$

$P_{k.sup} := r_{sup} \cdot P_{i.1} = 617.1 \cdot kN$

$P_{k.inf} := r_{inf} \cdot P_{i.1} = 504.9 \cdot kN$

$$\sigma_{pi} := \min\left(0.8 \cdot f_{puk}, 0.9 \cdot f_{p0.1k}\right) = 1.476 \times 10^{3} \cdot \text{MPa}$$

$$A_{p.} := \frac{P_{i.1}}{\sigma_{pi}} = 3.801 \times 10^{-4} \, m^{2}$$

$$n_{tendon.} := \frac{A_{p.}}{A_{pi}} = 2.534$$

Concrete stress (check cracking)

At tensioning:

$$\sigma_{cti} := \frac{-P_{k.sup}}{A_c} + \frac{-P_{k.sup} \cdot e_f + M_{g0.SLS}}{I_c} \cdot \left(-x_c\right) = 2.778 \cdot \text{MPa}$$

$$\sigma_{cci} := \frac{-P_{k.sup}}{A_c} + \frac{-P_{k.sup} \cdot e_f + M_{g0.SLS}}{I_c} \cdot \left(h - x_c\right) = -14.572 \cdot \text{MPa}$$

Top edge:
$$\left| \begin{array}{l} \text{"OK"} \quad \text{if } \sigma_{cti} \le \sigma_{cti.max7} \\ \text{"Not OK"} \quad \text{otherwise} \end{array} \right. = \text{"OK"}$$

Bottom edge:
$$\left| \begin{array}{l} \text{"OK"} \quad \text{if } \sigma_{cci} \ge -\left|\sigma_{cci.max7}\right| \\ \text{"Not OK"} \quad \text{otherwise} \end{array} \right. = \text{"OK"}$$

After loading (no cracks allowed in SLS):

$$\sigma_{cc.inf} := \frac{-\eta \cdot P_{k.inf}}{A_c} + \frac{-\eta \cdot P_{k.inf} \cdot e_f + M_{g0.SLS} + M_{qt}}{I_c} \cdot -x_c = -11.693 \cdot \text{MPa}$$

$$\sigma_{ct.inf} := \frac{-\eta \cdot P_{k.inf}}{A_c} + \frac{-\eta \cdot P_{k.inf} \cdot e_f + M_{g0.SLS} + M_{q}}{I_c} \cdot \left(h - x_c\right) = 5.735 \cdot \text{MPa}$$

Top edge:
$$\left| \begin{array}{l} \text{"OK"} \quad \text{if } \sigma_{cc.inf} \ge -\left|\sigma_{cc.inf.max}\right| \\ \text{"Not OK"} \quad \text{otherwise} \end{array} \right. = \text{"OK"}$$

Bottom edge:
$$\left| \begin{array}{l} \text{"OK"} \quad \text{if } \sigma_{ct.inf} \le \sigma_{ct.inf.max} \\ \text{"Not OK"} \quad \text{otherwise} \end{array} \right. = \text{"OK"}$$

Bending moment capacity of cross section

Required concrete cover

$\Delta c_{dev} := 10\text{mm}$

$c_{nom} := \phi + \Delta c_{dev} = 26\cdot\text{mm}$

$d := h - \left(c_{nom} + \phi_{stirrup} + \frac{\phi}{2}\right) = 0.433\,\text{m}$

$c_1 := c_{nom} + \phi_{stirrup} + \frac{\phi}{2} = 42\cdot\text{mm}$

$d_g := 16\text{mm}$ from manufacturer

$k_1 := 1.0 \qquad k_2 := 5\text{mm}$

$c_{bar} := \max\left(k_1\cdot\phi, d_g + k_2, 20\text{mm}\right) = 21\cdot\text{mm}$

Effective prestressing force

Tendon force: $\mu := 0.19 \qquad \alpha := \operatorname{atan}\left(\frac{e_f}{l_1}\right) \qquad k := \frac{0.0075}{\text{m}}$

$P_i(x) := P_{i.1}\cdot e^{-\mu\cdot(\alpha+k\cdot x)}$

$$\sigma_{cpi} := \frac{-P_i\left(\frac{l}{2}\right)}{A_{net}} + \frac{-P_i\left(\frac{l}{2}\right)\cdot e_{net} + M_{g0.SLS}}{I_{net}}\cdot e_{net} = -11.052\cdot\text{MPa}$$

$$\varepsilon_{p0i} := \frac{P_i\left(\frac{l}{2}\right)}{E_p\cdot A_p} - \frac{\sigma_{cpi}}{E_{cm}} = 6.729\times 10^{-3}$$

$P_{0.i} := E_p\cdot\varepsilon_{p0i}\cdot A_p = 575.3\cdot\text{kN}$

Amount of reinforcement

Top layer: $n_{max} := 4$

$$\frac{b_{tf}}{2\cdot\left(c_{nom} + \phi_{stirrup} + \frac{\phi}{2}\right) + n_{max}\cdot\phi + \left(n_{max} - 1\right)\cdot c_{bar}} = 1.801$$

Bottom layer: $n_{max} := 4$

$$\frac{b_{bf}}{2\cdot\left(c_{nom} + \phi_{stirrup} + \frac{\phi}{2}\right) + n_{max}\cdot\phi + \left(n_{max} - 1\right)\cdot c_{bar}} = 1.327$$

$d_1 := d = 0.433\,\text{m}$

$d_2 := d_1 - c_{bar} - \frac{2\phi}{2} = 0.396\,\text{m}$

$d_p := x_c + e_f = 0.421\,\text{m}$

$d_{prim} := \left(c_{nom} + \phi_{stirrup} + \frac{\phi}{2}\right) = 0.042\,\text{m}$

Horizontal force equilibrium

$\alpha := 0.810 \qquad \beta := 0.416 \qquad \varepsilon_{cu} := 3.5 \cdot 10^{-3}$

$f_{p0.1k} = 1.64 \times 10^{3} \cdot \text{MPa} \qquad f_{pd} := \dfrac{f_{p0.1k}}{1.15} = 1.426 \times 10^{3} \cdot \text{MPa}$

$$x := \alpha \cdot f_{cd} \cdot b_{tf} \cdot x + \frac{x - d_{prim}}{x} \cdot \varepsilon_{cu} \cdot E_s \cdot A_{s.prim} - \left(f_{pd} \cdot A_p + f_{yd} \cdot A_{s1}\right) = 0 \text{ solve}, x \rightarrow \begin{bmatrix} -\dfrac{2.82019348783481337 09e\text{-}29 \cdot \left(\sqrt{3.1693}\right.}{} \\ \dfrac{2.8201934878348133709e\text{-}29 \cdot \left(\sqrt{3.16939}\right.}{} \end{bmatrix}$$

$x := x_1 = 0.053\,\text{m}$

$\left| \begin{array}{l} \text{"Compression zone in top flange"} \quad \text{if } x \le h_{tf} \\ \text{"Recalculate"} \quad \text{otherwise} \end{array} \right. = \text{"Compression zone in top flange"}$

$\left| \begin{array}{l} \text{"Top reinforcement in compression zone"} \quad \text{if } x > d_{prim} \\ \text{"Recalculate"} \quad \text{otherwise} \end{array} \right. = \text{"Top reinforcement in compression zone"}$

$$b_t := \frac{\left[(h - x) - h_{bf}\right] \cdot b_w + \left(h - x - h_w\right) \cdot b_{bf}}{\left[(h - x) - h_{bf}\right] + \left(h - x - h_w\right)} = 0.198\,\text{m}$$

$A_{s.min} := 0.26 \cdot \dfrac{f_{ctm}}{f_{yk}} \cdot b_t \cdot d = 1.992 \times 10^{-4}\,\text{m}^2 \qquad A_{s.max} := 0.04 A_c = 4.6 \times 10^{-3}\,\text{m}^2$

$\left| \begin{array}{l} \text{"OK"} \quad \text{if } A_{s.min} < A_{s.tot} < A_{s.max} \\ \text{"Not OK"} \quad \text{otherwise} \end{array} \right. = \text{"OK"}$

Deformation conditions

$\varepsilon_{s.prim} := \dfrac{x - d_{prim}}{x} \cdot \varepsilon_{cu} = 7.01 \times 10^{-4}$

$\varepsilon_{sy} := \dfrac{f_{yd}}{E_s} = 2.5 \times 10^{-3}$

$\varepsilon_{s1} := \dfrac{d_1 - x}{x} \cdot \varepsilon_{cu} = 0.025$

$\varepsilon_p := \dfrac{d_p - x}{x} \cdot \varepsilon_{cu} = 0.025 \qquad \varepsilon_{pd} := \dfrac{f_{pd}}{E_p} = 7.506 \times 10^{-3}$

Steel tendon strain is decisive, concrete stress block is not fully developed but ok for preliminary design!

Moment equilibrium at prestressing steel level

$$M_{Rd} := \alpha \cdot f_{cd} \cdot b_{tf} \cdot x \cdot \left(d_p - \beta \cdot x\right) + \frac{x - d_{prim}}{x} \cdot \varepsilon_{cu} \cdot E_s \cdot A_{s.prim} \cdot \left(d_p - d_{prim}\right) + f_{yd} \cdot A_{s1} \cdot \left(d_1 - d_p\right)$$

$M_{Rd} = 419.195 \cdot \text{kN} \cdot \text{m} \qquad M_{Ed} = 180.055 \cdot \text{kN} \cdot \text{m}$

$\eta := \dfrac{\left|M_{Ed}\right|}{M_{Rd}} = 42.953 \cdot \%$

Refine calculation after infinite time effects have been introduced.

Accurate design

Before grouting of ducts

$$\sigma_{cti} := \frac{-P_{0.i}}{A_{net}} + \frac{-P_{0.i}\cdot e_{net} + M_{g0.SLS}}{I_{net}}\cdot\left(-x_{net}\right) = 2.846\cdot\text{MPa}$$

$$\sigma_{cci} := \frac{-P_{0.i}}{A_{net}} + \frac{-P_{0.i}\cdot e_{net} + M_{g0.SLS}}{I_{net}}\cdot\left(h - x_{net}\right) = -13.466\cdot\text{MPa}$$

Top edge:

$$\left|\begin{array}{l}\text{"OK"} \quad \text{if } \sigma_{cti} \le \sigma_{cti.max7} \\ \text{"Not OK"} \quad \text{otherwise}\end{array}\right. = \text{"Not OK"}$$

Bottom edge:

$$\left|\begin{array}{l}\text{"OK"} \quad \text{if } \sigma_{cci} \ge -\left|\sigma_{cci.max7}\right| \\ \text{"Not OK"} \quad \text{otherwise}\end{array}\right. = \text{"OK"}$$

Concrete will not crush or crack before grouting. Moving beam not considered here.

After grouting of ducts (infinite time)

Relaxation class 2:

$$\chi_{1000} := 2.5\% \qquad \mu := 0.7$$

$$\chi(t) := 0.66\cdot\chi_{1000}\cdot e^{9.1\cdot\mu}\cdot\left(\frac{t}{1000h}\right)^{0.75\cdot(1-\mu)}\cdot 10^{-3}$$

$$\chi_{inf} := \chi(500000h) = 0.048$$

Final shrinkage:

$$u := 2\cdot\left[\begin{array}{l}\dfrac{b_{tf}}{2} + h_{bf} + \sqrt{b_{tt}^{\,2} + h_{tt}^{\,2}} + \left(h_w - h_{tt} - h_{bt}\right) \ldots \\ + \sqrt{b_{bt}^{\,2} + h_{bt}^{\,2}} + h_{bf} + \dfrac{b_{bf}}{2}\end{array}\right] = 1.935\,\text{m}$$

$$h_0 := \frac{2\cdot A_c}{u} = 0.119\,\text{m}$$

$$k_h := \frac{\dfrac{h_0}{mm} - \left(100 - \dfrac{100}{-0.15}\right)}{\dfrac{100}{-0.15}} = 0.972$$

$$RH := 50\%$$

$$\beta_{RH} := 1.55\cdot\left[1 - \left(\frac{RH}{100\%}\right)^3\right] = 1.356$$

$$\varepsilon_{cdi} := 0.354\cdot 10^{-3}$$

$$\varepsilon_{cd.inf} := k_h\cdot\beta_{RH}\cdot\varepsilon_{cdi} = 4.665\times 10^{-4}$$

$$\beta_{ds} := \frac{75 - 4}{(74 - 4) + 0.04\cdot\sqrt{\left(\dfrac{h_0}{mm}\right)^3}} = 0.583$$

$$\varepsilon_{cd} := \varepsilon_{cd.inf}$$

$$\varepsilon_{ca} := 0.125\cdot 10^{-3}$$

$$\varepsilon_{cs} := \varepsilon_{cd} + \varepsilon_{ca} = 5.915\times 10^{-4}$$

Force from shrinkage:

$F_{cs.p} := E_p \cdot \varepsilon_{cs} \cdot A_p = 50.574 \cdot kN$

$F_{cs.s} := E_s \cdot \varepsilon_{cs} \cdot A_{s1} = 95.145 \cdot kN$

$F_{cs.s.prim} := E_s \cdot \varepsilon_{cs} \cdot A_{s.prim} = 95.145 \cdot kN$

Creep:

$$\varphi_{RH} := \left[1 + \frac{1 - \frac{RH}{100\%}}{0.1 \cdot \sqrt[3]{\frac{h_0}{mm}}} \cdot \left(\frac{35MPa}{f_{cm}} \right)^{0.7} \right] \cdot \left(\frac{35MPa}{f_{cm}} \right)^{0.2} = 1.46$$

$$\beta_{fcm} := \frac{16.8}{\sqrt{\frac{f_{ck}}{MPa} + 8}} = 2.074$$

$t_0 := 11$ $\qquad$ $t_1 := 75$

$\beta_{t0} := \dfrac{1}{0.1 + t_0^{\,0.2}} = 0.583$ $\qquad$ $\beta_{t1} := \dfrac{1}{0.1 + t_1^{\,0.2}} = 0.405$

$\varphi_{0.1} := \varphi_{RH} \cdot \beta_{fcm} \cdot \beta_{t0} = 1.765$

$\varphi_{0.2} := \varphi_{RH} \cdot \beta_{fcm} \cdot \beta_{t1} = 1.225$

$\beta_{c.75.7} := 0.52$ $\qquad$ $\varphi_{1.75.7} := \beta_{c.75.7} \cdot \varphi_{0.1} = 0.918$

$\beta_{c.inf.7} := 1$ $\qquad$ $\varphi_{1.inf.7} := \beta_{c.inf.7} \cdot \varphi_{0.1} = 1.765$

$\beta_{c.inf.75} := 1$ $\qquad$ $\varphi_{2.inf.75} := \beta_{c.inf.75} \cdot \varphi_{0.2} = 1.225$

$$\varphi_{ef.inf} := \frac{\left(M_{g0.SLS} - P_i\left(\frac{1}{2}\right) \cdot e_f \right) \cdot \varphi_{1.inf.7} + \left(M_{Ek} - M_{g0.SLS} \right) \cdot \varphi_{2.inf.75}}{M_{Ek} - P_i\left(\frac{1}{2}\right) \cdot e_f} = 0.567$$

Effective sectional constants:

$$\alpha_{p.ef} := \frac{E_p \cdot \left(1 - \chi_{inf}\right)}{E_{cm}} \cdot \left(1 + \varphi_{ef.inf}\right)$$

$$\alpha_{s.ef} := \frac{E_s}{E_{cm}} \cdot \left(1 + \varphi_{ef.inf}\right)$$

$$x_{I.ef} := \frac{A_{tf} \cdot y_{tf} + 2A_{tt} \cdot y_{tt} + A_w \cdot y_w + 2A_{bt} \cdot y_{bt} + A_{bf} \cdot y_{bf} \cdots + \left(\alpha_{p.ef} - 1\right) \cdot A_p \cdot y_{duct.I} + \left(\alpha_{s.ef} - 1\right) \cdot A_{s.prim} \cdot d_{prim} \cdots + \left(\alpha_{s.ef} - 1\right) \cdot A_{s1} \cdot d_1}{A_{I.ef}} = 0.229\,m$$

$$I_{tf.I.ef} := \frac{b_{tf} \cdot h_{tf}^{\,3}}{12} + A_{tf} \cdot \left(x_{I.ef} - y_{tf}\right)^2$$

$$I_{tt.I.ef} := \frac{b_{tt} \cdot h_{tt}^{\,3}}{36} + A_{tt} \cdot \left(x_{I.ef} - y_{tt}\right)^2$$

$$I_{w.I.ef} := \frac{b_w \cdot h_w^{\,3}}{12} + A_w \cdot \left(x_{I.ef} - y_w\right)^2$$

$$I_{bt.I.ef} := \frac{b_{bt} \cdot h_{bt}^{\,3}}{36} + A_{bt} \cdot \left(x_{I.ef} - y_{bt}\right)^2$$

$$I_{bf.I.ef} := \frac{b_{bf} \cdot h_{bf}^3}{12} + A_{bf} \cdot \left(x_{I.ef} - y_{bf}\right)^2$$

$$I_{I.ef} := I_{tf.I.ef} + 2 I_{tt.I.ef} + I_{w.I.ef} + 2 I_{bt.I.ef} \cdots = 2.622 \times 10^{-3}\,m^4$$
$$+ I_{bf.I.ef} - \left(\alpha_{p.ef} - 1\right) \cdot A_p \cdot \left(y_{duct.I} - x_{I.ef}\right)^2$$

$$e_{p.ef} := d_p - x_{I.ef} = 0.192\,m$$

$$e_{s.ef} := d - x_{I.ef} = 0.204\,m$$

$$e_{s.ef.prim} := x_{I.ef} - d_{prim} = 0.187\,m$$

$$\sigma_{cc.inf} := \frac{-\left(1 - \chi_{inf}\right) \cdot \left(P_{0.i} - F_{cs.p}\right) \cdots + F_{cs.s} - F_{cs.s.prim}}{A_{I.ef}} + \frac{-\left(1 - \chi_{inf}\right) \cdot \left(P_{0.i} - F_{cs.p}\right) \cdot e_{p.ef} \cdots + F_{cs.s} \cdot e_{s.ef} + F_{cs.s.prim} \cdot e_{s.ef.prim} \cdots + M_{g0.SLS} + M_{qt}}{I_{I.ef}} \cdot -x_{I.ef} = -14.439 \cdot MPa$$

$$\sigma_{ct.inf} := \frac{-\left(1 - \chi_{inf}\right) \cdot \left(P_{0.i} - F_{cs.p}\right) \cdots + F_{cs.s} - F_{cs.s.prim}}{A_{I.ef}} + \frac{-\left(1 - \chi_{inf}\right) \cdot \left(P_{0.i} - F_{cs.p}\right) \cdot e_{p.ef} \cdots + F_{cs.s} \cdot e_{s.ef} + F_{cs.s.prim} \cdot e_{s.ef.prim} \cdots + M_{g0.SLS} + M_q}{I_{I.ef}} \cdot \left(h - x_{I.ef}\right) = 7.525 \cdot MPa$$

$$\left| \begin{array}{l} \text{"OK" if } \sigma_{cc.inf} \ge -\left|\sigma_{cc.inf.max}\right| \\ \text{"Not OK" otherwise} \end{array} \right. = \text{"OK"}$$

$$\left| \begin{array}{l} \text{"OK" if } \sigma_{ct.inf} \le \sigma_{ct.inf.max} \\ \text{"Cracks will occur at infinite time" otherwise} \end{array} \right. = \text{"Cracks will occur at infinite time"}$$

$$\sigma_{cp.inf} := \frac{-\left(1 - \chi_{inf}\right) \cdot \left(P_{0.i} - F_{cs.p}\right) \cdots + F_{cs.s} - F_{cs.s.prim}}{A_{I.ef}} + \frac{-\left(1 - \chi_{inf}\right) \cdot \left(P_{0.i} - F_{cs.p}\right) \cdot e_{p.ef} \cdots + F_{cs.s} \cdot e_{s.ef} + F_{cs.s.prim} \cdot e_{s.ef.prim} \cdots + M_{g0.SLS} + M_{qt}}{I_{I.ef}} \cdot \left(d_p - x_{I.ef}\right) = 5.027 \cdot MPa$$

$$\sigma_{p0.inf} := \frac{\left(1 - \chi_{inf}\right) \cdot \left(P_{0.i} - F_{cs.p}\right)}{A_p} + \alpha_{p.ef} \cdot \sigma_{cp.inf} = 1.147 \times 10^3 \cdot MPa$$

$$\varepsilon_{p0.inf} := \frac{\sigma_{p0.inf}}{E_p} = 6.035 \times 10^{-3}$$

$$\Delta\varepsilon_p := \varepsilon_{pd} - \varepsilon_{p0.inf} = 1.471 \times 10^{-3}$$

Horizontal equilibrium:

$hv := 0.347 \quad bv := 0.270 \quad \varepsilon_{cc.max} := 0.8$

Assume: $\varepsilon_{cc} := 0.66 \times 10^{-3}$

$$\alpha_R := \frac{hv - bv}{0.2 \cdot 10^{-3}} \cdot \varepsilon_{cc} + \left[hv - \frac{\varepsilon_{cc.max}}{0.2} \cdot (hv - bv)\right] = 0.293$$

$hv := 0.346 \quad bv := 0.343$

$$\beta_R := \frac{hv - bv}{0.2 \cdot 10^{-3}} \cdot \varepsilon_{cc} + \left[hv - \frac{\varepsilon_{cc.max}}{0.2} \cdot (hv - bv)\right] = 0.344$$

$$x_{comp} := \alpha_R \cdot f_{cd} \cdot b_{tf} \cdot x_{comp} + \frac{x_{comp} - d_{prim}}{x_{comp}} \cdot \varepsilon_{cc} \cdot E_s \cdot A_{s.prim} - \left(f_{pd} \cdot A_p + \frac{d_1 - x_{comp}}{x_{comp}} \cdot \varepsilon_{cc} \cdot E_s \cdot A_{s1} \right) = 0 \text{ solve}, x_{comp} \rightarrow \begin{bmatrix} -\underline{9.3} \\ \underline{9.35} \end{bmatrix}$$

$$x := x_{comp_1} = 0.128\,m$$

$$x := \frac{\varepsilon_{cc}}{\varepsilon_{cc} + \Delta\varepsilon_p} \cdot d_p = 0.13\,m$$

$$\begin{vmatrix} \text{"OK"} \quad \text{if } x < h_{tf} \\ \text{"Neutral layer in web, recalculate"} \quad \text{otherwise} \end{vmatrix} = \text{"Neutral layer in web, recalculate"}$$

Assume neutral layer in web:

$$\varepsilon_{cc} := 0.7 \times 10^{-3}$$

$$hv := 0.347 \qquad bv := 0.270 \qquad \varepsilon_{cc.max} := 0.8$$

$$\alpha_R := \frac{hv - bv}{0.2 \cdot 10^{-3}} \cdot \varepsilon_{cc} + \left[hv - \frac{\varepsilon_{cc.max}}{0.2} \cdot (hv - bv) \right] = 0.309$$

$$hv := 0.346 \qquad bv := 0.343$$

$$\beta_R := \frac{hv - bv}{0.2 \cdot 10^{-3}} \cdot \varepsilon_{cc} + \left[hv - \frac{\varepsilon_{cc.max}}{0.2} \cdot (hv - bv) \right] = 0.345$$

$$x_{comp2} := \alpha_R \cdot f_{cd} \cdot A_{tf} + 2\alpha_R \cdot f_{cd} \cdot A_{tt} + \alpha_R \cdot f_{cd} \cdot b_w \cdot \left(x_{comp2} - h_{tf} \right) + \frac{x_{comp2} - d_{prim}}{x_{comp2}} \cdot \varepsilon_{cc} \cdot E_s \cdot A_{s.prim} - \left(f_{pd} \cdot A_p + \frac{d_1 - x_{comp2}}{x_{comp2}} \right.$$

$$x := \max\left(x_{comp2} \right) = 0.134\,m$$

$$x := \frac{\varepsilon_{cc}}{\varepsilon_{cc} + \Delta\varepsilon_p} \cdot d_p = 0.136\,m$$

x in web, OK!

Deformation conditions

$$\varepsilon_{s.prim} := \frac{x - d_{prim}}{x} \cdot \varepsilon_{cc} = 4.834 \times 10^{-4}$$

$$\varepsilon_{sy} := \frac{f_{yd}}{E_s} = 2.5 \times 10^{-3}$$

$$\varepsilon_{s1} := \frac{d_1 - x}{x} \cdot \varepsilon_{cc} = 1.533 \times 10^{-3}$$

Moment equilibrium

$$M_{Rd} := \alpha_R \cdot f_{cd} \cdot \left(b_{tf} - b_w \right) \cdot h_{tf} \cdot \left(d_p - \beta_R \cdot h_{tf} \right) + \alpha_R \cdot f_{cd} \cdot b_w \cdot x \cdot \left(d_p - \beta_R \cdot x \right) \ldots = 319.886 \cdot kN \cdot m$$
$$+ \varepsilon_{s.prim} \cdot E_s \cdot A_{s.prim} \cdot \left(d_p - d_{prim} \right) + \varepsilon_{s1} \cdot E_s \cdot A_{s1} \cdot \left(d_p - d_1 \right)$$

$$M_{Rd} = 319.886 \cdot kN \cdot m \qquad M_{Ed} = 180.055 \cdot kN \cdot m$$

$$\eta := \frac{M_{Ed}}{M_{Rd}} = 56.287 \cdot \%$$

Splice length of longitudinal reinforcement

$\alpha_1 := 1.0 \quad \alpha_2 := 1.0 \quad \alpha_3 := 1.0 \quad \alpha_5 := 1.0 \quad \alpha_6 := 1.5$

Conservative assumption

$\sigma_s := \max(\varepsilon_{s.prim} \cdot E_s, \varepsilon_{s1} \cdot E_s)$

$\eta_1 := 1.0 \quad \eta_2 := 1.0$

$f_b := 2.25 \cdot \eta_1 \cdot \eta_2 \cdot f_{ctd}$

$$l_{b.rqd} := \frac{\sigma_s}{f_b} \cdot \frac{\phi}{4} = 0.174\,m$$

$l_0 := \alpha_1 \cdot \alpha_2 \cdot \alpha_3 \cdot \alpha_5 \cdot \alpha_6 \cdot l_{b.rqd} = 0.261\,m$

$l_{0.min} := \max(0.3 \cdot \alpha_6 \cdot l_{b.rqd}, 15 \cdot \phi, 200mm) = 0.24\,m$

SLS Calculations

Sectional constants - State II

Guess: $x_{II} := 100.08mm$ in web

$A_{cc} := A_{tf} + 2 \cdot A_{tt} + b_w \cdot (x_{II} - h_{tf})$

$A_{II} := A_{cc} + (\alpha_s - 1) \cdot A_{s.prim} + \alpha_s \cdot A_{s1} + \alpha_p \cdot A_p = 0.051\,m^2$

$$x_{tp.cc} := \frac{A_{tf} \cdot y_{tf} + 2 \cdot A_{tt} \cdot y_{tt} + b_w \cdot (x_{II} - h_{tf}) \cdot \left[\frac{(x_{II} - h_{tf})}{2} + h_{tf}\right]}{A_{tf} + 2 \cdot A_{tt} + b_w \cdot (x_{II} - h_{tf})} = 0.054\,m$$

$$x_{II} := \frac{A_{cc} \cdot x_{tp.cc} + (\alpha_s - 1) \cdot A_{s.prim} \cdot d_{prim} + \alpha_s \cdot A_{s1} \cdot d_1 + \alpha_p \cdot A_p \cdot d_p}{A_{II}} = 100.08 \cdot mm$$

$$I_{II} := \frac{b_{tf} \cdot x_{II}^3}{12} + A_{cc} \cdot \left(x_{II} - \frac{x_{II}}{2}\right)^2 + (\alpha_s - 1) \cdot A_{s.prim} \cdot (x_{II} - d_{prim})^2 \ldots = 8.339 \times 10^{-4}\,m^4$$
$$+ \alpha_s \cdot A_{s1} \cdot (d_1 - x_{II})^2 + \alpha_p \cdot A_p \cdot (d_p - x_{II})^2$$

$e_{II} := h - x_{II} - 68.5mm = 0.306\,m \qquad e_{II} := e_f = 0.198\,m$

Distance between cracks

$k_1 := 0.8 \quad k_2 := 0.5 \quad k_3 := 3.4 \quad k_4 := 0.425$

$$h_{c.ef} := \min\left[2.5 \cdot (h - d), \frac{h - x_{II}}{2}, \frac{h}{2}\right] = 0.105\,m \qquad A_{ef} := h_{c.ef} \cdot b_{bf} = 0.029\,m^2$$

$$\rho_{p.ef} := \frac{A_{s1} + A_p}{A_{ef}}$$

$$s_{r.max} := k_3 \cdot c_1 + k_1 \cdot k_2 \cdot k_4 \cdot \frac{\phi}{\rho_{p.ef}} = 0.207\,m$$

Crack width

$$\sigma_{II}(z) := \frac{-P_i\left(\frac{1}{2}\right)}{A_{II}} + \frac{-P_i\left(\frac{1}{2}\right)\cdot e_{II} + M_{Ek}}{I_{II}}\cdot z$$

$$\sigma_s := \alpha_s\cdot\sigma_{II}\left(d_1 - x_{II}\right) = 90.239\cdot\mathrm{MPa}$$

$$k_t := 0.6$$

$$\Delta\varepsilon := \frac{\sigma_s - k_t\cdot\frac{f_{ctm}}{\rho_{p.ef}}\cdot\left(1 + \alpha_s\cdot\rho_{p.ef}\right)}{E_s} = 6.715\times 10^{-5}$$

$$w_k := \Delta\varepsilon\cdot s_{r.max} = 0.014\cdot\mathrm{mm}$$

$$\left|\begin{array}{l} \text{"OK"} \quad \text{if } 0\mathrm{mm} < w_k < 0.2\mathrm{mm} \\ \text{"Not OK"} \quad \text{if } w_k > 0.2\mathrm{mm} \\ \text{"No cracks formed in SLS"} \quad \text{otherwise} \end{array}\right. = \text{"OK"}$$

Deflections

For < l/2: $$A_1 := \frac{l_1\cdot l^2}{48\cdot E_{cm}\cdot I_c}\cdot\left(3 - \frac{4l_1^{\,2}}{l^2}\right)$$

For > l/2: $$A_2 := \frac{l_3\cdot l^2}{48\cdot E_{cm}\cdot I_c}\cdot\left(3 - \frac{4l_3^{\,2}}{l^2}\right)$$

$$p_1 := P_k\cdot A_1 + P_k\cdot A_2 + \frac{5\cdot g_k\cdot l^4}{384\cdot E_{cm}\cdot I_c} = 11.128\cdot\mathrm{mm}$$

$$\left|\begin{array}{l} \text{"OK"} \quad \text{if } p_1 < \frac{1}{300} \\ \text{"Not OK"} \quad \text{otherwise} \end{array}\right. = \text{"OK"}$$

Shear design

Shear force carried by web

$P_d := \sigma_{p0.inf} \cdot A_p = 516.006 \cdot kN \qquad \alpha_p := \operatorname{atan}\left(\frac{e_f}{l_1}\right) = 3.776 \cdot deg$

$V_{ipd} := P_d \cdot \tan\left(\alpha_p\right) = 34.056 \cdot kN$

$V_{Ed.net} := V_{Ed} - V_{ipd} = 29.721 \cdot kN$

Uncracked in bending?

$l_s := 100mm$

$x_{crit} := \frac{l_s}{2} + \left(h - x_c\right) = 0.302\,m$

$M_1\left(x_{crit}\right) = 19.134 \cdot kN \cdot m$

Given

$\frac{e_{crit}}{x_{crit}} = \frac{e_f}{l_1}$

$e_{crit} := \operatorname{Find}\left(e_{crit}\right) \rightarrow 19.933913043478236 \cdot mm = 0.02\,m$

$P_{0.inf} := \sigma_{p0.inf} \cdot A_p = 5.16 \times 10^{5}\,N$

$\sigma_{ct} := \frac{-P_{0.inf}}{A_c} + \frac{-P_{0.inf} \cdot e_{crit} + M_1\left(x_{crit}\right)}{I_c} \cdot \left(h - x_c\right) = -3.669 \cdot MPa$

Compressed in lower edge, thereby uncracked in critical section.

Shear capacity of uncracked concrete

$S := b_w \cdot \frac{x_c^{\,2}}{2} + \left(b_{tf} - b_w\right) \cdot h_{tf} \cdot \left(x_c - \frac{h_{tf}}{2}\right) = 7.707 \times 10^{-3} \cdot m^3$

$f_{ctd} := \frac{f_{ctk0.05}}{1.5} = 2.088 \cdot MPa$

$\alpha_l := 1$

$\sigma_{cp} := \frac{P_i\left(x_{crit}\right)}{A_c} = 4.815 \cdot MPa$

$V_{Rd.cw} := \frac{I_c \cdot b_w}{S} \cdot \sqrt{f_{ctd}^{\,2} + \alpha_l \cdot \sigma_{cp} \cdot f_{ctd}} = 201.562 \cdot kN$

$$\left| \begin{array}{l} \text{"OK" if } V_{Ed.net} < V_{Rd.cw} \\ \text{"Shear cracks formed before ULS" otherwise} \end{array} \right. = \text{"OK"}$$

Shear capacity of cracked concrete without shear reinforcement

$C_{Rd.c} := \frac{0.18}{1.5} = 0.12$

$k := \min\left(1 + \sqrt{\frac{200mm}{d}}, 2.0\right) = 1.68$

$\rho_l := \min\left(0.02, \frac{A_{s1}}{b_w \cdot d}\right) = 0.012$

$k_1 := 0.15$

$$V_{Rd.c} := \max\left[\left(0.035\cdot k^{\frac{3}{2}}\cdot\sqrt{\frac{f_{ck}}{MPa}}Pa + k_1\cdot\sigma_{cp}\right)\cdot b_w\cdot d, \left[C_{Rd.c}\cdot k\cdot\left(100\cdot\rho_l\cdot\frac{f_{ck}}{MPa}\right)^{\frac{1}{3}} Pa + k_1\cdot\sigma_{cp}\right]\cdot b_w\cdot d\right]$$

$V_{Rd.c} = 46.915\cdot kN$ $\qquad$ $V_{Ed.net} = 29.721\cdot kN$

Web shear compression failure

$$\nu := 0.6\cdot\left(1 - \frac{\frac{f_{ck}}{MPa}}{250}\right) = 0.462$$

$$V_{Rd.max} := 0.5\cdot b_w\cdot d\cdot\nu\cdot f_{cd} = 863.75\cdot kN$$

$$Check := \begin{vmatrix} \text{"OK!"} & \text{if } V_{Rd.max} > R_A \\ \text{"Not OK!"} & \text{otherwise} \end{vmatrix} = \text{"OK!"}$$

Design of shear reinforcement

$$\rho_{w.min} := 0.08\cdot\frac{\sqrt{\frac{f_{ck}}{MPa}}}{\frac{f_{yk}}{}} = 1.214\times 10^{-3} \qquad A_{sw} := \frac{\phi_{stirrup}^{\;2}}{4}\cdot\pi = 50.265\cdot mm^2 \qquad \alpha := 90deg$$

Given

$$\rho_{w.min} = \frac{2\cdot A_{sw}}{s\cdot b_w\cdot\sin(\alpha)}$$

$$s := Find(s) \rightarrow \frac{0.00055192157032200574286\cdot m^2}{mm\cdot\sin(90.0\cdot deg)} = 0.552\,m$$

$$s_{l.max} := 0.75\cdot d\cdot(1 + \cot(\alpha)) = 0.325\,m$$

$$s := \min(s, s_{l.max}) = 0.325\,m$$

Detailing of anchorage region

$\gamma_p := 1.2$ unfavourable effects in anchorage zone.

$P := \gamma_p\cdot P_{i.1} = 673.2\cdot kN$

Vertical reinforcement:

$a := 100mm$ $\qquad$ $h = 0.475\,m$ $\qquad$ $b := \frac{h}{2} = 0.238\,m$

Tension tie: $\frac{1}{2}\cdot\frac{b-a}{b} = 28.947\cdot\%$

$T := \frac{1}{4}\cdot\frac{b-a}{b}\cdot P = 97.437\cdot kN$

Reinforcement amount: $A_v := \frac{T}{f_{yd}} = 194.874\cdot mm^2$

ϕ8: $n_v := 3$ 3 vertical stirrups a ϕ8 (middle stirrup placed 0.238m from edge and 21cm spacing

$$n_v\cdot 2\cdot\pi\cdot\left(\frac{\phi_{stirrup}}{2}\right)^2 = 301.593\cdot mm^2$$

Horizontal reinforcement (optional):

$a := 155\mathrm{mm}$ $b_{bf} = 0.28\,\mathrm{m}$ $b := \frac{b_{bf}}{2} = 0.14\,\mathrm{m}$

Tension tie: $\frac{1}{2}\cdot\frac{a-b}{b} = 5.357\cdot\%$

$T := \frac{1}{4}\cdot\frac{a-b}{b}\cdot P = 18.032\cdot\mathrm{kN}$

Reinforcement amount: $A_h := \frac{T}{f_{yd}} = 36.064\cdot\mathrm{mm}^2$

ϕ8: $n_h := 1$ 1 horizontal stirrups a ϕ8 (placed 0.14 m from edge)

$n_h\cdot 2\cdot\pi\cdot\left(\frac{\phi_{stirrup}}{2}\right)^2 = 100.531\cdot\mathrm{mm}^2$

B

Design of specimens

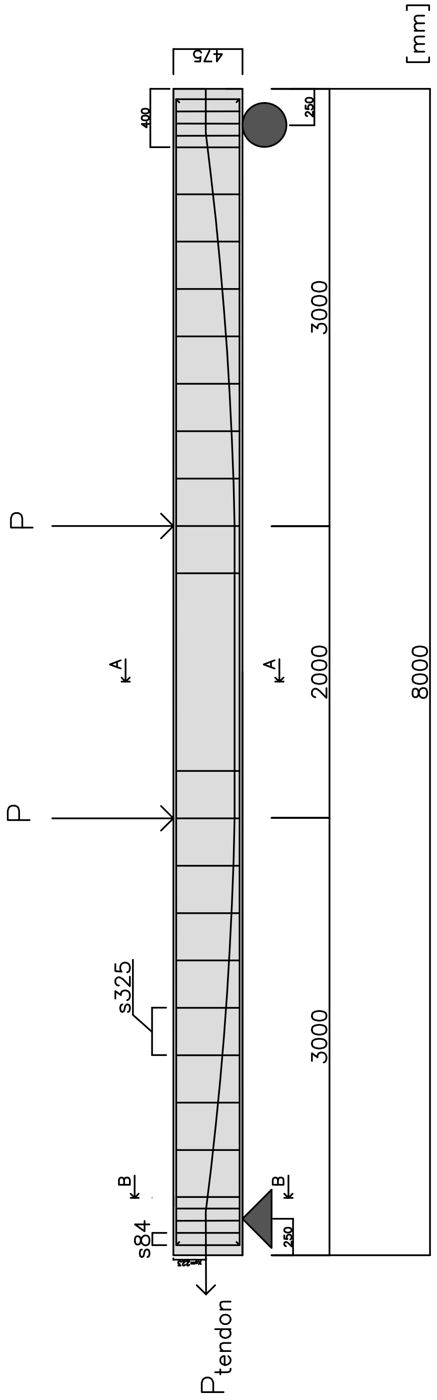
[mm]
475
400
250
3000
P
A
A
2000
8000
P
s325
3000
B
B
s84
250
P_{tendon}

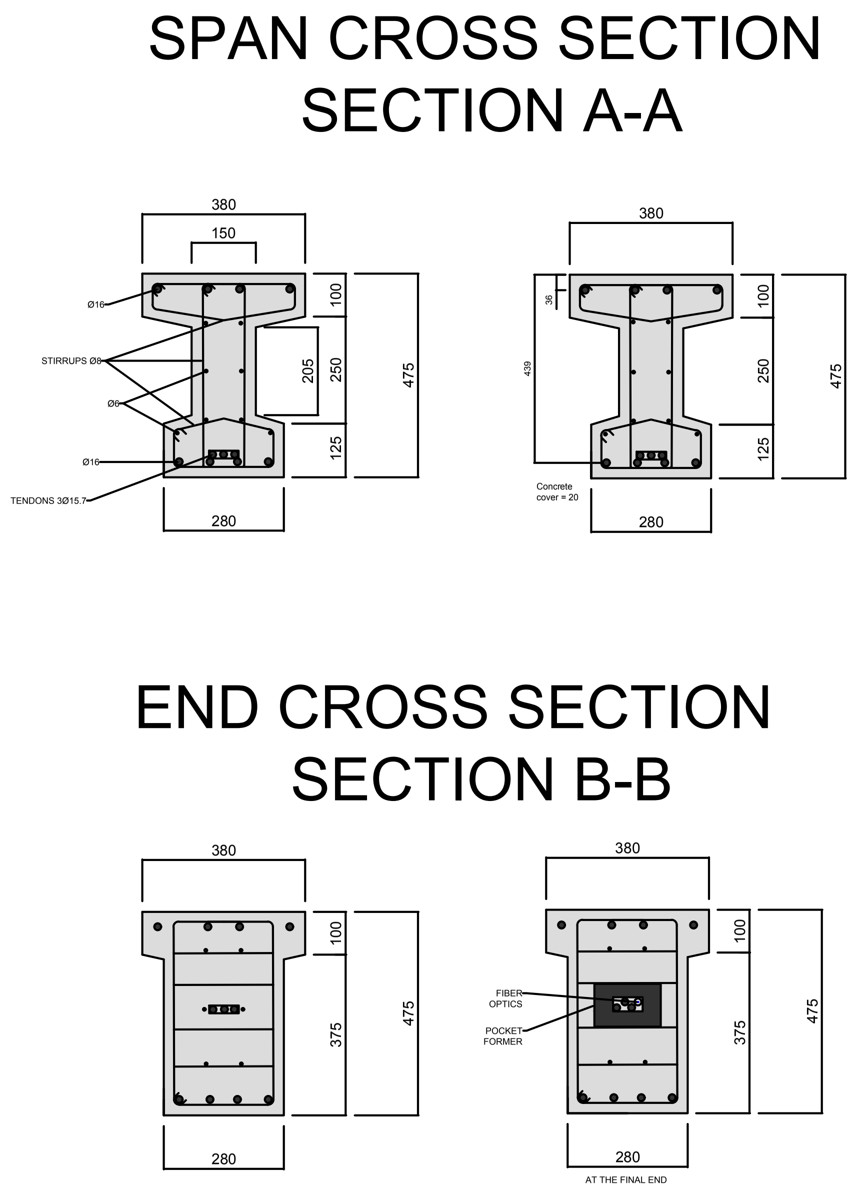
SPAN CROSS SECTION
SECTION A-A
380
150
Ø16
STIRRUPS Ø8
Ø6
Ø16
TENDONS 3Ø15.7
100
250
205
125
475
280
380
36
439
100
250
125
475
Concrete
cover = 20
280
END CROSS SECTION
SECTION B-B
380
100
375
475
280
380
FIBER
OPTICS
POCKET
FORMER
100
375
475
280
AT THE FINAL END

DEPARTMENT OF ARCHITECTURE AND CIVIL ENGINEERING
CHALMERS UNIVERSITY OF TECHNOLOGY
Gothenburg, Sweden
www.chalmers.se